International Telecommunication Union

ITU-R
Radiocommunication Sector of ITU

Model parameters for the physical-statistical wideband model in Recommendation ITU-R P.681

P Series

Radiowave propagation

International Telecommunication Union

Foreword

The role of the Radiocommunication Sector is to ensure the rational, equitable, efficient and economical use of the radio-frequency spectrum by all radiocommunication services, including satellite services, and carry out studies without limit of frequency range on the basis of which Recommendations are adopted.

The regulatory and policy functions of the Radiocommunication Sector are performed by World and Regional Radiocommunication Conferences and Radiocommunication Assemblies supported by Study Groups.

Policy on Intellectual Property Right (IPR)

ITU-R policy on IPR is described in the Common Patent Policy for ITU-T/ITU-R/ISO/IEC referenced in Annex 1 of Resolution ITU-R 1. Forms to be used for the submission of patent statements and licensing declarations by patent holders are available from http://www.itu.int/ITU-R/go/patents/en where the Guidelines for Implementation of the Common Patent Policy for ITU-T/ITU-R/ISO/IEC and the ITU-R patent information database can also be found.

Series of ITU-R Reports

(Also available online at http://www.itu.int/publ/R-REP/en)

Series	Title
BO	Satellite delivery
BR	Recording for production, archival and play-out; film for television
BS	Broadcasting service (sound)
BT	Broadcasting service (television)
F	Fixed service
M	Mobile, radiodetermination, amateur and related satellite services
P	**Radiowave propagation**
RA	Radio astronomy
RS	Remote sensing systems
S	Fixed-satellite service
SA	Space applications and meteorology
SF	Frequency sharing and coordination between fixed-satellite and fixed service systems
SM	Spectrum management

Note: This ITU-R Report was approved in English by the Study Group under the procedure detailed in Resolution ITU-R 1.

Electronic Publication
Geneva, 2017

© ITU 2017

REPORT ITU-R P.2145-2

Model parameters for the physical-statistical wideband models in Recommendation ITU-R P.681

(2009-2013-2017)

Summary

This Report describes the physical-statistical wideband LMSS channel model in Recommendation ITU-R P.681 § 7, providing all background and relevant information.

TABLE OF CONTENTS

Part A: Model parameters for an urban environment for the physical-statistical wideband land mobile satellite services channel model in Recommendation ITU-R P.681

1   Wideband LMSS channel model

The statistical data provided with the physical-statistical wideband land mobile satellite services (LMSS) channel model also named in this Report as the land mobile satellite channel model (LMSCM), was derived from measurement data recorded in a comprehensive high resolution channel sounding campaign in and around Munich in 2002. In this campaign different urban, suburban and rural environments were measured for car and pedestrian applications.

In these measurements the satellite of a potential navigation system was simulated by a Zeppelin NT. The Zeppelin transmitted the measurement signal between 1 460 and 1 560 MHz towards the ground using a hemispherical, circular polarized, antenna with 10W e.i.r.p. The receiver was mounted in the measurement vehicle, which was driven through the measurement area. In the case of the pedestrian measurement the antenna was carried by the walking user followed by the measurement vehicle.

Based on this measurement data the LMSCM was developed. This model is a realistic high resolution deterministic-statistical model.

A receiver can be moved through a synthetic environment with houses, trees and lamp posts. These obstacles influence the LoS path. In addition reflectors are produced causing echo signals.

The statistical part of the model comprises:
–   the house front, tree and lamp post generation in the synthetic environment;
–   the position dependent LoS signal power variations in the shadow of tree tops;
–   the position of reflectors dependent on the satellites azimuth and elevation;
–   the mean power of echoes depending on their distance to the receiver and on the;
–   satellite elevation;
–   Rice factor and bandwidth of echo signals depending on the satellite elevation;
–   the life span of echoes depending on the satellite elevation;
–   the number of coexisting echoes in the channel depending on the satellite elevation;
–   and the movement of reflection points, also depending on the satellite elevation.

Deterministically modelled are:
–   the diffraction of the LoS signal on houses, tree trunks and lamp posts;
–   the delay of diffracted signals received in the shadow of houses;
–   the mean attenuation through tree tops;
–   and the delay and Doppler shift trends of echo signals due to the receiver and reflector movement.

An important model feature is the high level of detail. Realistic correlation between echo signals is achieved due to the used reflector position statistics combined with the deterministically calculated delay and Doppler trends. Full satellite azimuth and elevation dependency is given for both LoS and the echo signals. As general model parameters the snapshot rate, the frequency band, the user type and the environment can be chosen.

Parameters for the distribution of e.g. house heights and widths, for tree and lamp post size and positions, but also for the street width and e.g. the receiver antenna height allow to model specific scenarios and to investigate their impact. High flexibility is also given by the way oriented

deterministic and stochastic model approach. Receiver speed and heading input allows to simulate different movement situations, e.g. turns, a traffic jam, stop and go, or the relatively long stops at traffic lights. Also speeds which are even higher than during the measurement can be applied.

For a complete description of the measurement, the data analysis and the modelling of the satellite to earth multipath channel see also [1].

The structure of this Part A is the following: section 1 gives an introduction to the model; section 2 describes in detail the characteristics of the channel model and implementation features; section 3 provide all features of the model which are dependent on the urban scenario where measurements were originally taken for the development of the model; section 4 includes an Interface Control Document for users interested on understanding the software implementation or re-implement the model. Acronyms are found in § 6. Section 8 provides information on intellectual property rights associated to the models and References.

2   Software model download

The MATLAB implementation of the model needs only 140 KB disk space including the statistical data for the urban city centre environment for car applications. It is a stand-alone model generating its own scenery. The execution speed is reasonably fast with 250 complex channel impulse responses per second on a 1.5 GHz CPU. The model output is a complex time-variant channel impulse response with up to 80 discrete rays. Due to this time variant tapped delay line structure it can be easily incorporated in any simulator.

The complete model implemented in MATLAB can be downloaded from: http://www.kn-s.dlr.de/satnav/.

3   Physical-statistical wideband model for mixed propagation conditions

For broadband LMSS with a multipath propagation channel where different frequencies within the signal bandwidth are affected differently by the channel (frequency-selective channels), a model that implements a linear transversal filter whose output is a sum of delayed, attenuated and Doppler shifted versions of the input signal (wideband model) is more suitable. Definitions on multipath propagation are found in Recommendation ITU-R P.1407-2.

The model is given for a situation where a satellite is transmitting from a known position to a receiver on ground, where an elevation ε and an azimuth φ can be computed relative to the receiver heading and position. The model can be applied for frequencies between 1 and 2 GHz. It is suitable to serve the requirements of wideband transmission systems with a bandwidth up to 100 MHz. The model is based on deterministic and stochastic parameters and it is able to generate vectors that include complex envelope time-series of direct signal and reflections, with corresponding path delay vectors. The parameters determining the stochastic behaviour of the model are derived from measurements obtained on a given scenario.

The geometry of the model is based on a synthetic environment representation. In the scenery there is a local Cartesian coordinate system. To keep the model simple, the receiver is moving in the x-direction only. Turns (changes of the receiver heading) are modelled by changing the satellite azimuth. Therefore, the model azimuth is calculated by:

$$\varphi = \varphi_{Rx} - \varphi_{sat} \tag{1}$$

where:

φ_{Rx} : absolute heading of the receiver

φ_{sat} : absolute satellite azimuth.

For the movement model, in the local coordinate system the receiver position is calculated by:

$$x(t) = \int_0^t v_{Rx}(t)\, dt \qquad (2)$$

where $v_{Rx}(t)$ is the velocity of the receiver. The y and z coordinates stay constant during the simulation run.

The channel model is realized in a modular way consisting of a combination of the following parts:

–   Shadowing of the direct signal:
    –   house front module;
    –   tree module;
    –   light pole module;
–   Reflections module.

The structure of the model is illustrated in Fig. 1 including the following input, intermediate and output time-variant signals:

   $v_u(t)$: user speed

   $hd_u(t)$: user heading

   $el_s(t)$: satellite elevation

   $az_s(t)$: satellite azimuth

   $x_u(t)$: user position in x-axis (y and z axis are considered constant)

   $az_u(t)$: user azimuth

   $y_u(t)$: output signals, where each *i* is related to direct signal and reflectors.

FIGURE 1

Structure of the model

Report P. 2145-01
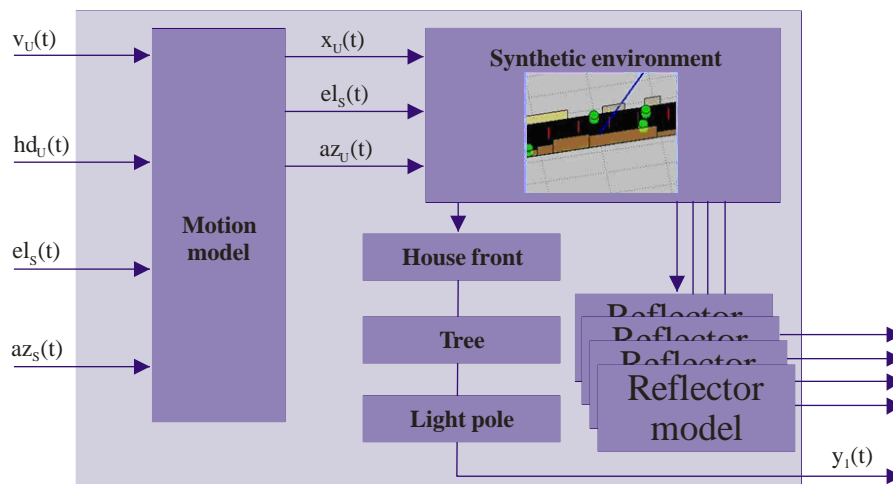
3.1 Shadowing of the direct signal

The shadowing and diffraction of the direct signal path at house fronts, trees and light poles within the scenery is calculated from a single knife-edge model (see Recommendation ITU-R P.526). A sketch of the general geometry is given in Fig. 2.

FIGURE 2

Communicating antennas over an obstacle
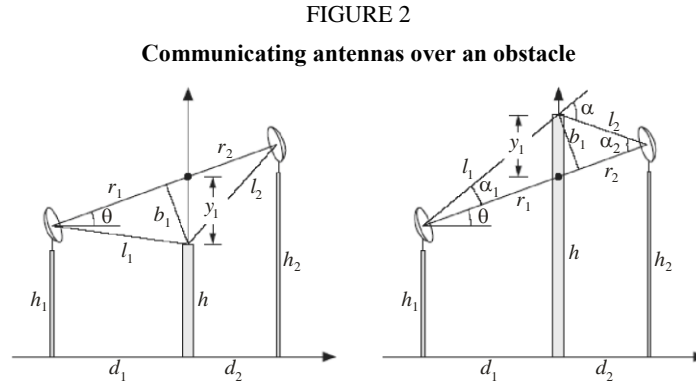
Report P. 2145-02

With the normalized Fresnel variable:

$$\nu = b_1 \sqrt{\frac{2}{\lambda} \frac{d_1 + d_2}{d_1 d_2}} = y_1 \cos(\theta) \sqrt{\frac{2}{\lambda} \frac{d_1 + d_2}{d_1 d_2}} \tag{3}$$

the diffraction coefficient $D(\nu)$ can be computed from the Fresnel integral $F(\nu)$ by:

$$D(\nu) = \frac{1}{1-j}\left(F(\nu) + \frac{1-j}{2}\right) = \frac{1}{1-j}\left(\int_0^\nu e^{-j\frac{\pi}{2}u^2}\,du + \frac{1-j}{2}\right) \tag{4}$$

The distance y_1 is defined positive if there is a direct sight between the antennas, whereas it is negative if the considered obstacle is shadowing the signal, i.e. $y_1 = \begin{cases} -|y_1| & \text{if LoS shadowed} \\ |y_1| & \text{otherwise} \end{cases}$

3.1.1 House-front module

Let P denote the point where the direct signal between satellite and receiver intersects with the considered house front. Then diffraction occurs at the roof of the house above or below that point, and at the closest walls to the left and to the right of it (see Fig. 3):

–   If the intersection point P falls inside a house (the direct ray is shadowed), the LoS signal is shadowed. In this case the model returns three paths, with relative delays, $\Delta\tau_{roof}$, $\Delta\tau_{wall,left}$, $\Delta\tau_{wall,right}$ and complex amplitude factor . $D(\nu_{roof})$, $D(\nu_{wall,left})$, $D(\nu_{wall,right})$ respectively corresponding to the roof, the left wall and the right wall around P.

–   If the intersection point P does not fall inside a house (the direct ray is not shadowed), the model returns a single path with amplitude factor $D(\nu)$ corresponding to the smallest y_1 and with $\Delta\tau$ equal to zero.

FIGURE 3

Diffraction at roofs and walls of house front
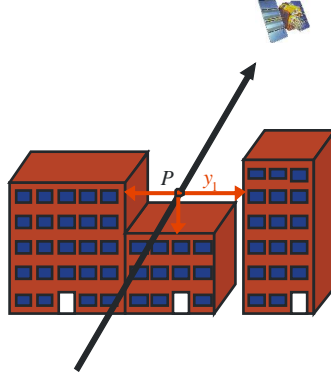
Report P. 2145-03

The diffraction coefficients can be computed from the following variables:

Diffraction at house roof

The diffraction coefficient and relative delay due to diffraction at house roof are computed by the model according to the following steps:

Step 1: The distance between the intersection point P and the receiver on ground plane is calculated as follows:

$$d_1 = \sqrt{(x_P - x_{Rx})^2 + (y_P - y_{Rx})^2} \tag{5}$$

Step 2: The distance between P and the satellite is calculated as follows:

$$d_2 = \sqrt{(x_{Sat} - x_P)^2 + (y_{Sat} - y_P)^2} \tag{6}$$

Step 3: The distance between the vertical distance between P and house roof is calculated as follows:

$$\left|y_{1,roof}\right| = \left|X_P - X_{roof}\right| \tag{7}$$

Step 4: Calculate the normalized Fresnel variable v_{roof} according to equation (3), θ being the elevation angle of the satellite from the receiver.

Step 5: The diffraction coefficient due to diffraction at house roof $D(v_{roof})$ is calculated according to equation (4).

Step 6: The path delay $\Delta\tau_{roof}$ is calculated as follows:

$$\Delta\tau_{roof} = \left(\sqrt{(z_{roof} - z_{Rx})^2 + d_1^2} - \frac{d_1}{\cos(\theta)} + y_1\sin(\theta)\right) \cdot c_0 \tag{8}$$

Diffraction at house walls

The diffraction coefficients and relative delays due to diffraction at house walls are computed by the model according to the following steps:

Step 1: The distance between the intersection point P and the receiver on ground plane is calculated as follows:

$$d_1 = \sqrt{(x_P - x_{Rx})^2 + (y_P - y_{Rx})^2}$$ (9)

Step 2: The distance between P and the satellite is calculated as follows:

$$d_2 = \sqrt{(x_{Sat} - x_P)^2 + (y_{Sat} - y_P)^2}$$ (10)

Step 3: The vertical distances between P and the left and right house walls are calculated as follows:

$$\left| y_{1,left} \right| = \left| X_P - X_{wall,left} \right|$$ (11)

$$\left| y_{1,right} \right| = \left| X_P - X_{wall,right} \right|$$ (12)

Step 4: The angle θ is calculated as follows:

$$\arctan\left(\frac{\left| x_P - x_{Rx} \right|}{d_1} \right)$$ (13)

Step 5: The normalized Fresnel variables $v_{wall,left}$ and $v_{wall,right}$ are calculated according to equation (3), θ being the angle calculated at Step 4.

Step 6: The diffraction coefficients due to diffraction at house roof $D(v_{wall,left})$ and $D(v_{wall,right})$ are calculated according to equation (4).

Step 7: The path delays $\Delta\tau_{wall,left}$ and $\Delta\tau_{wall,right}$ are calculated as follows:

$$\Delta\tau_{wall,left} = \left(\sqrt{(z_{roof} - z_{Rx})^2 + d_1^2} - \frac{d_1}{\cos(\theta)} + y_{1,left}\sin(\theta) \right)$$ (14)

$$\Delta\tau_{wall,right} = \left(\sqrt{(z_{roof} - z_{Rx})^2 + d_1^2} - \frac{d_1}{\cos(\theta)} + y_{1,right}\sin(\theta) \right)$$ (15)

As mentioned in the introduction, if the intersection point P does not fall inside a house, the model returns a single path with amplitude factor $D(v)$ corresponding to min $(y_{1,roof}, y_{1,left}, y_{1,right})$ and with $\Delta\tau$ equal to zero.

3.1.2 Light pole module

Let P denote the point on the direct ray being closest to the axis of the light pole, and d be this closest distance (see Fig. 4). Consider the line through P that is orthogonal to the tree axis and to the direct ray. Diffraction occurs at the two points where this line intersects with the surface of the pole. The effect of these two sides of the pole is coherently added according to a double knife-edge diffraction model (see Recommendation ITU-R P.526):

$$D\big(v_{left}, v_{right}\big) = \frac{1}{1-j}\left(F(v_{left}) + \frac{1-j}{2}\right) + \frac{1}{1-j}\left(F\big(-v_{right}\big) + \frac{1-j}{2}\right) \tag{16}$$

Step 1: The distance from the point P to the pole axis is calculated as follows:

$$d = \sqrt{(x_{pole} - x_{Rx})^2 + (y_{pole} - y_{Rx})^2}\,\sin(\varphi_{sat} - \varphi_{pole}) \tag{17}$$

Step 2: The distance from the receiver to the point P is calculated as follows:

$$d_2 = \sqrt{(x_{Sat}^2 - x_P^2) + (y_{Sat}^2 - y_P^2) + (z_{Sat}^2 - z_P^2)} \tag{18}$$

Step 3: The distance from the point P to the satellite is calculated as follows:

$$d_1 = \sqrt{(x_{pole} - x_{Rx})^2 + (y_{pole} - y_{Rx})^2}\,\frac{\cos(\varphi_{sat} - \varphi_{pole})}{\cos(\varepsilon_{sat})} \tag{19}$$

Step 4: The distance from the point P to the left and right intersection points with the surface of the pole are respectively calculated as follows:
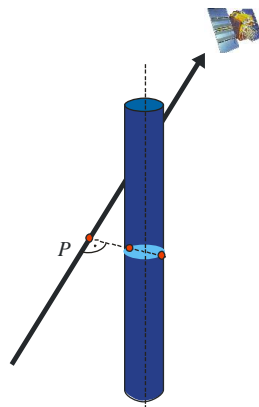
$$b_{1,left} = y_{1,left} = d - R_{pole} \tag{20}$$

$$b_{1,right} = y_{1,right} = d + R_{pole} \tag{21}$$

Step 5: The normalized Fresnel variables v_{left} and v_{right} are calculated according to equation (3).

Step 6: The diffraction coefficient due to diffraction at light pole $D(v_{left}, v_{right})$ is calculated according to equation (4).

FIGURE 4

Diffraction at a light pole

Report P. 2145-04

3.1.3 Tree module

Diffraction at the tree trunk

For the trunk of a tree the same double knife-edge model as for the light poles is considered in § 3.1.2.

Attenuation at the tree top

The attenuation factor caused by the top of a tree:

$$A_{tree}(x) = A_{cyl}(x) \cdot A_{stoch}(x) \tag{22}$$

is divided into a deterministic and a stochastic part (see Fig. 5). The deterministic term A_{cyl} is proportional to the length of the part of the direct ray that intersects with the cylinder of the tree model. It depends on the tree geometry and the specific attenuation γ_{tree} (see § 3.3).

The stochastic part is modelled by a Ricean fading process with the Gaussian way-power spectrum:

$$A_{stoch}(x) = \frac{1}{\sqrt{K_{tr}+1}} \left(\sqrt{K_{tr}} e^{j\varphi_c} + F^{-1}\left\{ \sqrt{S_{tr}(X)} \right\} \right) \tag{23}$$

with

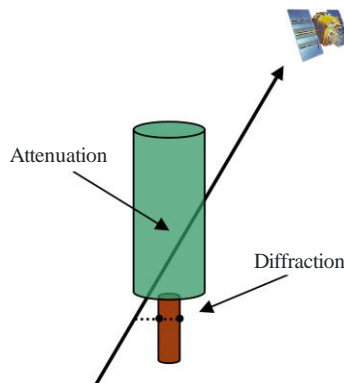$$S_{tr}(X) = \frac{1}{\sqrt{2\pi\sigma^2}} e^{-\frac{X^2}{2\sigma^2}} \tag{24}$$

and

$$\sigma = \frac{B_{tr}}{2\sqrt{2\ln(2)}}$$

where:

K_{tr} and B_{tr}: respectively denote the Rice factor and the 3-dB bandwidth of the spectrum (see § 3.3)

φ_c: phase which is chosen randomly between 0 and 2π for each tree according to a uniform distribution.

FIGURE 5

Diffraction and attenuation by a tree

Report P. 2145-05

3.2 Reflections

The model uses reflectors that are realized as infinitively small spheres with a given attenuation to the direct path radiating equally in any direction. Based on these reflectors, a set of echoes is generated from a geometric position in the synthetic environment. The following sections deal with the generation of the echoes in terms of:

– position;

– lifespan;

– mean power (average and variation);

– fading (process, bandwidth, rice factor);

– reflector movement;

– number of echoes generation.

3.2.1 Synthesis of a single reflection

The likelihood of receiving an echo from a given reflector position is strongly dependent of the position of the reflector relative to the receiver and the satellite.

Horizontal position

The likelihood density distribution $P_{r,\psi}(\varepsilon, \varphi)$ for the existence of a reflector being present at a given position (polar coordinates r, ψ) is calculated as:

$$p_{r,\psi}(\varepsilon,\varphi) = \frac{p_{r,\psi}(\varepsilon) \cdot p_{\alpha-\varphi}(\varepsilon)}{\iint p_{r,\psi}(\varepsilon) \cdot p_{\alpha-\varphi}(\varepsilon)\mathrm{d}r\mathrm{d}\psi} \tag{25}$$

where ε is the satellite elevation; φ is the satellite azimuth; α is the right-hand oriented angle between the reflector and satellite seen from the receiver (see Fig. 6); $p_{r,\psi}(\varepsilon)$ is the probability density of a reflector being present at the horizontal position r, ψ, assuming an equal distribution of φ; and $p_{\alpha-\varphi}(\varepsilon)$ is the probability density of a reflector being present at the relative direction between φ and α (see § 3.3).

FIGURE 6

Relative angle, α
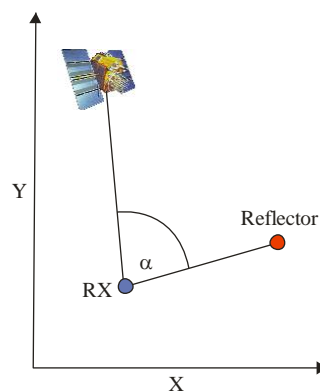
Report P. 2145-06

Z-Position

To determine the Z-position of the reflector, assume that the elevation of the reflection ray does not change, since most of the reflecting walls are vertical.

Therefore, the reflector z coordinate is given by:

$$z = \min\left(\frac{r}{\cos(\varepsilon)}, h_b - h_{RX}\right)$$ (26)

where r is the distance between receiver and reflector, h_b is the height of a randomly-chosen building according to the building height distribution in the modelled environment, and h_{RX} is the antenna height above ground.

Echo power

The power radiated from a reflector is modelled by a Gaussian distribution:

$$p_e(P) = \frac{1}{\sqrt{2\pi}\sigma(r,\psi,\varepsilon)} \exp\left(-\frac{(P-\mu(r,\psi,\varepsilon))^2}{2\sigma(r,\psi,\varepsilon)^2}\right)$$ (27)

where $\sigma(r, \psi, \varepsilon)$ and $\mu(r, \psi, \varepsilon)$ are, respectively, the power variance and the power mean at the relative position (r, ψ) for the satellite elevation, ε (see § 3.3).

Echo fading

The isolated echo signal is modelled as a Rican fading process. This process is modelled by:

$$s_{stoch}(t) = \sqrt{P_e}\frac{1}{\sqrt{K}+1}\left(\sqrt{K}\exp(j\varphi_C) + F^{-1}\left\{\sqrt{S(f)}\right\}\right)$$ (28)

where:

p_e : selected echo power as in equation (27)

K : Rice factor (see § 3.3)

φ_C : randomly-chosen (uniformly distributed between 0 and 2π) initial phase of the constant part

$F^{-1}\{S(f)\}$: statistical process that in average fits to the spectrum $S(f)$, assumed to be Gaussian distributed:

$$S(f) = \frac{1}{\sqrt{2\pi}\sigma}\exp\left(-\frac{f^2}{2\sigma^2}\right)$$ (29)

where σ is given by:

$$\sigma = \frac{B_e}{2\sqrt{2\ln(2)}}$$ (30)

with B_e being the 3-dB bandwidth of the echo selected from the Gaussian probability density function $p_{be}(\varepsilon)$ (see § 3.3). The mean and variance of this bandwidth are derived from measurements for a given scenario.

The echo fading process is highly correlated with the movement of the receiver. Therefore, the complex value of the echo is modelled by:

$$s(x,t) = s_{stoch}(t) \cdot \exp\left(-j(\varphi_D(x) + \varphi_{i,R})\right)$$ (31)

where x is the x-position of the receiver, $\varphi_{i,R}$ is the randomly-chosen (uniformly distributed between 0 and 2π) initial phase of the echo, and φ_D is the deterministic Doppler phase shift due to the receiver movement given by:

$$\varphi_D(x) = \frac{\left|\overline{r}_r(x)\right|}{2\pi\lambda} \tag{32}$$

with $\overline{r}_r(x)$ the vector from the receiver to the reflection point, and λ, the wavelength.

The relative delay (with respect to the direct signal) of the echo can be calculated by:

$$\Delta\tau(x) = \frac{\left|\overline{r}_r(x)\right| - \overline{r}_r(x) \cdot \overline{r}_s(x)}{c_0} \tag{33}$$

where $\overline{r}_s(x)$ is the normalized vector from the receiver to the satellite.

Reflector life span

The echoes appear and disappear rapidly and often, their lifetime is highly dependent on the receiver speed. The lifespan is modelled as a function dependent on the travelled direction.

The actual life span is selected from a given cumulative distribution function, $P_{ls}(\varepsilon)$, derived from measurements for a given scenario (see § 3.3).

Reflector movement

Some reflection points tend to move parallel to the receiver movement; the rest of the points are assumed to be static. The probability of a reflector moving depends on the satellite elevation. This probability $\Pr\left(\text{mov}_{refl} \xleftrightarrow[\text{parallel}]{} \text{mov}_{Rx}/\varepsilon\right)$ is derived from measurements for a given scenario (see § 3.3).

3.2.2 Number of coexisting reflections

The number of coexisting echoes is modelled as a combination of a synthetically-generated wideband and narrow-band process, overlaid by a constant:

$$N(x,\varepsilon) = N_n(x,\varepsilon) + N_w(x,\varepsilon) + \overline{N}(\varepsilon) \tag{34}$$

where:

$N_n(x,\varepsilon)$: narrow-band process (with a Gaussian distributed amplitude)

$N_w(x,\varepsilon)$: wide band process (also with a Gaussian distributed amplitude)

$\overline{N}(\varepsilon)$: constant describing the average number of echoes.

The power spectral density of the process $PSD\{N(x,\varepsilon)\}$, and the mean value $\overline{N}(\varepsilon)$, are derived from measurements for a given scenario (see § 3.3).

3.3 Model parameters for an urban environment

Table 1 summarizes the inputs to the different elements of the model that are scenario-dependent and derived from data. For the use of the model as a whole, synthetic scenery needs to be generated with given characteristics for the size and distribution of trees, light poles and buildings in the scenery. In § 4 the parameters for the generation of this scenery for the measured case in Munich are included.

TABLE 1

Scenario-dependant parameters and functions extracted from data files

Parameter	Description
γ_{tree}	Specific attenuation (dB/m) for the deterministic part of tree attenuation A_{cyl}
K_{tr}	Rice factor tree attenuation Ricean fading process A_{stoch}
B_{tr}	3-dB bandwidth of tree attenuation Ricean fading process A_{stoch}
$p_{r,\psi}(\varepsilon)$	Probability density of a reflector being present at the horizontal position, r, ψ, assuming an equal distribution of the satellite azimuth φ
$p_{\alpha-\varphi}(\varepsilon)$	Probability density of a reflector being present at the relative direction between the azimuth φ and the angle α between reflector and satellite seen from the receiver
$\mu(r, \psi, \varepsilon)$	Power mean at the relative position (r, ψ) observed in the measurement for the satellite elevation ε
$\sigma(r, \psi, \varepsilon)$	Power variance at the relative position (r, ψ) observed in the measurement for the satellite elevation ε
B_e	3-dB bandwidth of the echo selected from the Gaussian probability density function $p_{be}(\varepsilon)$ with mean and variance depending on elevation ε
K	Rice factor of the echo fading Ricean process
$P_{ls}(\varepsilon)$	Cumulative distribution function of the life span of a reflector as a function of elevation ε
$Pr\left(\text{mov}_{refl} \underset{\text{parallel}}{\longleftrightarrow} \text{mov}_{Rx}/\varepsilon\right)$	Probability that a reflector moves parallel to the receiver, depending on elevation ε
$\overline{N}(\varepsilon)$	Constant describing the average number of echoes as a function of elevation ε
$PSD\{N(x,\varepsilon)\}$	Power spectral density of the process (narrow-band plus wideband) describing the number of echoes as a function of elevation ε

3.4 Model input

For every input sample some values must be given for the model input:

– satellite elevation
– satellite azimuth
– user speed
– user heading.

Please note that the user speed is limited by the sampling frequency:

$$v < \frac{c_0 \cdot f_{samp}}{f_c \cdot 2} \tag{35}$$

where f_{samp} is the sampling frequency, f_c is the carrier frequency and c_0 is the speed of light. It is recommended to use some over-sampling factor.

3.5 Model output

The model outputs a vector of N path delays τ_i and N complex values $A_i(t)$ for every time instance. The equivalent baseband channel impulse response is given by:

$$h(t,\tau) = \sum_{i=1}^{N} A_i(t) \cdot \delta(\tau - \tau_i(t)) \tag{36}$$

where t and τ indicate time and delay axes respectively. Please note that the path delays $\tau_i(t)$ are time-variant and they can reach arbitrary values.

The following Figures give an example of the model output. For these Figures the user speed was set to $v(t) = (\sin(t+t_0)+1) \cdot v_{max}$. In Fig. 7 the red dashed line shows the maximum possible Doppler frequency according to the current user speed and the carrier frequency. The other coloured lines show the Doppler frequency of the echoes – their width is proportional to the actual power. At instances $t = 4,7$ s the car came to a full stop which reduces the Doppler to a minimum driven by the time driven fading process.

Figure 8 shows the Delay variation of the reflections. Due to the given life span, the life time of the reflections is dependent of speed. In regions where the receiver speed is high the echo life time is short but in regions with low user speeds the echoes can live for a long time.
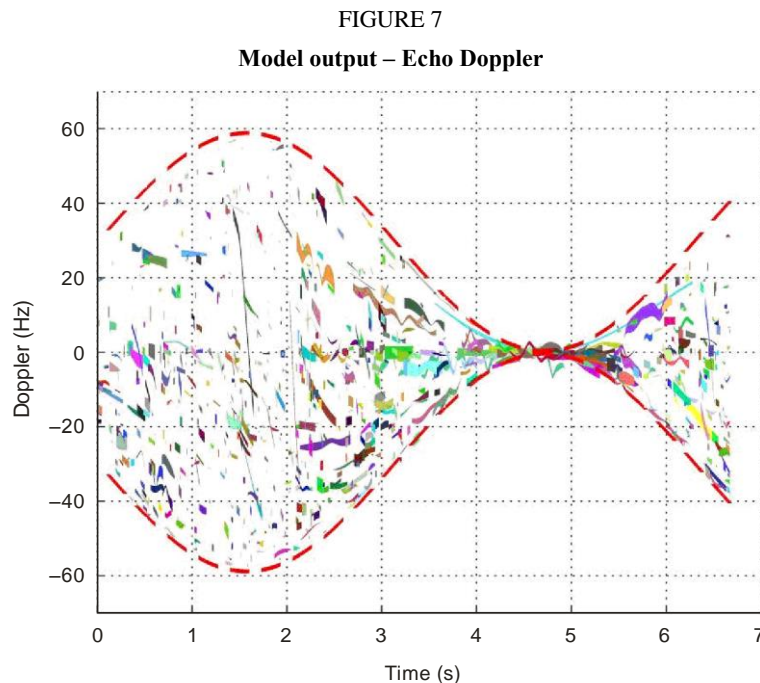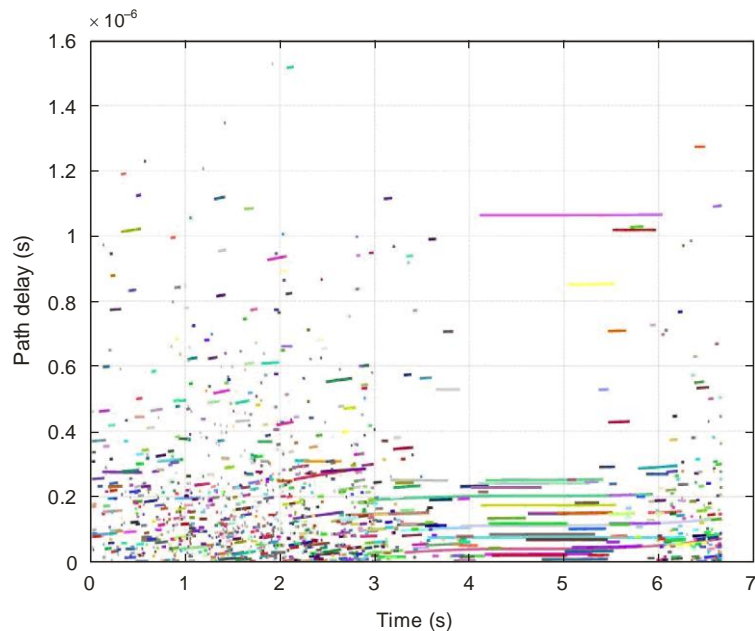
FIGURE 7

Model output – Echo Doppler

Report P. 2145-07

FIGURE 8

Model output – Echo delay

3.6 Model output usage

Let $s(t)$ be the transmitted equivalent baseband signal, then the received signal $r(t)$ can be calculated in the usual way, by the convolution of the transmitted signal with the channel impulse response as:

$$r(t) = s(t) * h(t, \tau) \tag{37}$$

The channel impulse responses as model output are updated at a rate given by f_{samp}.

The delay axis τ of the output is continuous, thus, in order to implement the channel impulse response into a FIR filter a discretization of the delay axis is required. This is done by interpolation as explained in § 3.7.

3.7 User Implementation Features: interpolation of series of time-continuous discrete impulses to FIR filter coefficients

The time-continuous CIR time series provided by channel models have to be converted to the discrete-time sampling grid to be applicable in simulation software. Several options for this interpolation process are possible.

Two different types of interpolation methods are lined out within this Report. The first procedure is the standard time domain low-pass interpolation method using a $\sin(x)/x$ formulation. It is shown that the usage of this method results in a fluctuating and unsatisfying phase response in the case of time-continuous echoes as inputs.

The introduced frequency domain method demonstrates far better results from a phase response point of view.

To clarify the process, examples with three Dirac impulses (which could represent a CIR) are calculated in the next sections.

To provide a sanity check of the described procedure, in § 3.7.1 first assumes that the given echo impulses sit directly on sampling instants. Secondly, § 3.7.2 describes the time domain low-pass interpolation and § 3.7.3 introduces the frequency domain method.

All these sections carry out the example calculation with a sampling frequency of $f_{smpl}=25$ MHz whereas § 3.7.4 gives a comparison of the interpolation methods' properties for the same example but at sampling frequency of 100 MHz.

3.7.1 Low-pass interpolation of sampling points matching Dirac input impulses

For the following example calculation, a sampling frequency of $f_{smpl}=25$ MHz is assumed. Three Dirac-like impulses are given which lay exactly on sampling instants:

$$T_n(0)=0\text{s}$$

$$T_n(1)=0.12\times10^{-6}\text{s} \tag{38}$$

$$T_n(2)=0.36\times10^{-6}\text{s}$$

and they possess the following complex weights:

$$A_n(0)=1$$

$$A_n(1)=0.87\cdot e^{j\left(\frac{1}{4}\pi\right)} \tag{39}$$

$$A_n(2)=0.24\cdot e^{j(-0.37\cdot\pi)}$$

The complete input signal can be written as:

$$x(t)=\sum_{k=0}^{m}A_n(k)\cdot\delta(t-T_n(k)) \tag{40}$$

Here, the considered time duration shall span from $t=0$ s until $t=0.44\times10^{-7}$ s. Figure 9 shows a plot of $x(t)$'s magnitude.

$x(t)$ can now be interpolated at the sampling points:

$$t_n=n\cdot\frac{1}{f_{smpl}}, \quad n=0,1,...,11 \tag{41}$$

using the low-pass interpolation formula [Kammeyer and Kroschel, 2002]:

$$h(t_n)=\sum_{k=0}^{m}A_n(k)\cdot si[\omega_{max}(t-T_n(k))] \tag{42}$$

where:

$$si(x) = \frac{\sin(x)}{x} \qquad (43)$$

and

$$\omega_{max} = 2\pi \frac{f_{smpl}}{2} \qquad (44)$$

The magnitude plot of the resulting 12 interpolated points can be seen as red crosses in Fig. 10. The continuous lines show the values of the single si-function for every Dirac impulse. The black line shows the resulting sum of the three functions.

The two subsequent sections examine the case when the Dirac impulses occur on time instants which do not match sampling points.

FIGURE 9

**Example signal with three complex Dirac impulses at time instants that match sampling points.
Magnitude plot**
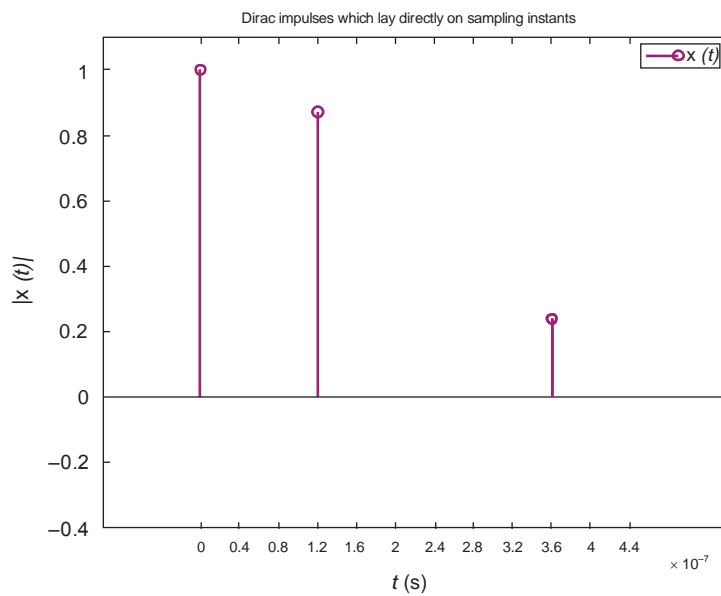
Report P. 2145-09

FIGURE 10

**Interpolated with three complex Dirac impulses at time instants that match sampling points.
Magnitude plot**
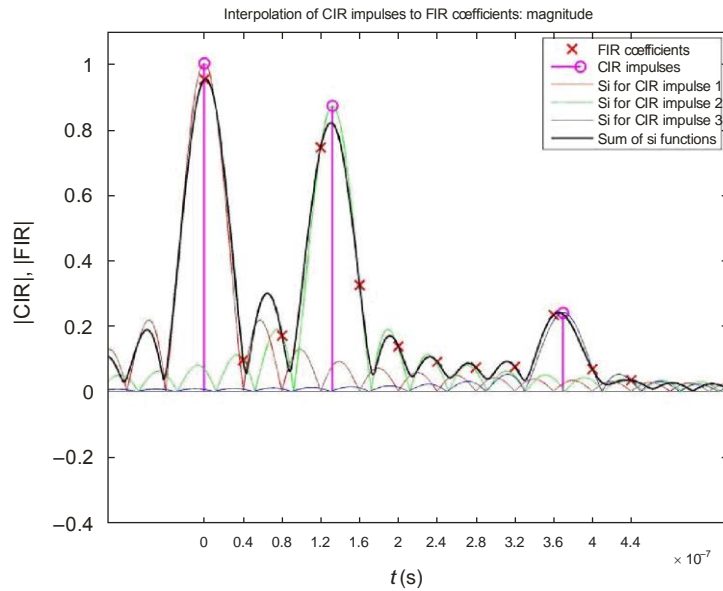
Report P. 2145-10

FIGURE 11

**Interpolated $x(t)$ with three complex Dirac impulses at time instants that match sampling points.
Phase plot**
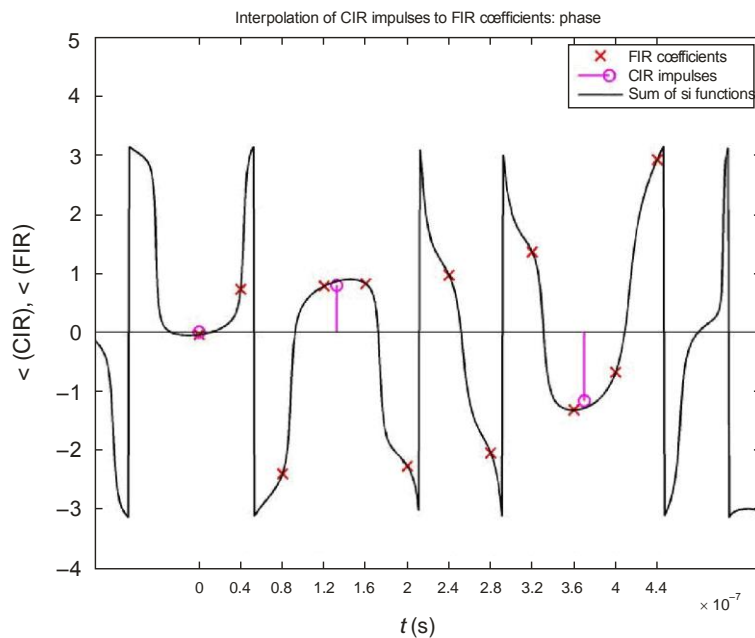
Report P. 2145-11

3.7.2 Low-pass interpolation of time-continuous Dirac input impulses

The same complex weights as given in equation (39) are used again, but compared to the times in equation (38) the last two impulses are slightly shifted to the following time instants:

$$T_n(0) = 0 \qquad (45)$$

$$T_n(1) = 0.132 \times 10^{-6}\,\text{s} \tag{46}$$

$$T_n(2) = 0.37 \times 10^{-6}\,\text{s} \tag{47}$$

Figures 12 and 13 show the amplitude and phase plots of the interpolation. Since the impulses are not on sampling points anymore, the si-functions are shifted and the resulting sum of si-functions does not become 0 at the sampling instants. These residuals are called interpolation artefacts.

Every echo is represented by a $sin(x)/x$ function. The sum of all these functions is the interpolation result, as seen in the Figure as a black curve. This result is sampled at the sampling instants given by the x-axis ticks and the corresponding red crosses. These values directly represent the FIR coefficients that can be used later in simulation program for the interpolation process.

FIGURE 12

Low-pass interpolation of the example echoes.
The instants in time when the impulses occur do not match sampling instants.
The LoS and the two echoes are illustrated as magenta Dirac-like stems with circles on top.
A weighted *sin(x)/x* function represents every echo (green, red and blue curves). The resulting
sum is given by the black line. The sampled FIR coefficients are represented by red crosses.
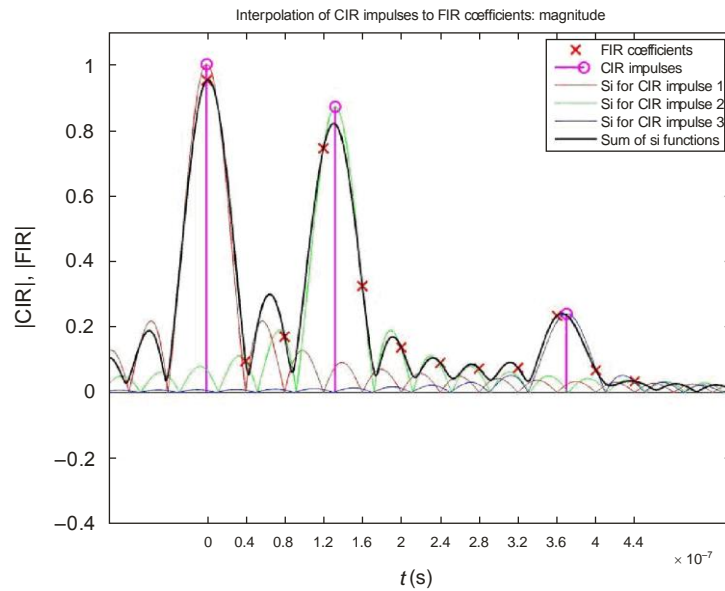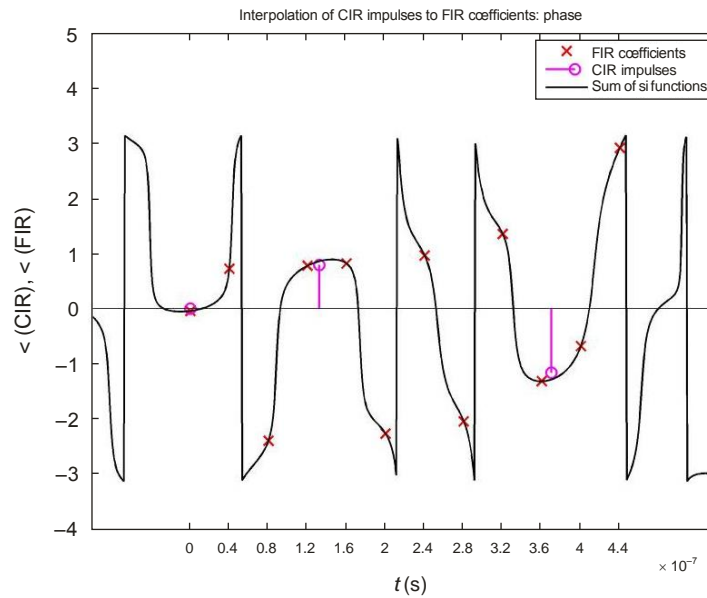**This plot shows the data component's magnitude**

Report P. 2145-12

FIGURE 13

Same as Fig. 12, but this plot shows the data component's phase

Report P. 2145-13

3.7.3 Interpolation of time-continuous Dirac input impulses in frequency domain

Another interpolation method can be formulated using Fourier transform. Since the Fourier transform of the Dirac function $\delta(t)$ is given by:

$$\Im\{\delta(t)\} = 1 \tag{48}$$

the Fourier transform's linearity is given by Sklar [1998]:

$$\Im\{A \cdot f(t)\} = A \cdot F(\omega) \tag{49}$$

and the Fourier transform's time-shift property states Sklar [1998]:

$$\Im\{f(t-\tau)\} = F(\omega)e^{-j\omega\cdot\tau} \tag{50}$$

Where $\omega = 2\pi f$. An echo at time instant δ_0 with weight A can thus be transformed to frequency domain using:

$$\Im\{A \cdot \delta(t-\tau)\} = A \cdot e^{-j\omega\cdot\tau} \tag{51}$$

A CIR consisting of multiple echoes can thus be calculated by a sum of such complex exponential functions:

$$\Im\left\{\sum_{n=0}^{N} A_n \cdot \delta(t-\tau_n)\right\} = \sum_{n=0}^{N} A_n \cdot e^{-j\omega\cdot\tau_n} \tag{52}$$

Figures 14 and 15 show the magnitude and phase plot of this Fourier transform with the given sample echoes.

The subsequent step is to carry out the inverse Fourier transform of this frequency domain signal to obtain the interpolated points in time domain. The result of this computation using the inverse discrete Fourier transform (IDFT) is shown as magnitude plot in Fig. 16 and phase plot in Fig. 17.

The comparison of the low-pass interpolation result's phase plot (the red crosses in Fig. 13) and the frequency domain version (the red crosses in Fig. 17) shows a much smoother and realistic phase transitions for the interpolated FIR coefficients that originated by the frequency domain method. The phase jumps that occur from one red-crossed point to the other for the time domain version might severely affect a simulation program. In contrary, the frequency domain result provides a very linear phase characteristic in between the instance where the Dirac impulses occurred.

FIGURE 14

Interpolation in frequency domain: Sum of complex exponential functions and the resulting FIR coefficients. The magnitude is shown
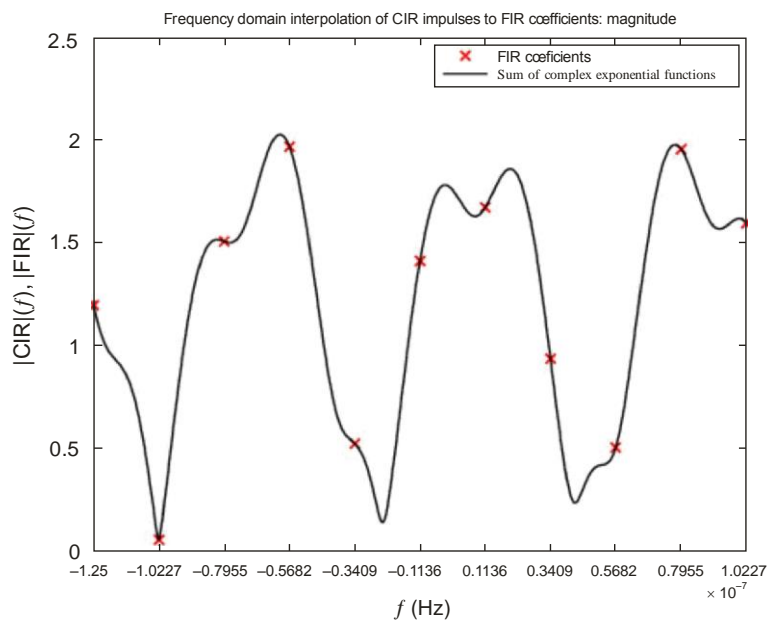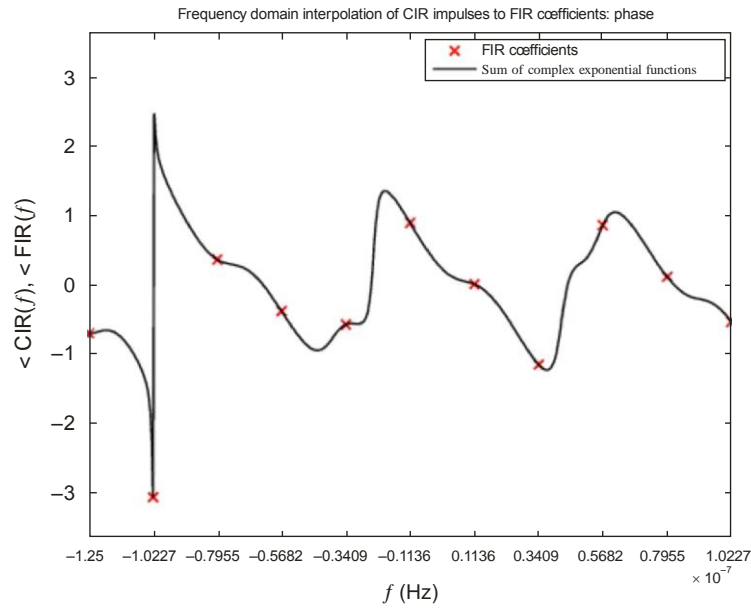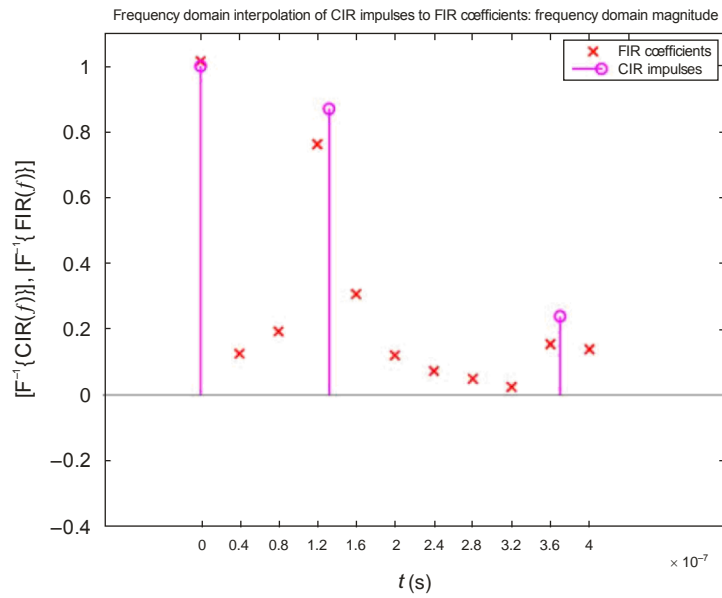

Report P. 2145-14

FIGURE 15

**Interpolation in frequency domain: Sum of complex exponential functions
and the resulting FIR coefficients. The phase is shown**

Frequency domain interpolation of CIR impulses to FIR cœfficients: phase
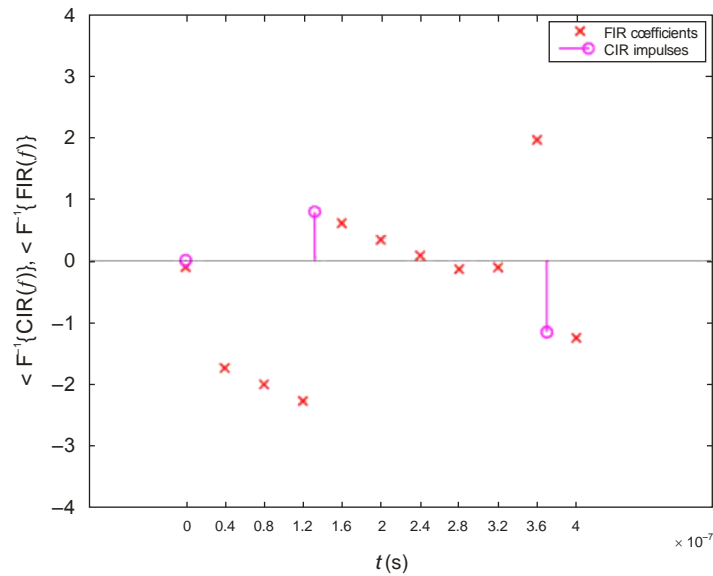

Report P. 2145-15

FIGURE 16

**The inverse Fourier transform of data given in Figs 14 and 15
leads to the wanted FIR coefficients in time domain.
The coefficients' magnitude is plotted**

Frequency domain interpolation of CIR impulses to FIR cœfficients: frequency domain magnitude

Report P. 2145-16

FIGURE 17

**The inverse Fourier transform of data given in Figs 14 and 15
leads to the wanted FIR coefficients in time domain.
The coefficients' phase is plotted**

Report P. 2145-17

3.7.4 Comparison of the interpolation methods with a sampling frequency of 100 MHz

All examples above where calculated using a sampling frequency of 25 MHz. The effect of the phase distortions which are caused by the low-pass interpolation becomes even more visible, when a higher sampling rate is chosen. The following four plots provide the direct comparison between low-pass and frequency domain interpolation of the example data at 100 MHz. Figures 18 and 19 show the magnitude and phase plot of the low-pass interpolation result and Figs 20 and 21 show the result for the frequency domain method. Once again, the phase response of the frequency domain method is very linear whereas the low-pass interpolation generates high phase jumps which will cause negative influences on a simulation routine.
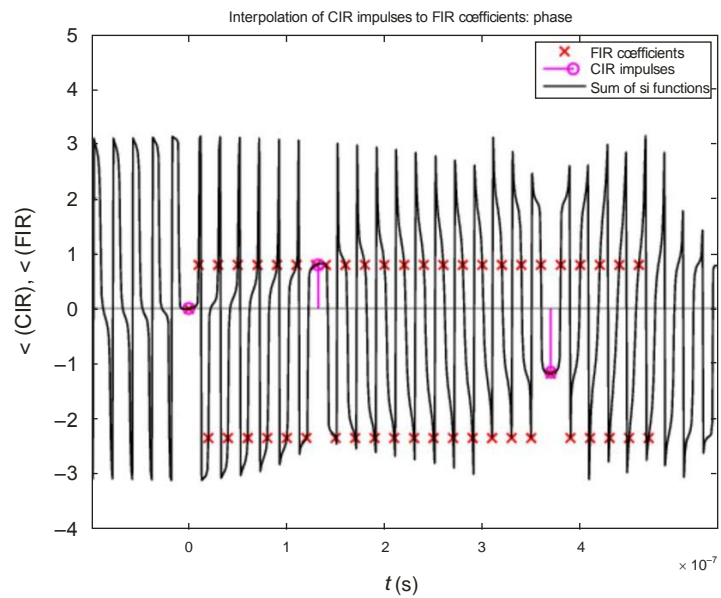
FIGURE 18

**Low-pass interpolation of sample impulses at 100 MHz
sampling frequency. Magnitude plot**
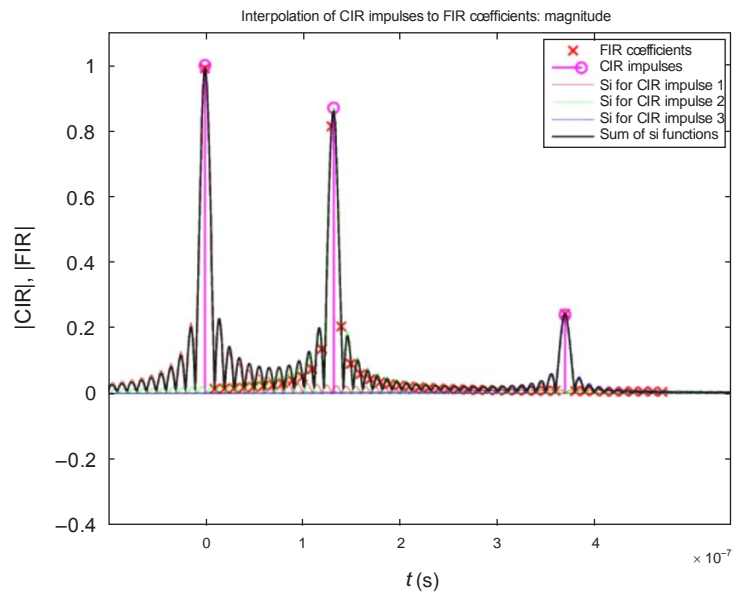
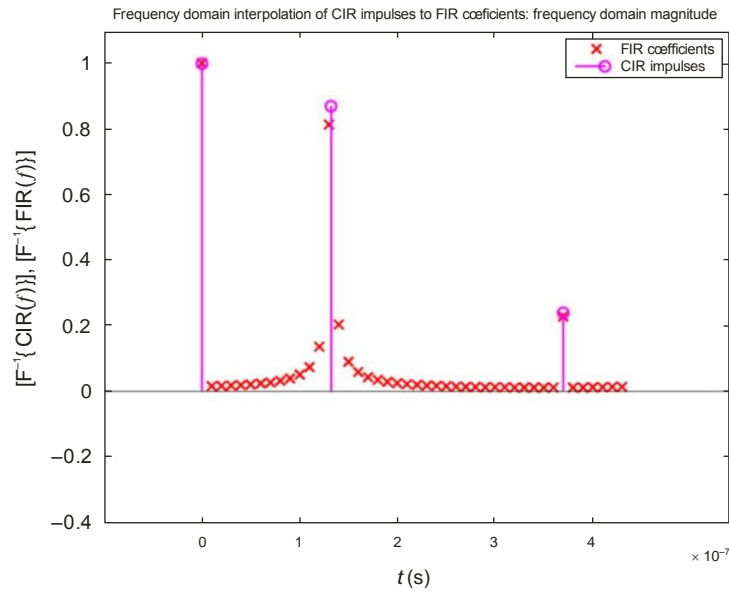Report P. 2145-18

FIGURE 19

**Low-pass interpolation of sample impulses at 100 MHz sampling frequency.
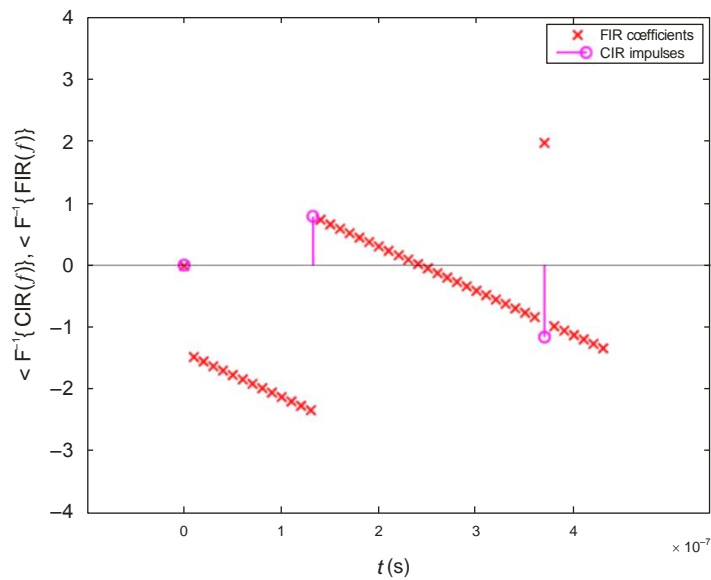Phase plot**

Report P. 2145-19

FIGURE 20

**Frequency domain interpolation of sample impulses at 100 MHz sampling frequency.
Magnitude plot**

Report P. 2145-20

FIGURE 21

**Frequency domain interpolation of sample impulses at 100 MHz sampling frequency.
Phase plot**

Report P. 2145-21

4 Report on physical-statistical wideband LMSS model in urban and suburban scenarios in Munich

In this section, the measurements used to derive the model parameters are described. Data for the following environments are provided:

– Urban vehicle

– Suburban vehicle

–   Urban pedestrian

–   Suburban pedestrian

4.1   Environment description

4.1.1   Urban measurements

The measurements for the urban environment have been carried out in Munich (Germany). From the beginning of these measurements the satellite elevation has been seen as an important parameter for the measurement. Therefore the track of the measurement receiver has been selected in a way that it is highly concentrated around the centre spot of the measurement. This ensured that although the car was driving along its track the elevation is not changing very much during one measurement. Although this requirement was fulfilled the track has been selected to provide typical mixture of architecture for this environment.

Figure 22 shows the car track in the "Lindwurmstrasse" area in Munich. This road is one of the main roads of the capital of the German federal state of Bavaria. The track was followed by narrow roads, street canyons and large squares. For this low elevation the visibility of the satellite is naturally quite low as well.

FIGURE 22

Measurement Area "Urban" in Munich

Report P. 2145-22

Figure 23 shows a typical wide road in Munich. In these roads trees can often be found on the sides of the road. The buildings are typically around 6 floors high. The road has 4-6 lanes in total.

FIGURE 23

Measurement Area "Lindwurmstrasse" in Munich

Report P. 2145-23

Figure 24 shows a typical narrow street in Munich. This scenario is the often feared "urban canyon". It has only 2-4 lanes in total but in contrast to the wide street scenario most of the sky is shadowed.

FIGURE 24

Measurement Area "Oberanger" in Munich

Report P. 2145-24

4.1.2 Suburban city

The suburban measurements have been performed in the small town of Fürstenfeldbruck near Munich (48°10'39.02"N, 11°15'22.12"E). Figure 25 gives an impression of the measurement area. In comparison to the city of Munich the buildings of Fürstenfeldbruck are significantly lower (usually only three floors) and the streets are wider (see Figs 26 and 27).

FIGURE 25

Measurement Area "Suburban" in Fürstenfeldbruck
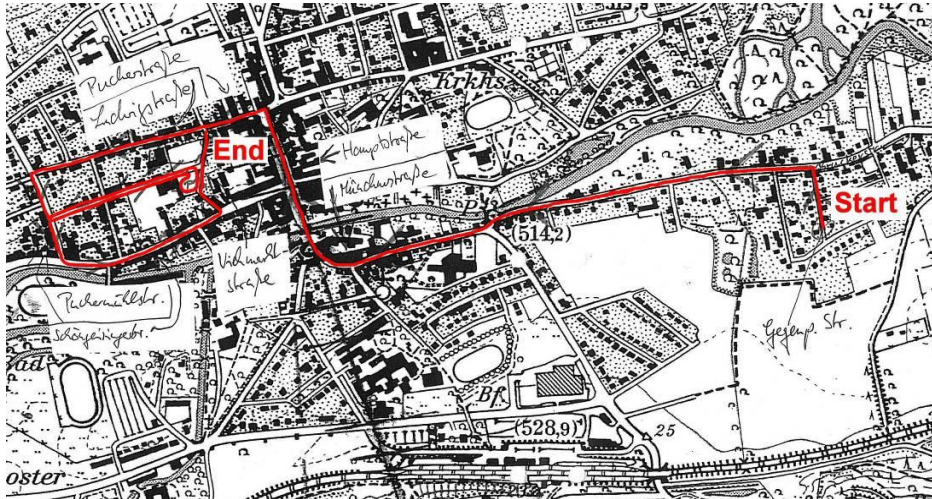
Report P. 2145-25

FIGURE 26

City of Fürstenfeldbruck – Main street – View N to S

Report P. 2145-26

FIGURE 27

City of Fürstenfeldbruck – Main street – View S to N

Report P. 2145-27

4.2 Model description of scenario specific features

As described in the previous section, the model was developed from measurements in an urban scenario in both the old town and the modern part of Munich, Germany. Munich is one of the largest cities in Germany. The following scenarios are incorporated into the statistics:

– Wide streets, 30-50 m

– Narrow streets, 20-25 m

– City squares.

The model contains a set of parameters that can be configured to adapt the house fronts, trees and light poles in the environment. In § 4.3.2, a scenario is provided that matches the situation of the measured environment. The parameters can be tuned to other environments; however, those changes only affect the direct signal. For an accurate representation of the scenario, all scenario-dependent parameters in Table 2 would need to be estimated.

The data are included in data files available in the model software implementation. The File Interface Description for the files is given in § 5.

TABLE 2

Scenario-dependant parameters and functions extracted from data files

| Parameter	Description	Value
γ_{tree}	Specific attenuation (dB/m) for the deterministic part of tree attenuation A_{cyl}	See § 4.3.3
K_{tr}	Rice factor tree attenuation Ricean fading process A_{stoch}	30
B_{tr}	3 dB bandwidth of tree attenuation Ricean fading process A_{stoch}	0.437 (1/m)

TABLE 2 (*end*)

| Parameter	Description	Value
$p_{r,\psi}(\varepsilon)$	Probability density of a reflector being present at the horizontal position, r, ψ, assuming an equal distribution of the satellite azimuth φ	See Fig. 28
$p_{\alpha\text{-}\varphi}(\varepsilon)$	Probability density of a reflector being present at the relative direction between the azimuth φ and the angle α between reflector and satellite seen from the receiver	See Fig. 29
$\mu(r,\psi,\varepsilon)$	Power mean at the relative position (r,ψ) observed in the measurement for the satellite elevation ε	See Fig. 30
$\sigma(r,\psi,\varepsilon)$	Power variance at the relative position (r,ψ) observed in the measurement for the satellite elevation ε	See Fig. 31
B_e	3 dB bandwidth of the echo selected from the Gaussian probability density function $p_{be}(\varepsilon)$ with mean and variance depending on elevation ε	See Figs 32 and 33
K	Rice factor of the echo fading Ricean process	See Fig. 34
$P_{ls}(\varepsilon)$	Cumulative distribution function of the life span of a reflector as a function of elevation ε	See Fig. 35
$\Pr(\text{mov}_{refl} \xleftrightarrow[\text{parallel}]{} \text{mov}_{Rx}/\varepsilon)$	Probability that a reflector moves parallel to the receiver, depending on elevation ε	See Fig. 36
$\overline{N}(\varepsilon)$	Constant describing the average number of echoes as a function of elevation ε	See Fig. 37
$\text{PSD}\{N(x,\varepsilon)\}$	Power spectral density of the process (narrow-band plus wideband) describing the number of echoes as a function of elevation ε	See Fig. 38

4.2.1 Urban vehicle

FIGURE 28

Probability density of a reflector being present at a horizontal position relative to the receiver
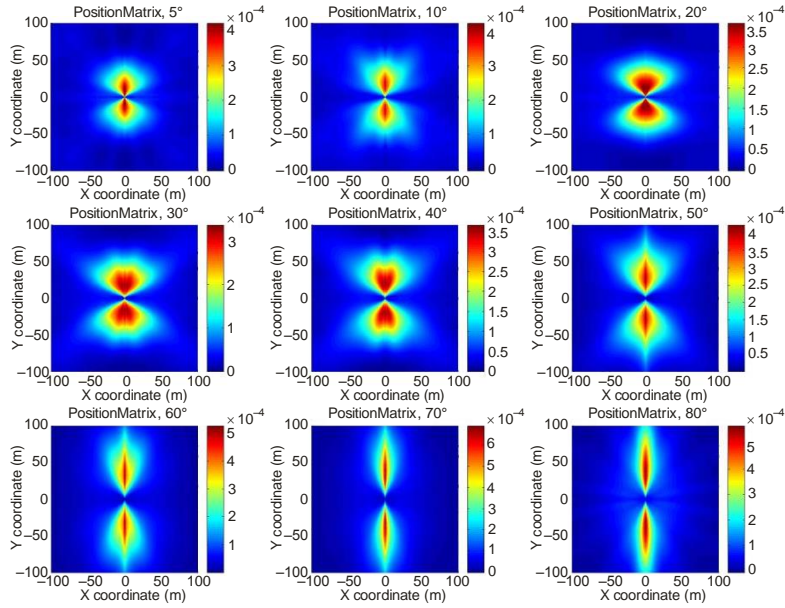
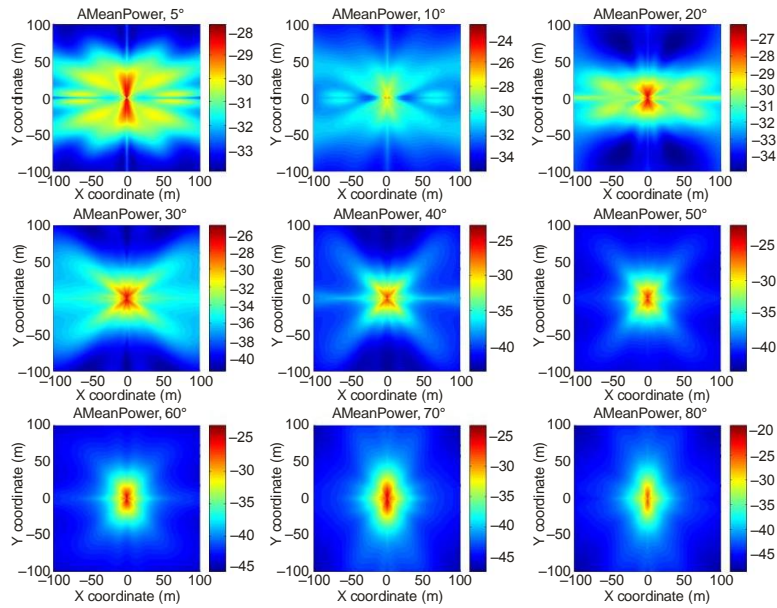
Report P. 2145-28

FIGURE 29

Likelihood of a reflector being present at a certain relative azimuth angle between reflector and LoS
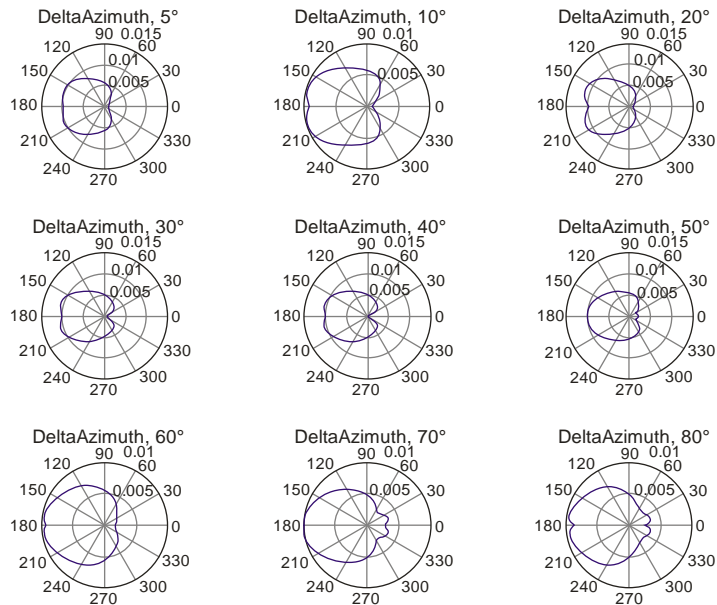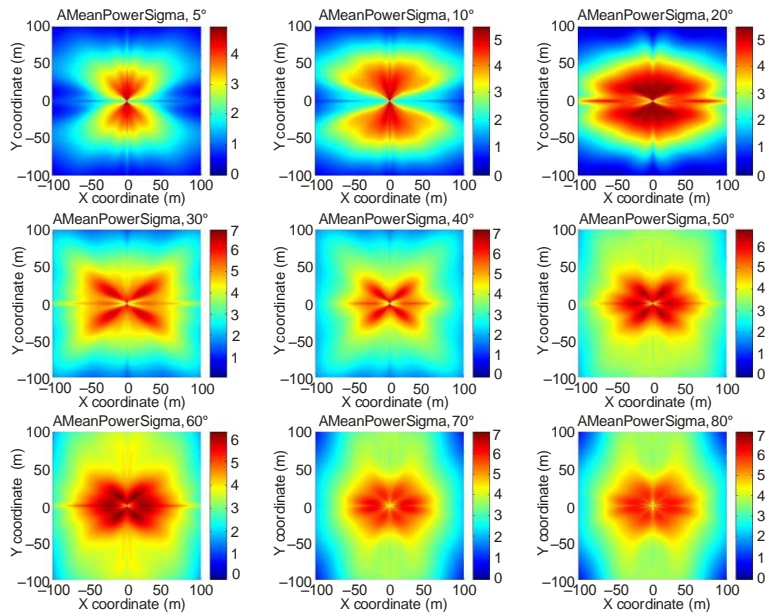

Report P. 2145-29

FIGURE 30

**Mean power of a reflector for a certain horizontal
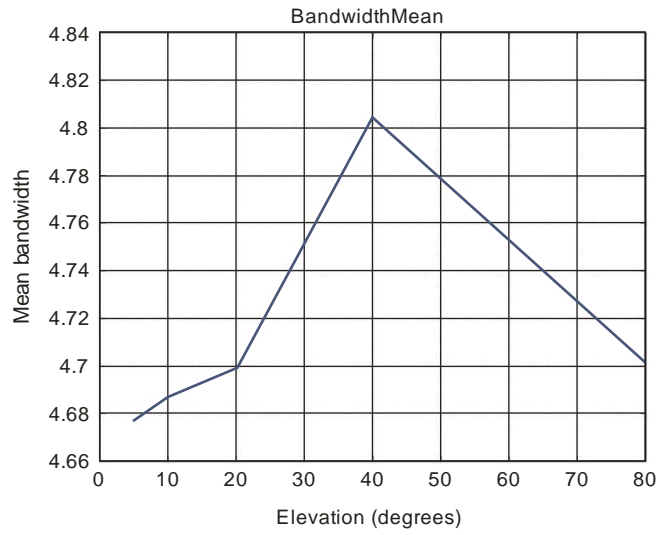position relative to the receiver**

Report P. 2145-30

FIGURE 31

**Standard deviation of the mean power of a reflector for a given
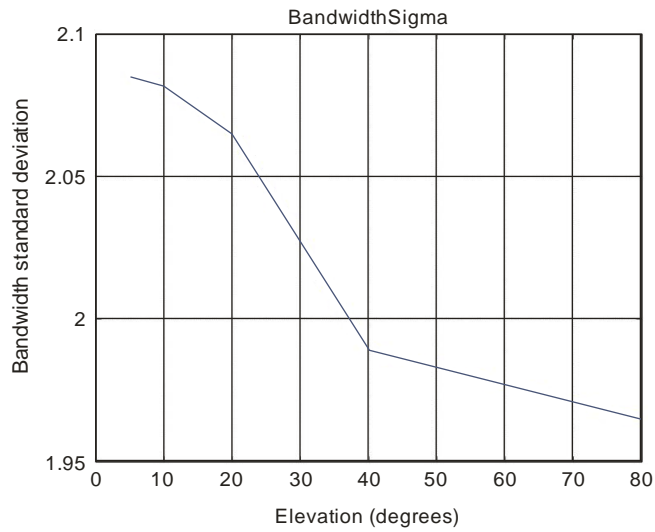relative horizontal position of a reflector**

Report P. 2145-31

FIGURE 32

**Mean value of the bandwidth of an echo as a function
of the satellite elevation**
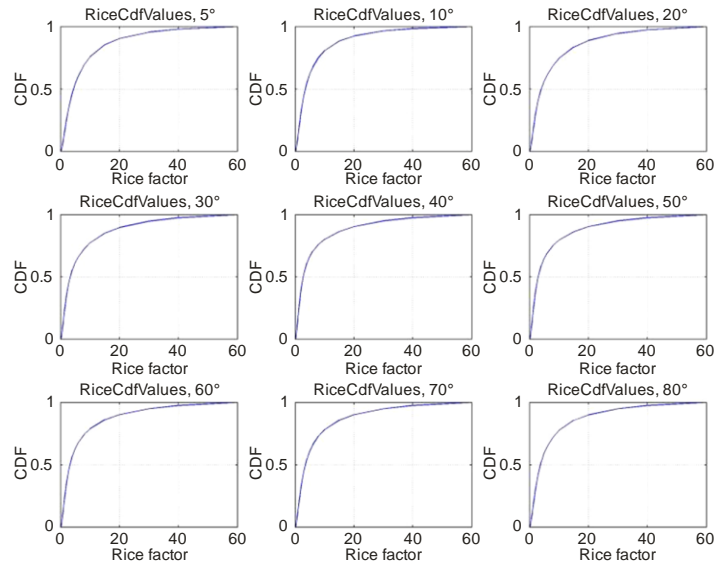

Report P. 2145-32

FIGURE 33

**Standard deviation of the bandwidth of an echo
as a function of the elevation angle**

Report P. 2145-33

FIGURE 34

**Cumulative distribution function of the Rice factors
as a function of the elevation angle**

Report P. 2145-34

FIGURE 35

**Cumulative density function of the life span as a function
of the elevation angle**
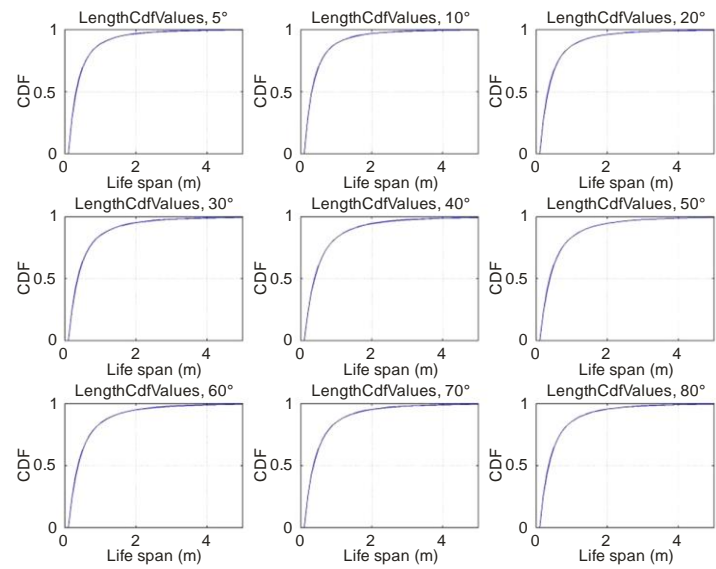
Report P. 2145-35

FIGURE 36

Probability that a reflector is moving in the same direction as the receiver as a function of the elevation angle
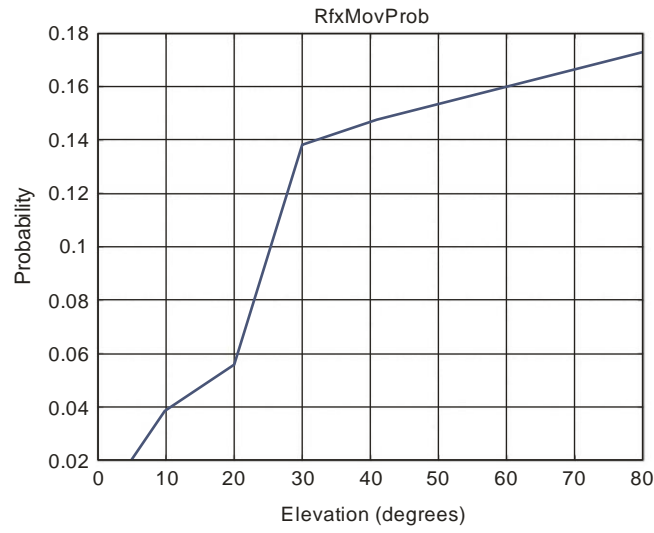
Report P. 2145-36

FIGURE 37

Mean number of coexisting reflectors as a function of the elevation angle

Report P. 2145-37

FIGURE 38

**Spectrum of the variation of the number of echoes over
distance travelled in the x direction**
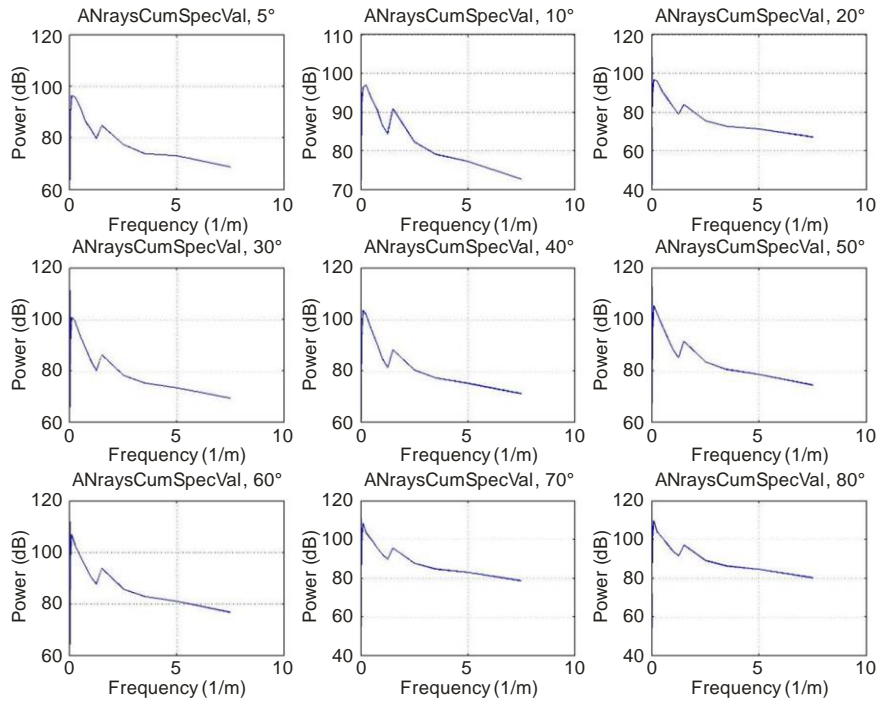
Report P. 2145-38

4.2.2 Suburban vehicle

FIGURE 39

**Probability density of a reflector being present at a
horizontal position relative to the receiver**
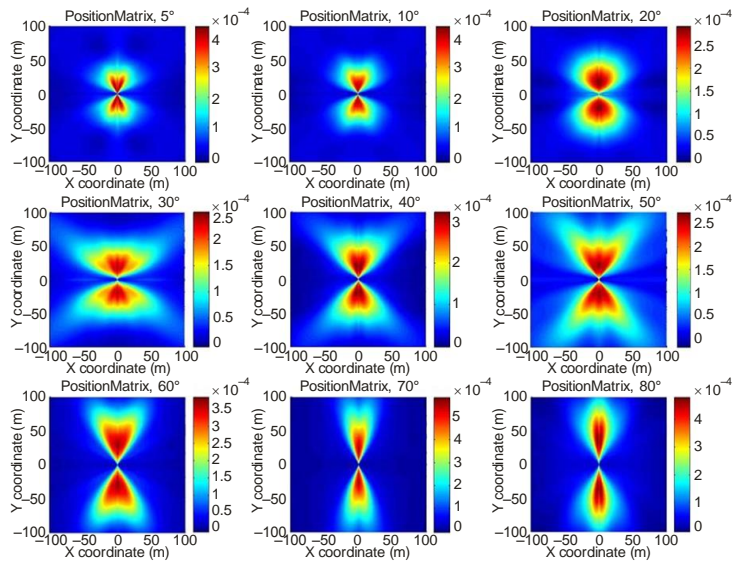
Report P. 2145-39

FIGURE 40

**Likelihood of a reflector being present at a certain relative
azimuth angle between reflector and LoS**
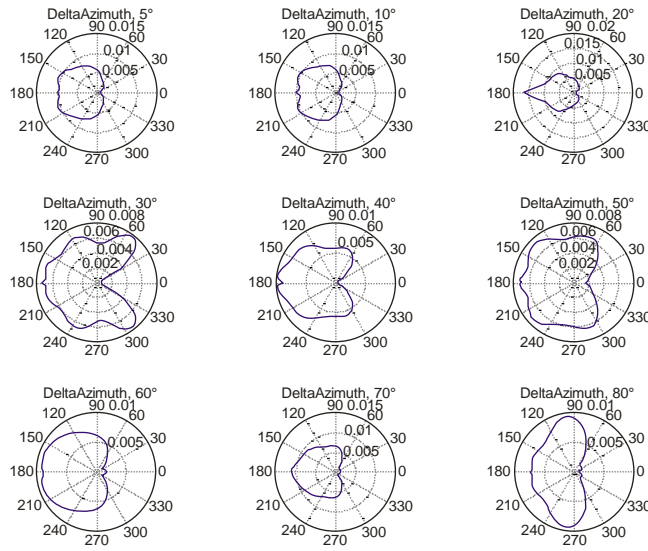
Report P. 2145-40

FIGURE 41

**Mean power of a reflector for a certain horizontal position
relative to the receiver**

Report P. 2145-41

FIGURE 42

**Standard deviation of the mean power of a reflector for a given relative
horizontal position of a reflector**

Report P. 2145-42

FIGURE 43

**Mean value of the bandwidth of an echo as a
function of the satellite elevation**

Report P. 2145-43

FIGURE 44

**Standard deviation of the bandwidth of an echo
as a function of the elevation angle**

Report P. 2145-44

FIGURE 45

**Cumulative distribution function of the Rice factors
as a function of the elevation angle**

Report P. 2145-45

FIGURE 46

**Cumulative density function of the life span as a
function of the elevation angle**
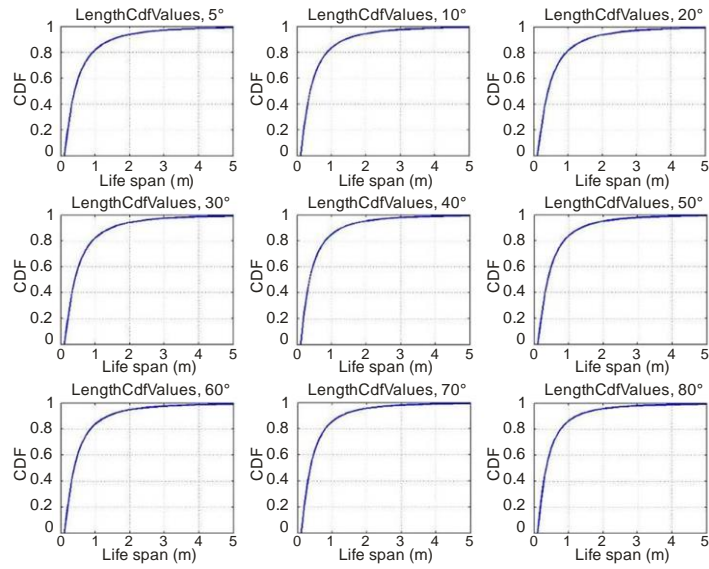
Report P. 2145-46

FIGURE 47

**Probability that a reflector is moving in the same direction as
the receiver as a function of the elevation angle**
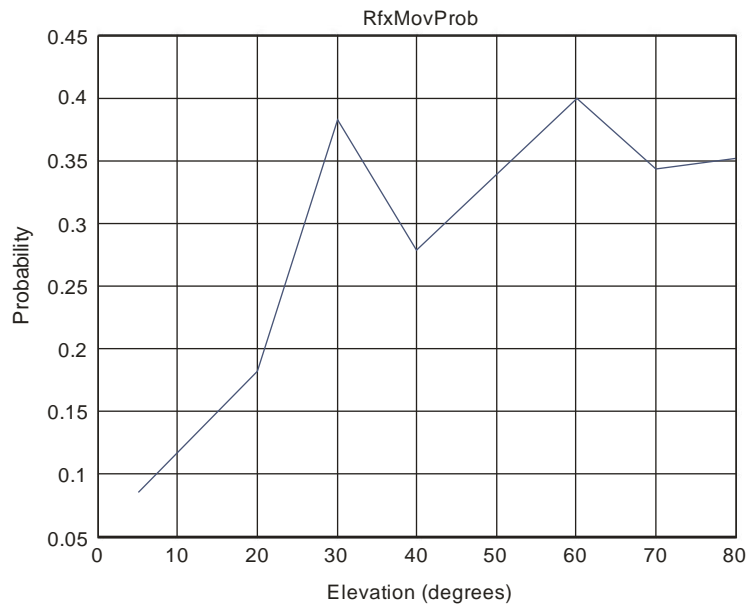
Report P. 2145-47

FIGURE 48

**Mean number of coexisting reflectors as a function
of the elevation angle**

Report P. 2145-48

FIGURE 49

**Spectrum of the variation of the number of echoes over
distance travelled in the x direction**
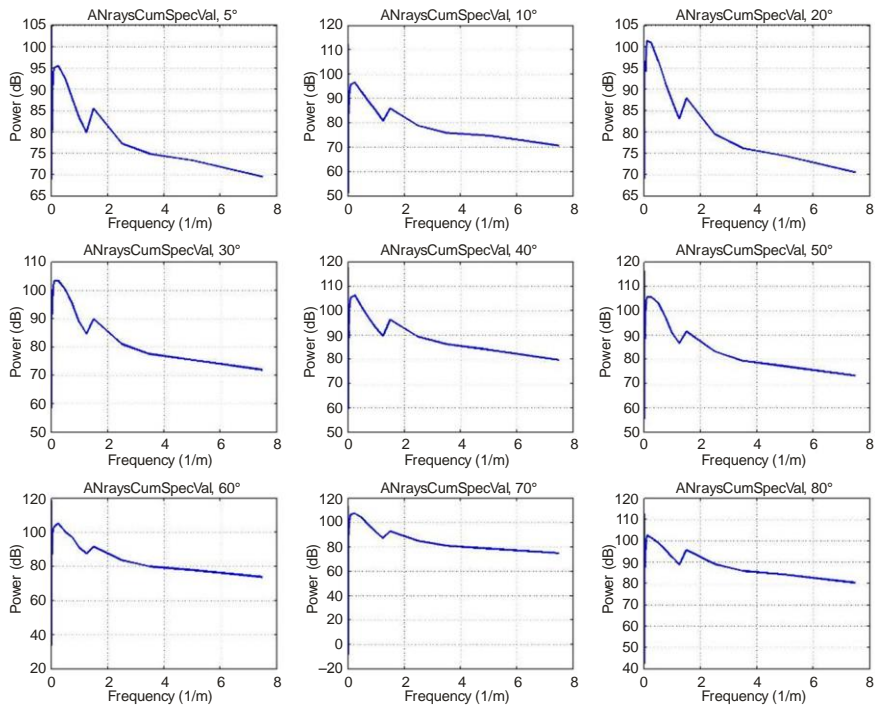
Report P. 2145-49

4.2.3 Urban pedestrian

FIGURE 50

Probability density of a reflector being present at a horizontal position relative to the receiver
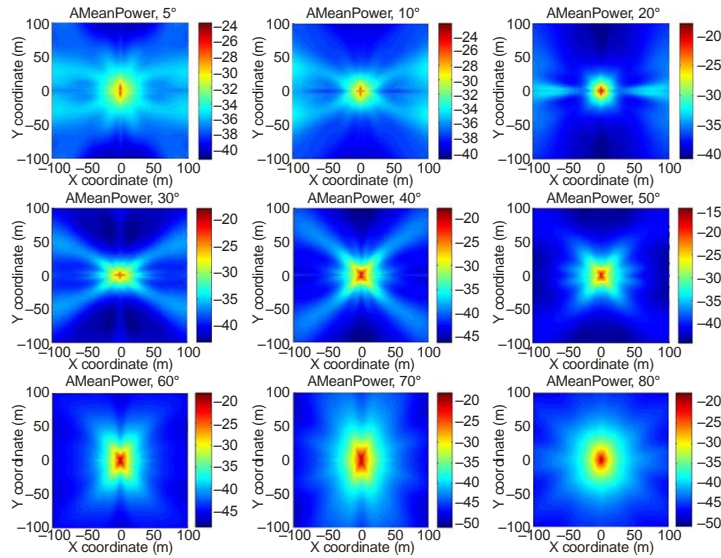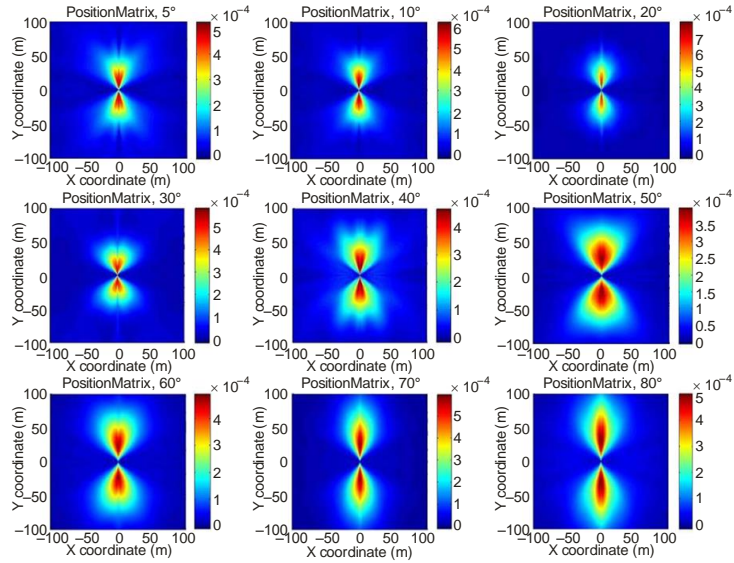

Report P. 2145-50

FIGURE 51

Likelihood of a reflector being present at a certain relative azimuth angle between reflector and LoS
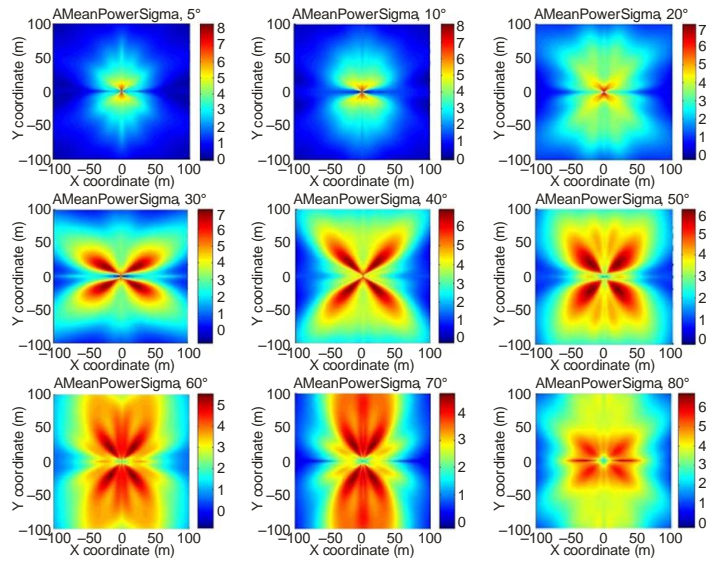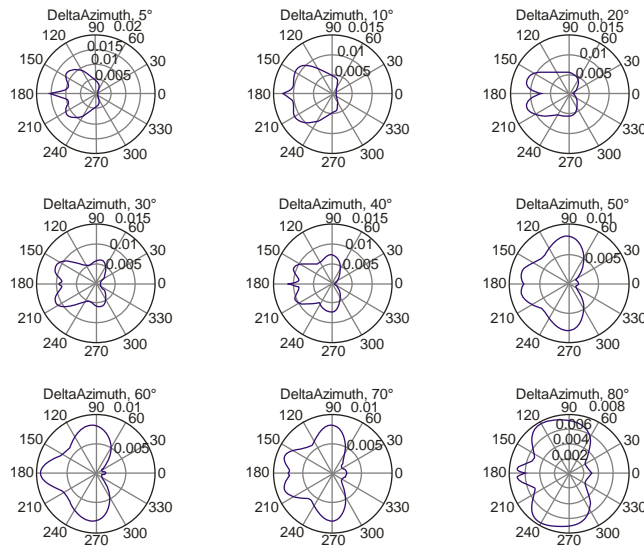

Report P. 2145-51

FIGURE 52

**Mean power of a reflector for a certain horizontal
position relative to the receiver**
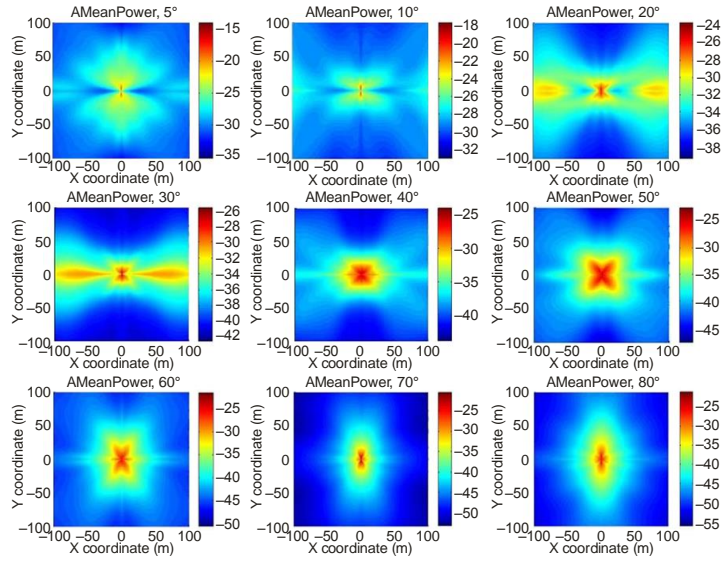
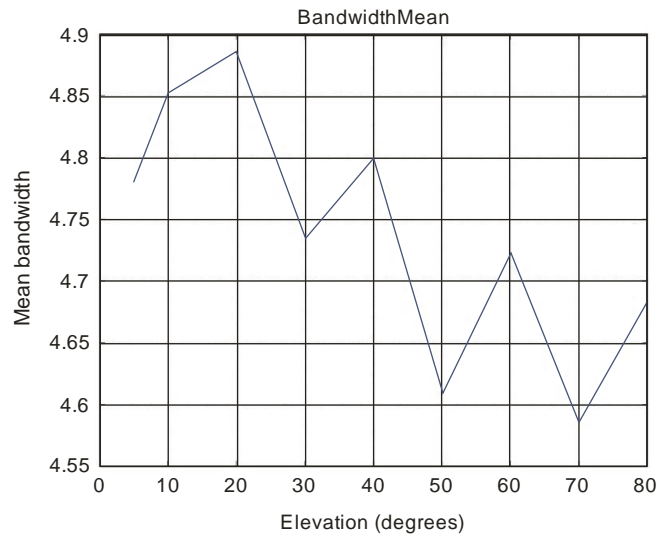Report P. 2145-52

FIGURE 53

**Standard deviation of the mean power of a reflector for a given
relative horizontal position of a reflector**
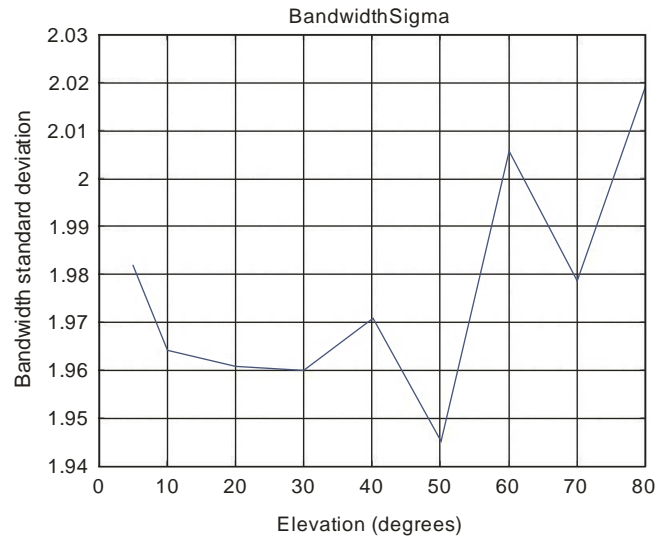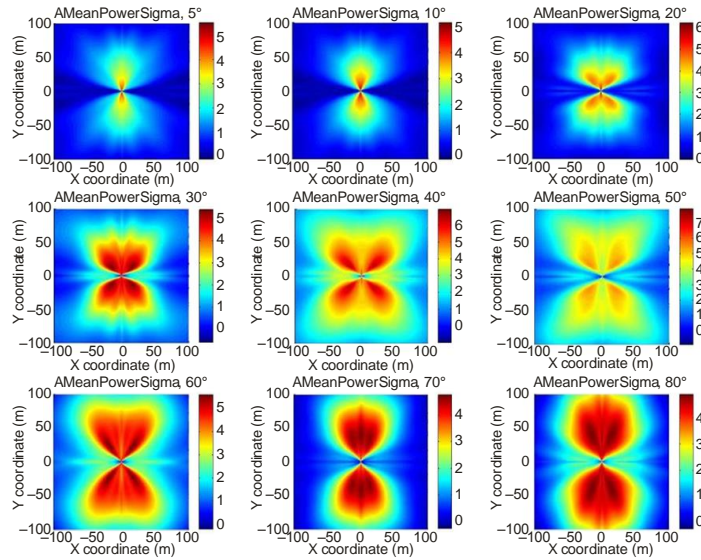

Report P. 2145-53

FIGURE 54

**Mean value of the bandwidth of an echo as a
function of the satellite elevation**
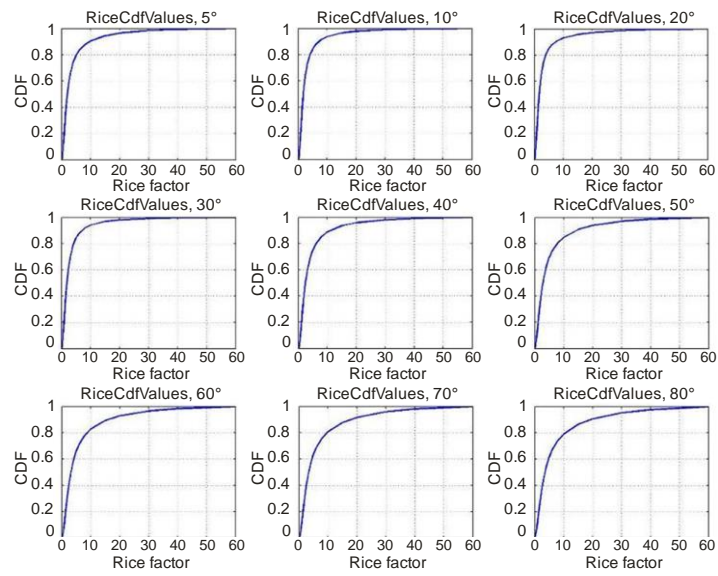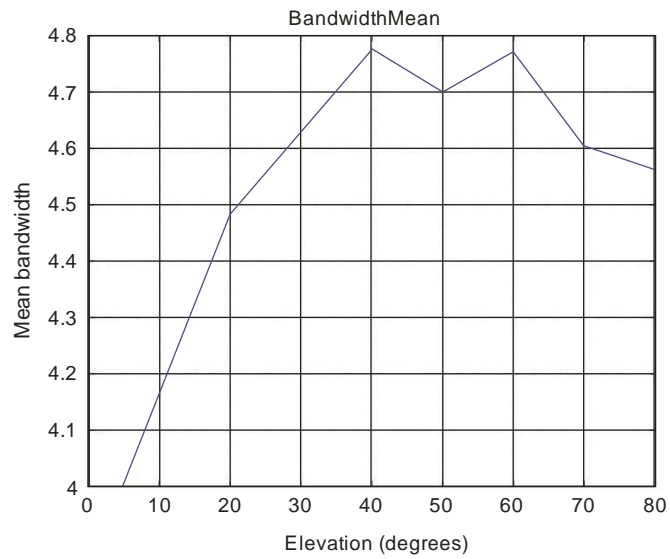

Report P. 2145-54

FIGURE 55

**Standard deviation of the bandwidth of an echo as a
function of the elevation angle**
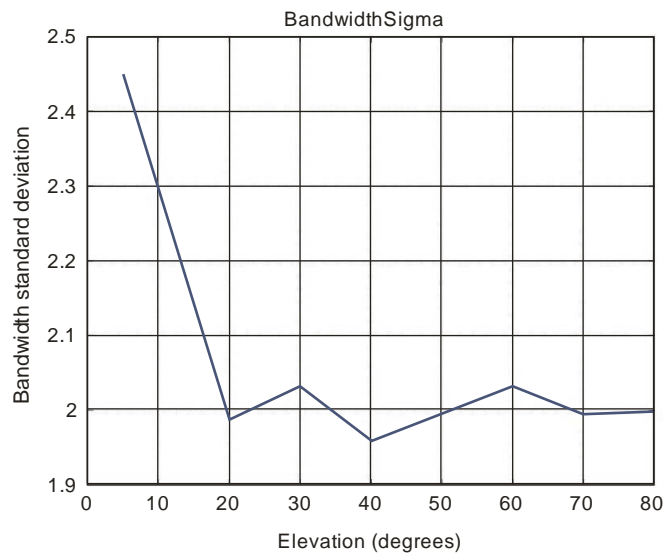
Report P. 2145-55

FIGURE 56

**Cumulative distribution function of the Rice factors
as a function of the elevation angle**
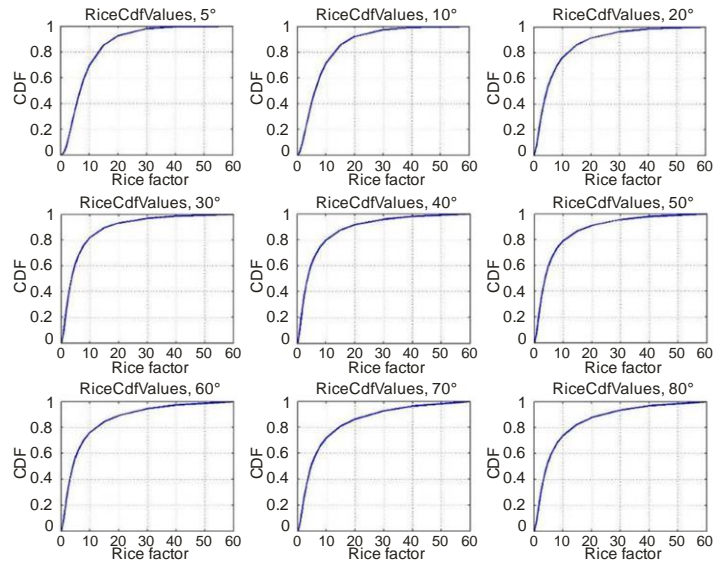
Report P. 2145-56

FIGURE 57

**Cumulative density function of the life span
as a function of the elevation angle**
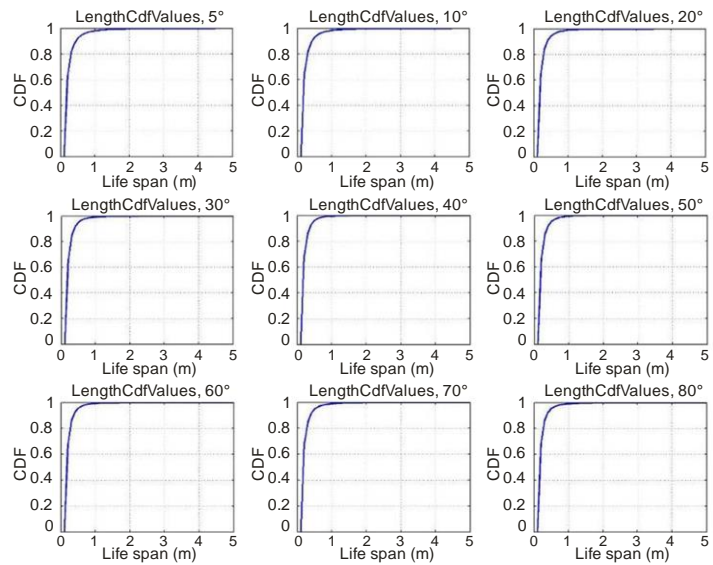
Report P. 2145-57

FIGURE 58

**Probability that a reflector is moving in the same direction as the
receiver as a function of the elevation angle**
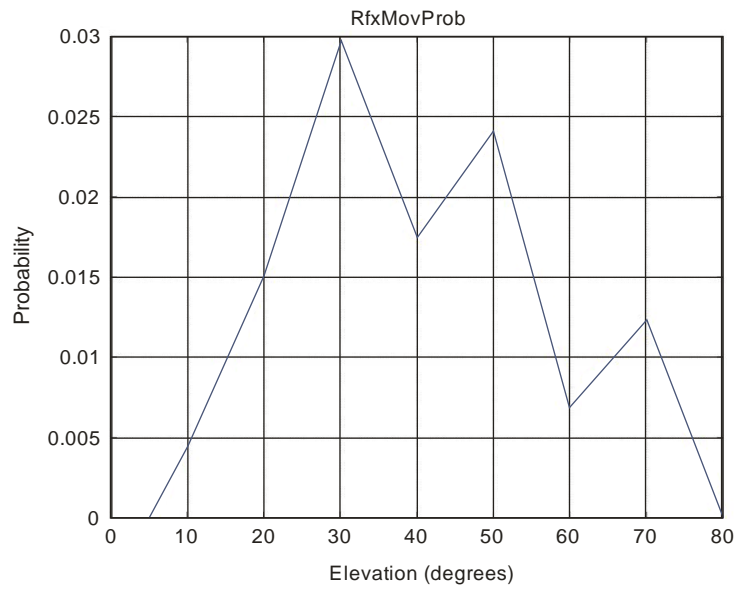
Report P. 2145-58

FIGURE 59

**Mean number of coexisting reflectors as a function
of the elevation angle**
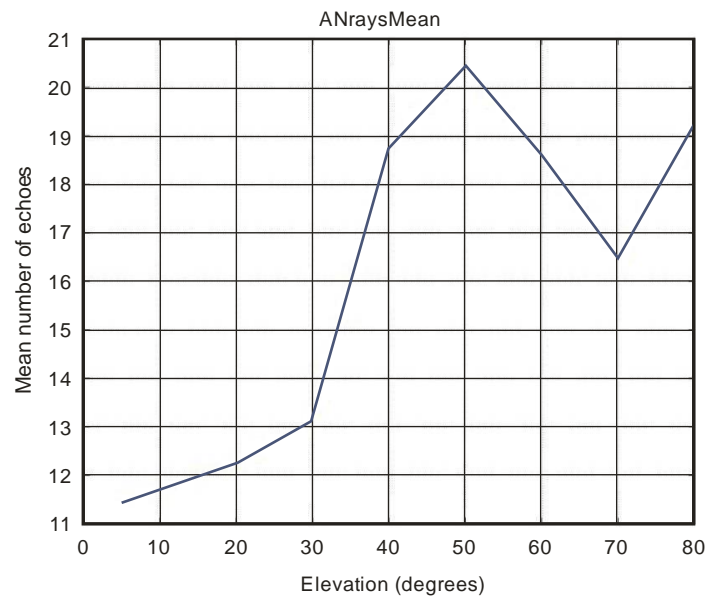
Report P. 2145-59

FIGURE 60

**Spectrum of the variation of the number of echoes over
distance travelled in the x direction**
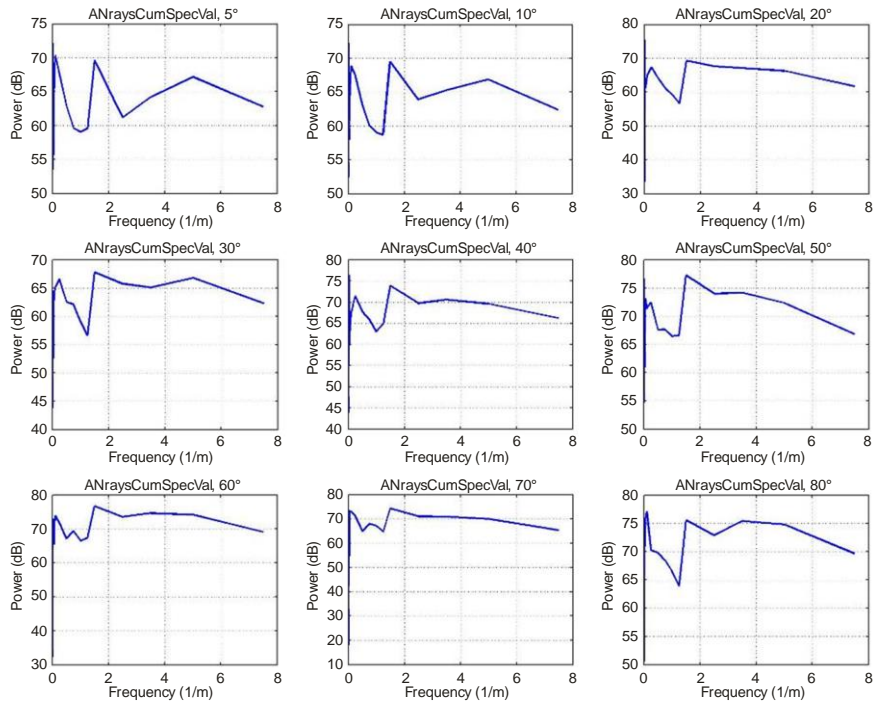
Report P. 2145-60

4.2.4 Suburban pedestrian

FIGURE 61

**Probability density of a reflector being present at a horizontal
position relative to the receiver**
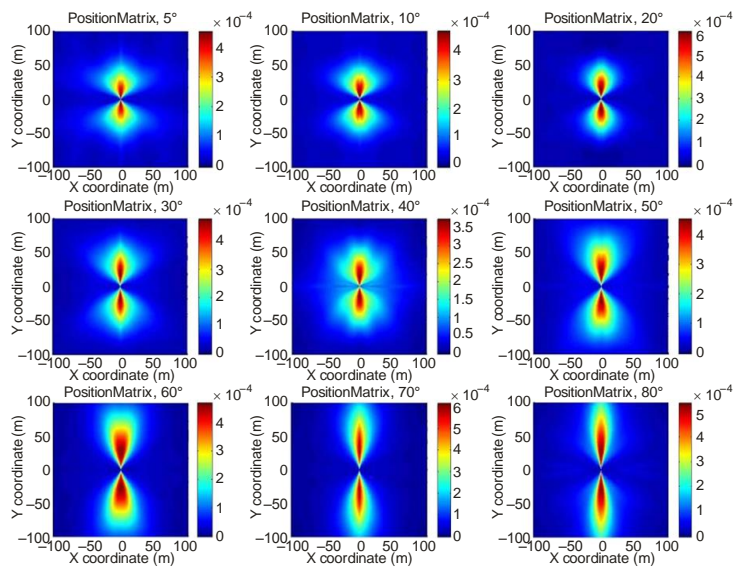
Report P. 2145-61

FIGURE 62

Likelihood of a reflector being present at a certain relative azimuth angle between reflector and LoS
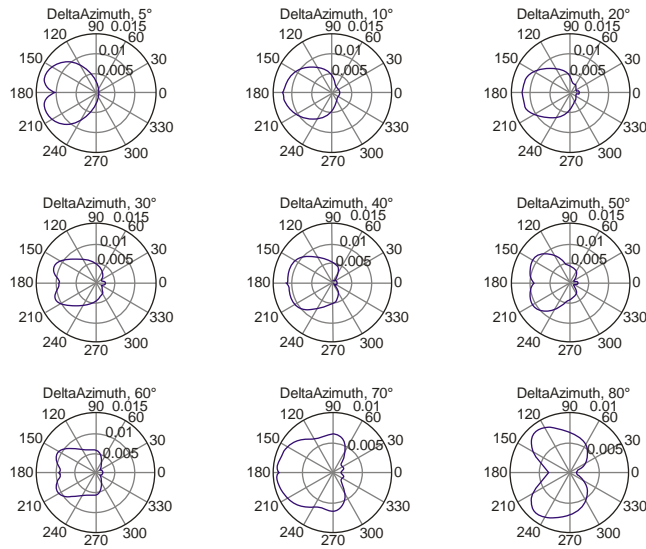
Report P. 2145-62

FIGURE 63

Mean power of a reflector for a certain horizontal position relative to the receiver
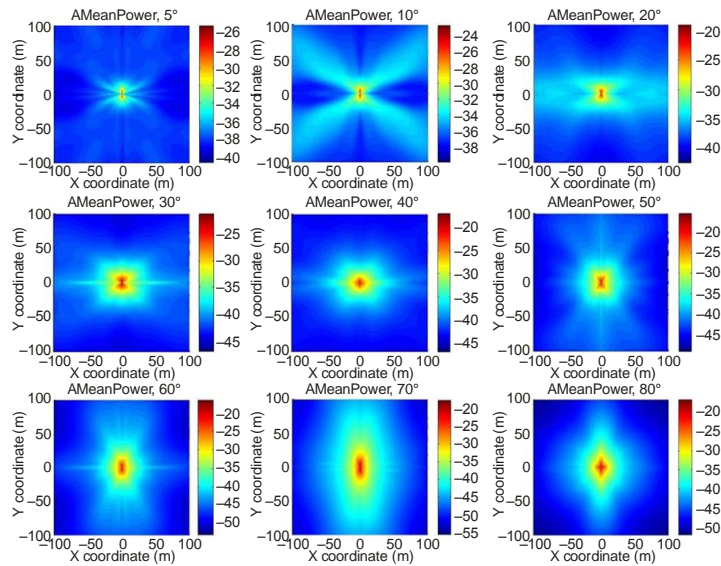
Report P. 2145-63

FIGURE 64

**Standard deviation of the mean power of a reflector for a given relative
horizontal position of a reflector**
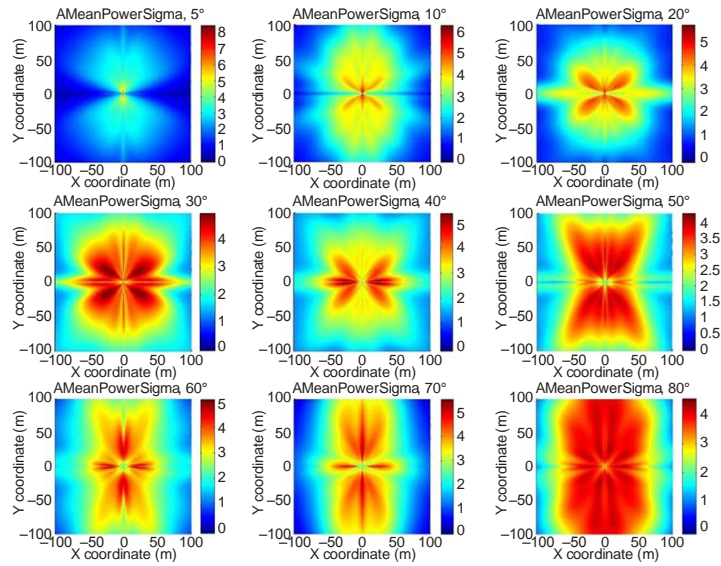
Report P. 2145-64

FIGURE 65

**Mean value of the bandwidth of an echo as a
function of the satellite elevation**
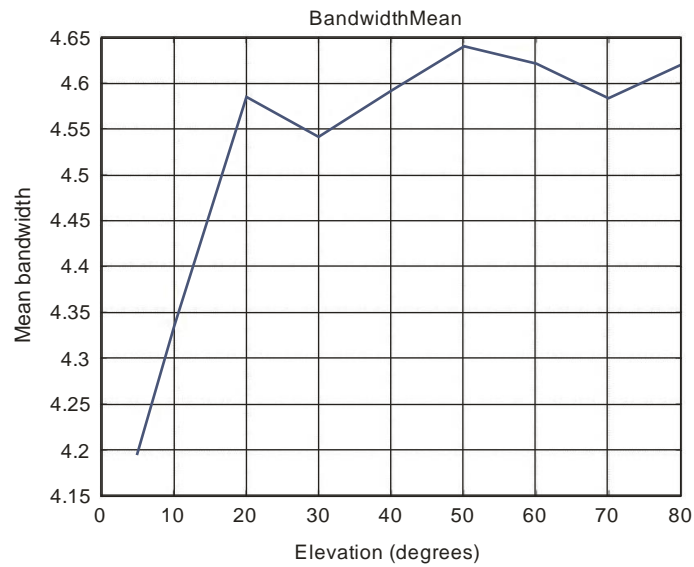
Report P. 2145-65

FIGURE 66

**Standard deviation of the bandwidth of an echo as a
function of the elevation angle**
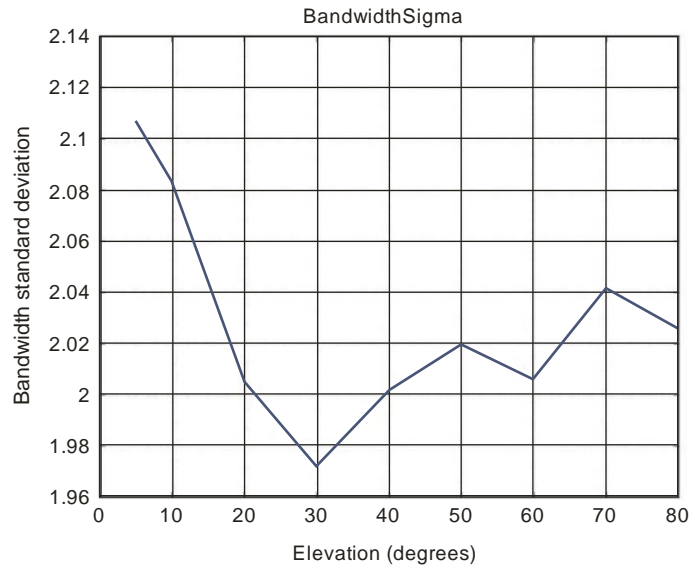
Report P. 2145-66

FIGURE 67

**Cumulative distribution function of the Rice factors as a
function of the elevation angle**
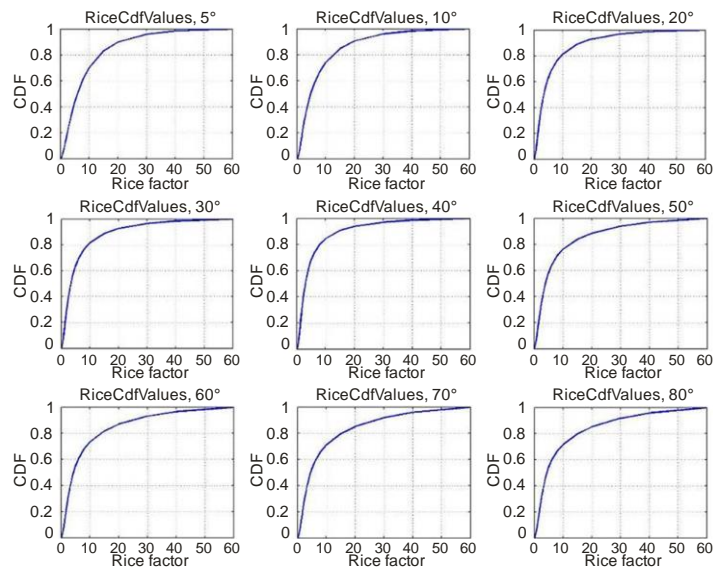
Report P. 2145-67

FIGURE 68

**Cumulative density function of the life span as a
function of the elevation angle**
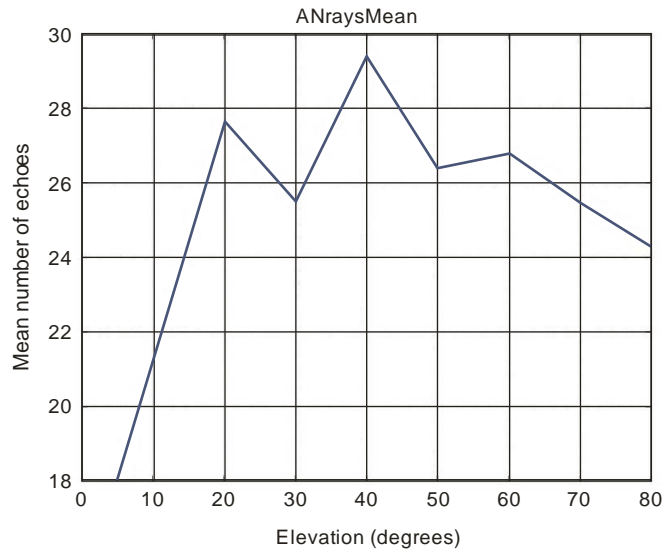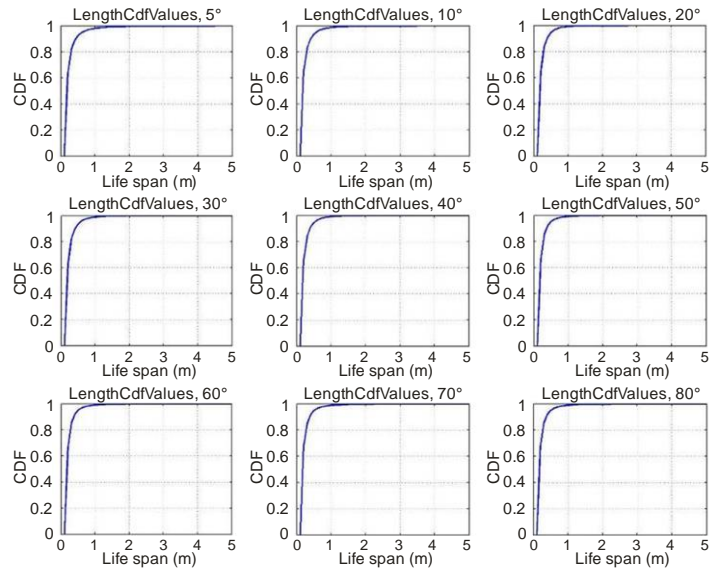

Report P. 2145-68

FIGURE 69

**Probability that a reflector is moving in the same direction as the
receiver as a function of the elevation angle**
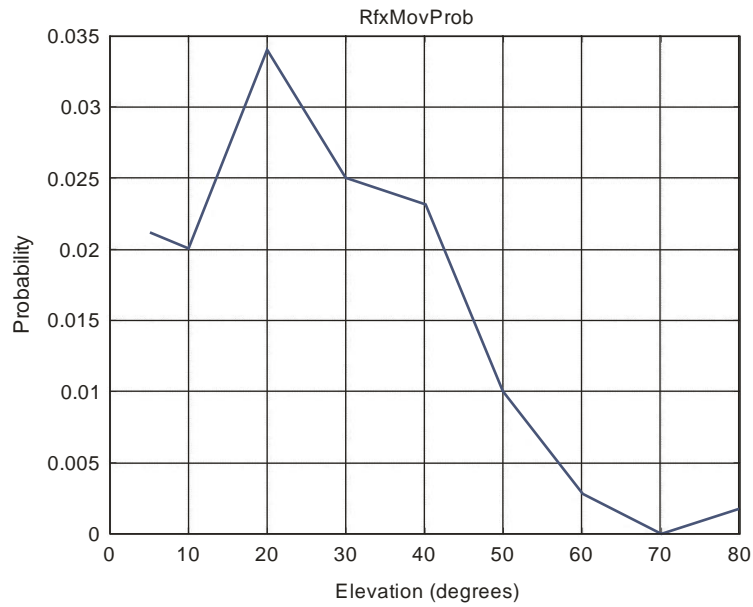
Report P. 2145-69

FIGURE 70

**Mean number of coexisting reflectors as a
function of the elevation angle**
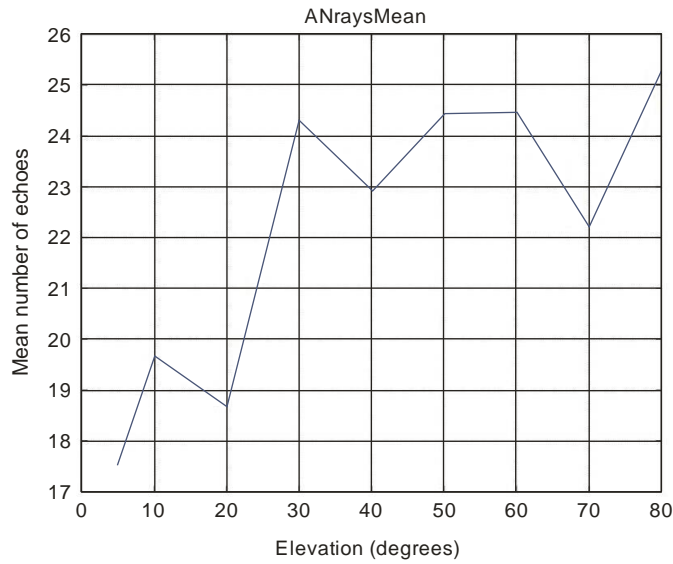
Report P. 2145-70

FIGURE 71

**Spectrum of the variation of the number of echoes over distance
travelled in the x direction**
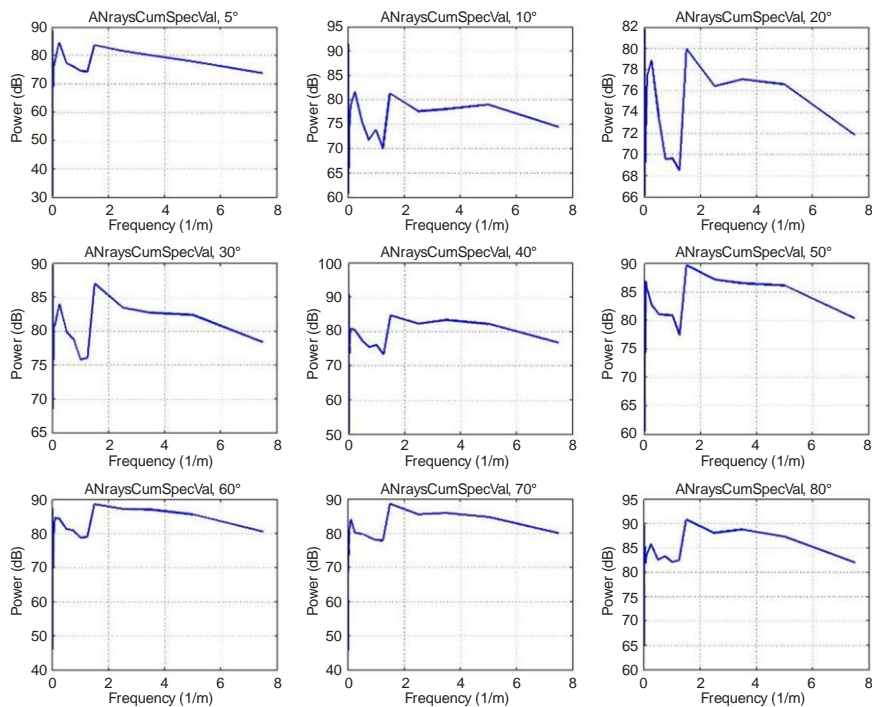
Report P. 2145-71

4.3 Geometric parameters

Although any observed parameter set can be used to initialize this model, the following parameter settings are currently recommended. These values have been derived from observations in Munich (Germany).

4.3.1 User parameters

Urban vehicle

DistanceFromRoadMiddle	m	−5

Suburban vehicle

DistanceFromRoadMiddle	m	−2

Urban pedestrian

DistanceFromRoadMiddle	m	−6.5

Suburban pedestrian

DistanceFromRoadMiddle	m	−5.5

FIGURE 72

User parameters and antenna placement
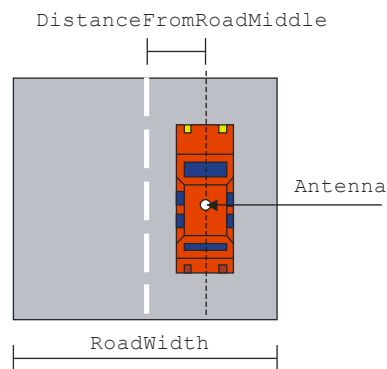
Report P. 2145-72

4.3.2 Building parameters

The building parameters set up the deterministic and statistical processes with respect to building shaping and placement. There are two rows of buildings that can be switched on. The building rows can be specified by a shaping process for house width and house height, and a placement process, which is governed by a gap-placing process. The Y-distance of the building rows is a fixed deterministic value.

Urban vehicle

BuildingRow1YPosition	m	−12
BuildingRow2YPosition	m	12
HouseWidthMean	m	22
HouseWidthSigma	m	25
HouseWidthMin	m	10
HouseHeightMean	m	16
HouseHeightSigma	m	6.4
HouseHeightMin	m	4
HouseHeightMax	m	50
GapWidthMean	m	27
GapWidthSigma	m	25
GapWidthMin	m	10
Gap Likelihood		0.18

Suburban vehicle

BuildingRow1YPosition	m	−7
BuildingRow2YPosition	m	7
HouseWidthMean	m	16
HouseWidthSigma	m	11
HouseWidthMin	m	5
HouseHeightMean	m	10
HouseHeightSigma	m	3.6
HouseHeightMin	m	3
HouseHeightMax	m	15
GapWidthMean	m	15
GapWidthSigma	m	22
GapWidthMin	m	2
Gap Likelihood		0.28

Urban pedestrian

BuildingRow1YPosition	m	−8
BuildingRow2YPosition	m	8
HouseWidthMean	m	22
HouseWidthSigma	m	25
HouseWidthMin	m	10
HouseHeightMean	m	16
HouseHeightSigma	m	6.4
HouseHeightMin	m	4
HouseHeightMax	m	50
GapWidthMean	m	27
GapWidthSigma	m	25
GapWidthMin	m	10
Gap Likelihood		0.18

Suburban pedestrian environment

BuildingRow1YPosition	m	7
BuildingRow2YPosition	m	7
HouseWidthMean	m	16
HouseWidthSigma	m	11
HouseWidthMin	m	5
HouseHeightMean	m	10
HouseHeightSigma	m	3.6
HouseHeightMin	m	3
HouseHeightMax	m	15
GapWidthMean	m	15
GapWidthSigma	m	22
GapWidthMin	m	2
Gap Likelihood		0.28

FIGURE 73

Building placement
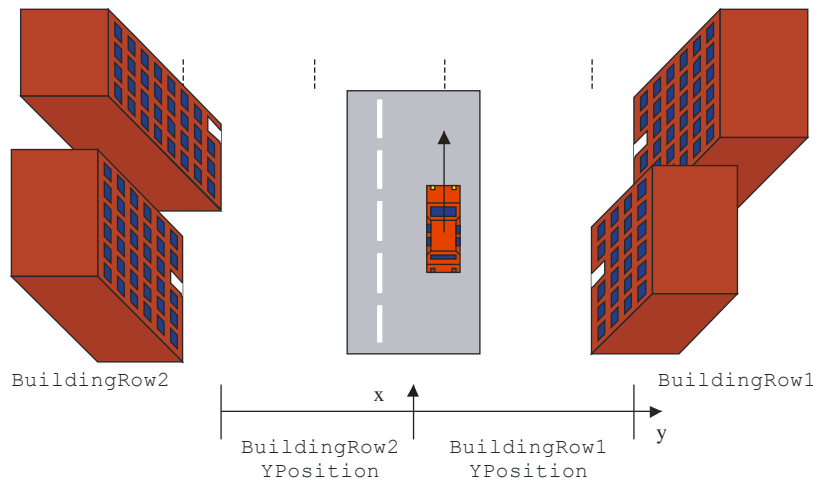
Report P. 2145-73

FIGURE 74

Building shaping and placement processes

ProcessHouseHeight:
HouseHeightMean
HouseHeightSigma
HouseHeightMin

ProcessHouseWidth:
HouseWidthMean
HouseWidthSigma
HouseWidthMin

ProcessGapWidth
GapWidthMean
GapWidthSigma
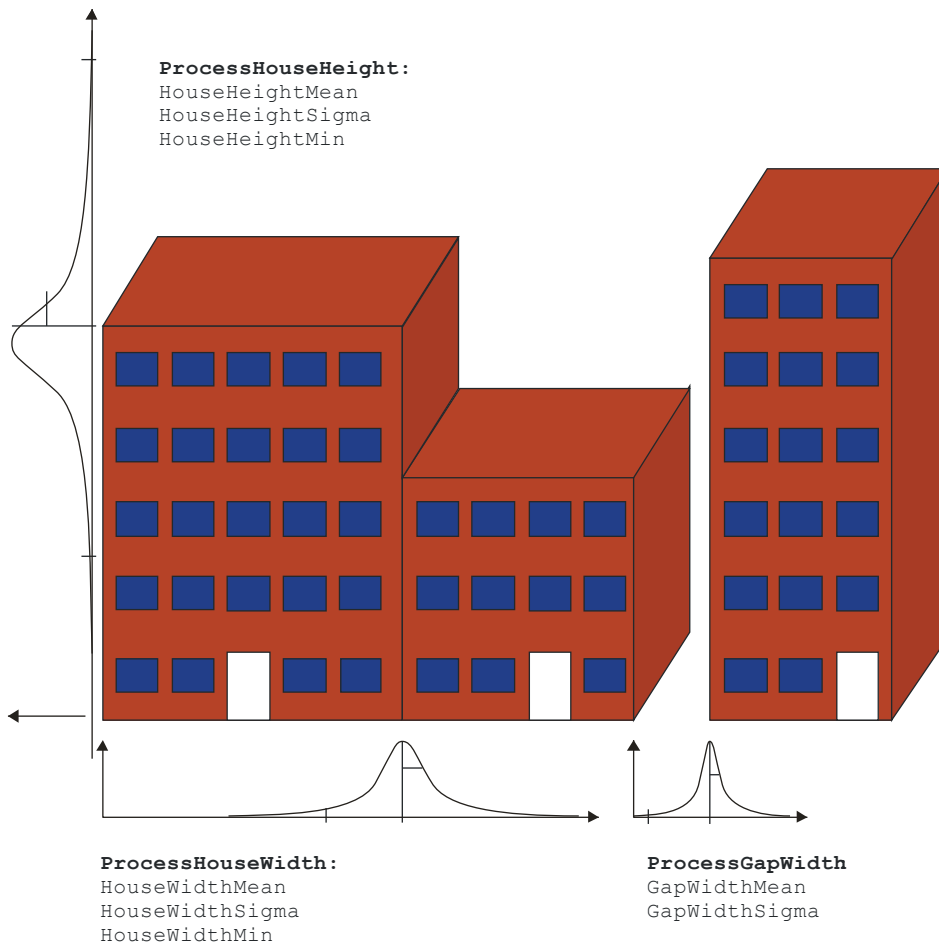
Report P. 2145-74

4.3.3 Tree parameters

Unlike the buildings, all trees in the scenario have the same deterministic shape. There are two rows of trees that can be switched on. The placement of both tree rows is controlled by separate statistical placement processes for each row, respectively.

Urban car environment

TreeHeight	m	8
TreeDiameter	m	5
TreeTrunkLength	m	2
TreeTrunkDiameter	m	0.2
TreeAttenuation	dB/m	1.1
TreeRow1YPosition	m	−8
TreeRow2YPosition	m	8
TreeRow1YSigma	m	2
TreeRow2YSigma	m	2
TreeRow1MeanDistance	m	60
TreeRow2MeanDistance	m	40
TreeRow1DistanceSigma	m	20
TreeRow2DistanceSigma	m	20

Suburban car environment

TreeHeight	m	7
TreeDiameter	m	4
TreeTrunkLength	m	2
TreeTrunkDiameter	m	0.2
TreeAttenuation	dB/m	1.1
TreeRow1YPosition	m	−5
TreeRow2YPosition	m	5
TreeRow1YSigma	m	0.5
TreeRow2YSigma	m	0.5
TreeRow1MeanDistance	m	40
TreeRow2MeanDistance	m	20
TreeRow1DistanceSigma	m	20
TreeRow2DistanceSigma	m	20

Urban pedestrian environment

TreeHeight	m	6
TreeDiameter	m	3
TreeTrunkLength	m	2
TreeTrunkDiameter	m	0.2
TreeAttenuation	dB/m	1.1
TreeRow1YPosition	m	−6
TreeRow2YPosition	m	6
TreeRow1YSigma	m	0.5
TreeRow2YSigma	m	0.5
TreeRow1MeanDistance	m	60
TreeRow2MeanDistance	m	40
TreeRow1DistanceSigma	m	20
TreeRow2DistanceSigma	m	20

Suburban pedestrian environment

TreeHeight	m	7
TreeDiameter	m	4
TreeTrunkLength	m	2
TreeTrunkDiameter	m	0.2
TreeAttenuation	dB/m	1.1
TreeRow1YPosition	m	−5
TreeRow2YPosition	m	5
TreeRow1YSigma	m	0.5
TreeRow2YSigma	m	0.5
TreeRow1MeanDistance	m	40
TreeRow2MeanDistance	m	20
TreeRow1DistanceSigma	m	20
TreeRow2DistanceSigma	m	20

FIGURE 75

Tree parameters
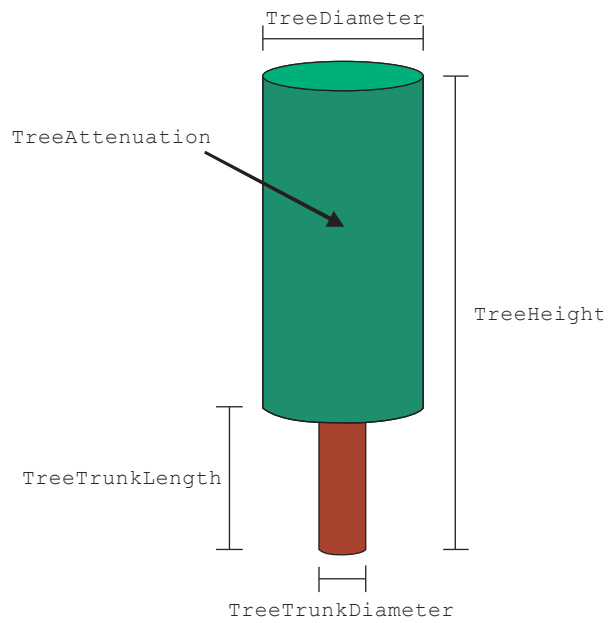
Report P. 2145-75

FIGURE 76

Tree placement processes
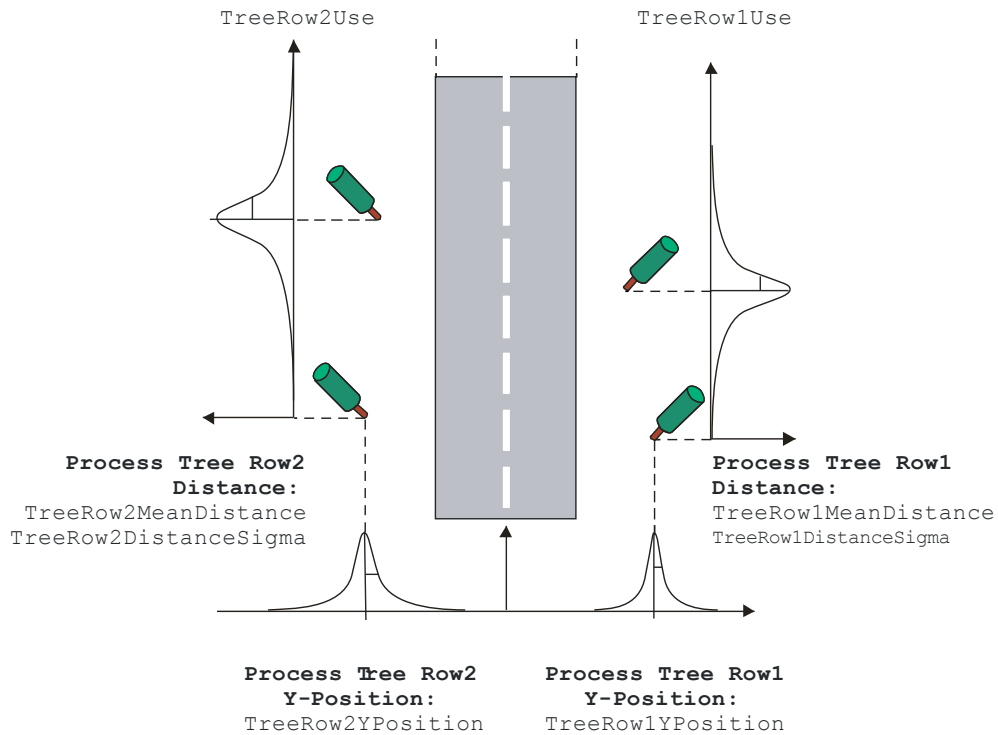
Report P. 2145-76

4.3.4 Pole parameters

The handling of poles in the environment is similar to that for trees. The shape is the same for all poles, and there are two rows that can be switched on. The pole placement is likewise controlled by separate statistical placement processes.

Urban car environment

PoleRow1 use		Yes
Pole Row2 use		no
PoleHeight	m	10
PoleDiameter	m	0.2
PoleRow1YPosition	m	0
PoleRow2YPosition	m	10
PoleRow1YSigma	m	1
PoleRow2YSigma	m	1
PoleRow1MeanDistance	m	25
PoleRow2MeanDistance	m	10
PoleRow1DistanceSigma	m	10
PoleRow2DistanceSigma	m	10

Suburban car environment

PoleRow1 use		Yes
Pole Row2 use		no
PoleHeight	m	9
PoleDiameter	m	0.2
PoleRow1YPosition	m	0
PoleRow2YPosition	m	−5
PoleRow1YSigma	m	0.5
PoleRow2YSigma	m	0.5
PoleRow1MeanDistance	m	40
PoleRow2MeanDistance	m	40
PoleRow1DistanceSigma	m	5
PoleRow2DistanceSigma	m	5

Urban pedestrian environment

PoleRow1 use		Yes
Pole Row2 use		no
PoleHeight	m	10
PoleDiameter	m	0.2
PoleRow1YPosition	m	−6
PoleRow2YPosition	m	0
PoleRow1YSigma	m	0.5
PoleRow2YSigma	m	0.5
PoleRow1MeanDistance	m	25
PoleRow2MeanDistance	m	10
PoleRow1DistanceSigma	m	10
PoleRow2DistanceSigma	m	10

Suburban pedestrian environment

PoleRow1 use		Yes
Pole Row2 use		no
PoleHeight	m	9
PoleDiameter	m	0.2
PoleRow1YPosition	m	0
PoleRow2YPosition	m	−5
PoleRow1YSigma	m	0.5
PoleRow2YSigma	m	0.5
PoleRow1MeanDistance	m	40
PoleRow2MeanDistance	m	40
PoleRow1DistanceSigma	m	5
PoleRow2DistanceSigma	m	5

FIGURE 77

Pole parameters
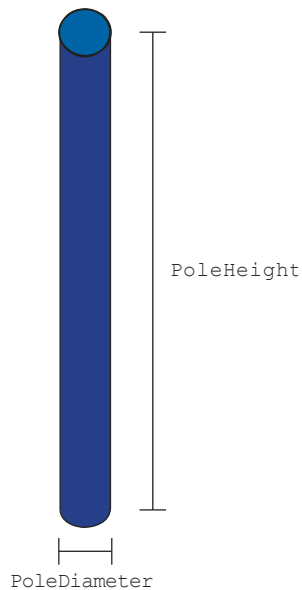
Report P. 2145-77

FIGURE 78

Pole placement processes
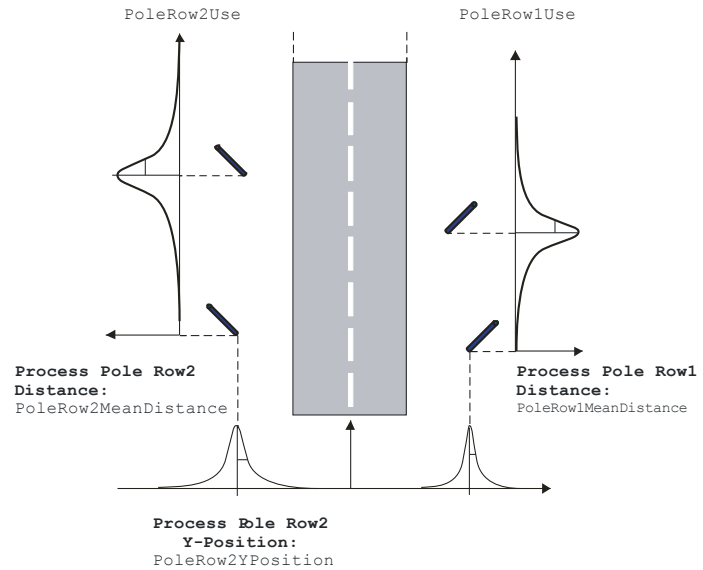
Report P. 2145-78

5 Data file interface descriptions

This section contains information related to the software implementation of the LMSCM. It provides a description of the interface implemented in the software. The intention of this section is to allow a user of the software to use other statistical data than the one delivered with this implementation.

5.1 Statistical data file description

With the channel model implementation, two Matlab files which contain statistical channel data, are provided for different environments (urban, suburban) and different applications (car, pedestrian).

As example for car applications in an urban environment the statistical data files are named `EchoNumberParUrbanCar.mat` and `EchoParUrbanCar.mat`.

These two data files contain the following lists of Matlab variables:

```
EchoNumberParUrbanCar.mat
Name                        Size            Bytes   Class

ANraysCumSpecFreqBins       32x9             2304   double
ANraysCumSpecVal            32x9             2304   double
ANraysMean                  1x9                72   double
ElevationVec                1x9                72   double

EchoParUrbanCar.mat
Name                        Size            Bytes   Class

ABandwidthMean              1x9                72   double
ABandwidthSigma             1x9                72   double
ADeltaAzim                  10x9              720   double
```

```
ALengthCdfBins            24x9                1728  double
ALengthCdfValues          24x9                1728  double
AMeanPower                10x10x9             7200  double
AMeanPowerSigma           10x10x9             7200  double
APosition                 10x10x9             7200  double
ARfxMovProb               1x9                   72  double
ARiceCdfBins              27x9                1944  double
ARiceCdfValues            27x9                1944  double
ElevationVec              1x9                   72  double
```

5.1.1 Elevation vector

Different statistical channel parameters are stored in these variables. The last dimension of each variable is related to the satellite elevation, which is the angle between the tangential plane of the earth's surface at the user position and the incidence angle of the direct path signal from the satellite. Basis for the statistics are channel measurements at nine different elevations. These values are stored in the variable `ElevationVec` (degrees):

```
ElevationVec =

     5    10    20    30    40    50    60    70    80
```

5.1.2 Number of coexisting echoes

In the measurements a narrow and a wide band process were identified causing variations in the number of coexisting echoes as the receiver moves through the multipath environment. To model the receiver position dependent variations in the number of coexisting echoes $N_e(x)$, where x is the receiver's position along its trajectory, both processes are synthesized in the implemented channel model.

The discrete common CDF (Cumulative Distribution Function) of the narrow and wide band process is approximated by a piecewise linear function $P(X)$, which is stored in the variables `ANraysCumSpecVal` and `ANraysCumSpecFreqBins` for the nine different elevations.

As an example the values of the CDF with unit [1] for 5° elevation are:

```
ANraysCumSpecVal(:,1)' =

  1.0e+006 *

0       0.4294      0.4897      0.4970      0.5587      0.6614      0.7495
0.7734        0.7771      0.7795      0.7891      0.7911      0.7978
0.8025     0.8041    0.8138    0.8294            0.8440         0.8696
0.8841     0.9148    0.9805    1.0429    1.0813    1.1017
1.1160        1.1258      1.1431      1.1505      1.1555      1.1600
1.1627
```

at the corresponding spatial frequencies with unit [1/m] stored in:
```
ANraysCumSpecFreqBins(:,1)' =

0       0.0005      0.0010      0.0015      0.0020      0.0025      0.0030
0.0035        0.0040      0.0045      0.0055      0.0065      0.0075
0.0085        0.0095      0.0120      0.0145      0.0195      0.0345
0.0495        0.0995      0.2495      0.4995      0.7495      0.9995
```

```
1.2495      1.4995      2.4995      3.4995      4.9995      7.4995
9.9995
```

In the channel model the spectrum of the process is derived from the CDF $P(X)$ by differentiation. Next an inverse Fourier transform is calculated resulting in the synthesized change of the number of coexisting echoes $N_p(x)$. The total number of coexisting echoes is calculated by adding the average number of echoes $\bar{n}$ with a lower bound of zero:

$$N_e(x) = \max(0, N_p(x) + \bar{n})$$

The average number of coexisting echoes $\bar{n}$ is stored in the variable `ANraysMean`. As example, the values for the different elevations in the urban environment for car applications are:

```
ANraysMean =

 8.7311     13.0396   13.2762   18.3764   23.4766   24.6038   25.7309
26.8581     27.9853
```

5.2   Echo bandwidth

In the implemented model the distribution of the echoes' bandwidth is modelled by a Gaussian process. The corresponding mean and variance values in Hz are stored in the variables `ABandwidthMean` and `ABandwidthSigma` for the different elevations. Again for the urban car example these values are:

```
ABandwidthMean =
4.6770      4.6874      4.6990      4.7520      4.8049      4.7791
4.7533      4.7275    4.7017
```

and

```
ABandwidthSigma =

2.0850      2.0817      2.0652      2.0271      1.9889      1.9829
1.9769      1.9709    1.9649
```

5.3   Life span of reflectors

In the measurement data the channel appears rapidly changing. Many echoes disappear and new ones appear. This process is highly correlated to the receiver speed. When the receiver stops, the echoes remain. In order to allow the motion dependent modelling of the multipath channel, the echo life span in meters is defined. This life span is the distance the receiver is travelling from appearance of an echo until it disappears.

The discrete distribution of the life span of reflectors, respectively its CDF, is stored in the variables `ALengthCdfBins` and `ALengthCdfValues`, where for example:

```
ALengthCdfValues(:,1)' =
0       0.2776      0.4758      0.6044      0.6934      0.7568      0.8030
0.8373      0.8637      0.8844      0.9144      0.9348      0.9492
0.9598      0.9675      0.9798      0.9866      0.9934      0.9963
0.9977    0.9990    0.9994    0.9999    1.0000
```

are the values at the lowest elevation of 5° at the corresponding life spans (m):

```
ALengthCdfBins(:,1)' =
0.1000      0.2000      0.3000      0.4000      0.5000      0.6000
0.7000      0.8000      0.9000      1.0000      1.2000      1.4000
1.6000      1.8000      2.0000      2.5000      3.0000      4.0000
5.0000      6.0000      8.0000     10.0000     15.0000     20.0000
```

5.4 Rice factor of echoes

The fading characteristic of single echo signals observed in the measured data indicates a constant component. Therefore a Ricean model is applied. The discrete distribution of the Rice factors of echo signals, respectively its CDF, is stored in the variables `ARiceCdfBins` and `ARiceCdfValues`, where for example:

```
ARiceCdfValues(:,1)' =

0       0.0058      0.0138      0.0220      0.0313      0.0422      0.0542
0.0672      0.0810      0.0955      0.1255      0.1561      0.1864
0.2161      0.2448      0.3109      0.3686      0.4645      0.5412
0.6027      0.6937      0.7579      0.8538      0.9042      0.9553
0.9799      1.0000
```

are the values at the lowest elevation of 5° at the corresponding Rice factor bins

```
ARiceCdfBins(:,1)' =

0.1000      0.2000      0.3000      0.4000      0.5000      0.6000
0.7000      0.8000      0.9000      1.0000      1.2000      1.4000
1.6000      1.8000      2.0000      2.5000      3.0000      4.0000
5.0000      6.0000      8.0000     10.0000     15.0000     20.0000
30.0000     40.0000     60.0000
```

5.5 Movement of reflection points

The measurements also revealed that some reflection points move according to the movement of the receiver (like e.g. on a house wall), while others remain at fixed positions. A measure for this behaviour is the observed change in the angle α, which is the angle between the van's moving direction and the direction to the reflection point. For a theoretically fixed reflection α would change according to the movement of the receiver. On the other hand, if the reflection point moves e.g. along a house front, α does not change during the observation interval. The distribution of this angular changes shows a significant bend, which allows to estimate the percentage of reflection points which are moving. The rest can be associated with fixed reflectors, e.g., traffic signs or trees, which in general have very short life spans.

The probabilities for a moving reflection point at different elevations are stored in:

```
ARfxMovProb =

0.0209      0.0387      0.0559      0.1386      0.1471      0.1536
0.1600      0.1665      0.1730
```

5.6 Horizontal reflector position distribution

Further analysis of the measurement data show that the horizontal position distribution of reflectors relative to the receiver position changes significantly for different elevations. These two-dimensional distributions are symmetrical with respect to the movement direction of the receiver, because in urban and suburban environments the likelihood for a reflector to be on the left or the right side of a street is the same. Moreover, the likelihood for a reflector in front or in the rear is the same, thus the distributions are symmetrical with respect to the cross axis, too. Hence, only a quarter of the distributions needs to be stored.

The two-step polynomial approximations of these horizontal reflector position distributions are stored in the variable APosition.

As an example the polynomial coefficients for 5° elevation in the urban car case are:

```
APosition(:,:,1) =

  Columns 1 through 4

 -4.2762e-038   8.4117e-035  -6.9855e-032   3.1800e-029
  1.9300e-035  -3.7787e-032   3.1218e-029  -1.4130e-026
 -3.6100e-033   7.0363e-030  -5.7842e-027   2.6030e-024
  3.6015e-031  -6.9922e-028   5.7219e-025  -2.5610e-022
 -2.0482e-029   3.9650e-026  -3.2331e-023   1.4405e-020
  6.5416e-028  -1.2655e-024   1.0305e-021  -4.5796e-019
 -1.0705e-026   2.0804e-023  -1.7004e-020   7.5746e-018
  7.3129e-026  -1.4463e-022   1.2015e-019  -5.4257e-017
 -6.1199e-026   1.3699e-022  -1.2466e-019   5.9536e-017
  4.5639e-025  -9.4822e-022   8.3410e-019  -4.0362e-016

  Columns 5 through 8

 -8.6107e-027   1.4025e-024  -1.3089e-022   5.9626e-021
  3.8008e-024  -6.1448e-022   5.6899e-020  -2.5789e-018
 -6.9548e-022   1.1153e-019  -1.0229e-017   4.5915e-016
  6.7969e-020  -1.0807e-017   9.7998e-016  -4.3308e-014
 -3.7995e-018   5.9880e-016  -5.3581e-014   2.3133e-012
  1.2024e-016  -1.8796e-014   1.6558e-012  -6.9005e-011
 -1.9881e-015   3.0896e-013  -2.6721e-011   1.0509e-009
  1.4368e-014  -2.2300e-012   1.8771e-010  -6.5134e-009
 -1.5862e-014   2.2390e-012  -1.1857e-010  -5.9136e-009
  1.1683e-013  -2.0590e-011   2.1473e-009  -1.2071e-007


  Columns 9 through 10

 -6.7635e-020  -8.6843e-019
  3.0199e-017   3.4464e-016
 -5.3951e-015  -5.9065e-014
  4.9353e-013   5.7003e-012
 -2.4271e-011  -3.3547e-010
  5.9928e-010   1.2058e-008
 -5.2603e-009  -2.5004e-007
 -3.0846e-008   2.7240e-006
```

```
   7.7678e-007 -1.2097e-005
   2.6144e-006  3.7349e-005
```

In the model a quarter of the horizontal reflector position distribution in polar coordinates is calculated from these coefficients by:

```
for
r = 1:length(RadiusVec)
p = diag(APosition(:,:,k)*repmat([RadiusVec(r).^[9:-1:0]],11,1)');
y = polyval(p(1:10),AzimuthVec,9);
A(:,r) = y';                      % Quarter of position distribution
end
```

where *k* is the index of the elevation and:

```
RadiusVec = [0:2:250];       % Model radius grid in m
AzimuthVec = [0:2:90];       % Model azimuth grid in degrees
```

5.7   The relative satellite-reflector azimuth angle

The above described horizontal reflector position distributions are independent of the satellite azimuth. In order to model the multipath channel dependent on both satellite elevation and azimuth, statistics for the azimuthal angle of arrival of echoes relative to the LoS signal are used. As the measurements revealed these distributions are symmetrical for positive and negative angles.

Polynomial approximations of these statistics between 0-180° (because of the symmetry) are stored in the variable `ADeltaAzim` for the different elevation angles. As example for 5° elevation in the urban car case the polynomial coefficients are:

```
ADeltaAzim(:,1)' =

-6.6625e-020    5.8308e-017  -2.1039e-014    4.0321e-012  -4.4015e-
010       2.7190e-008  -8.8648e-007    1.3628e-005  -6.6625e-005
9.9306e-004
```

In the model the relative satellite-reflector azimuth angle distribution is calculated from these coefficients by:

```
A = polyval(ADeltaAzim(:,k),DeltaAzimuthVec,9);
Afull = [A,A(end-1:-1:1)];   % Full delta azimuth distribution
```

where *k* is the index of the elevation and:

```
DeltaAzimuthVec = [0:2:180]; % Model delta azimuth grid in degrees
```

5.8 Average power of echo signals

The distance and direction of a reflector from the receiver plays a major role for the power of the received echo signal. This fact is taken into account in the LMS channel model. From the measurement data statistics for the mean and for the standard deviation of the average echo power depending on the relative horizontal reflector position were determined. Again these two-dimensional distributions are symmetrical with respect to the movement direction of the receiver and with respect to the cross axis. Hence, only a quarter of the distributions needs to be stored.

The two step polynomial approximations of mean and variance of these echo power distributions are stored in the variables AMeanPower and AMeanPowerSigma, respectively. The mean and variance values of these distributions are giving the echo powers in dB relative to an unobstructed direct path signal.

```
AMeanPower(:,:,1) =

  Columns 1 through 4

   3.2415e-033  -4.4259e-030   2.0915e-027  -2.4915e-025
  -1.4516e-030   2.0161e-027  -9.8989e-025   1.4582e-022
   2.6687e-028  -3.7401e-025   1.8708e-022  -2.9970e-020
  -2.5852e-026   3.6192e-023  -1.8021e-020   2.8107e-018
   1.3999e-024  -1.9254e-021   9.1711e-019  -1.1130e-016
  -4.0648e-023   5.2756e-020  -2.1378e-017  -3.5833e-016
   4.9848e-022  -4.9793e-019   1.5104e-017   1.7251e-013
   1.2194e-021  -6.0663e-018   8.0632e-015  -5.0351e-012
  -6.4724e-020   1.2835e-016  -1.0736e-013   4.9239e-011
   1.1131e-019  -1.7655e-016   1.1110e-013  -3.4615e-011

  Columns 5 through 8

  -1.1925e-022   5.0124e-020  -7.8214e-018   5.5650e-016
   4.1637e-020  -2.0094e-017   3.2257e-015  -2.3139e-013
  -6.5995e-018   3.4849e-015  -5.6760e-013   4.0781e-011
   6.7858e-016  -3.4584e-013   5.5772e-011  -3.9715e-009
  -5.1674e-014   2.1765e-011  -3.3575e-009   2.3344e-007
   2.7945e-012  -8.9493e-010   1.2720e-007  -8.4755e-006
  -9.4727e-011   2.3281e-008  -2.9617e-006   1.8540e-004
   1.7310e-009  -3.4324e-007   3.8525e-005  -2.2248e-003
  -1.3471e-008   2.2365e-006  -2.1816e-004   1.1296e-002
   5.2379e-009  -2.3587e-007  -2.8721e-005   3.6428e-003

  Columns 9 through 10

  -1.4925e-014   1.0488e-013
   6.1936e-012  -4.3351e-011
  -1.0852e-009   7.5583e-009
   1.0450e-007  -7.2361e-007
  -6.0306e-006   4.1483e-005
   2.1307e-004  -1.4548e-003
  -4.4920e-003   3.0403e-002
   5.1368e-002  -3.4283e-001
  -2.4106e-001   1.5657e+000
  -1.4033e-001  -3.0032e+001
```

```
AMeanPowerSigma(:,:,1) =

  Columns 1 through 4

 -6.7162e-036 -1.3427e-031  2.5678e-028 -1.9790e-025
  2.8474e-032  8.2478e-030 -6.9534e-026  6.6278e-023
 -1.0421e-029  8.8194e-027  3.9699e-024 -7.9929e-021
  1.6298e-027 -2.0585e-024  6.0874e-022  3.2146e-019
 -1.3599e-025  2.0158e-022 -1.0457e-019  1.3616e-017
  6.4285e-024 -1.0401e-020  6.5078e-018 -1.8134e-015
 -1.7047e-022  2.9095e-019 -1.9957e-016  6.8149e-014
  2.3556e-021 -4.1320e-018  2.9566e-015 -1.0897e-012
 -1.4295e-020  2.4816e-017 -1.7517e-014  6.3391e-012
  5.5300e-020 -9.8571e-017  7.2827e-014 -2.8728e-011

  Columns 5 through 8

  8.1771e-023 -1.9705e-020  2.8014e-018 -2.2505e-016
 -2.9883e-020  7.5472e-018 -1.1046e-015  9.0513e-014
  4.2796e-018 -1.1681e-015  1.7878e-013 -1.5090e-011
 -2.9039e-016  9.2293e-014 -1.5227e-011  1.3459e-009
  7.8105e-015 -3.8059e-012  7.2537e-010 -6.9179e-008
  1.0264e-013  6.8814e-011 -1.8867e-008  2.0593e-006
 -1.0763e-011  5.6750e-011  2.4039e-007 -3.4208e-005
  2.0843e-010 -1.4956e-008 -1.3074e-006  3.0631e-004
 -1.1794e-009  7.9272e-008  7.7429e-006 -1.6358e-003
  6.4736e-009 -8.1970e-007  5.1574e-005 -8.2620e-004

  Columns 9 through 10

  8.9018e-015 -9.8528e-014
 -3.6356e-012  4.1189e-011
  6.1957e-010 -7.2226e-009
 -5.7064e-008  6.8914e-007
  3.0750e-006 -3.8804e-005
 -9.8162e-005  1.3070e-003
  1.7996e-003 -2.5461e-002

 -1.7782e-002  2.6351e-001
  8.7924e-002 -1.2001e+000
 -6.2491e-002  3.3190e+000
```

In the model a quarter of the mean and variance echo power distribution in polar coordinates is calculated from these coefficients by:

```
for
r = 1:length(RadiusVec)
p = diag(AMeanPower(:,:,k)*repmat([RadiusVec(r).^[9:-1:0]],11,1)');
y = polyval(p(1:10),AzimuthVec,9);
Pm(:,r) = y';              % Quarter of power distribution mean
```

```
p       =       diag(AMeanPowerSigma(:,:,k)*repmat([RadiusVec(r).^[9:-
1:0]],11,1)')');
y = polyval(p(1:10),AzimuthVec,9);
Ps(:,r) = y';              % Quarter of power distribution sigma
End
```

where *k* is the index of the elevation and:

```
RadiusVec = [0:2:250];    % Model radius grid in m
AzimuthVec = [0:2:90];    % Model azimuth grid in degrees
```

6   User motion

This channel model is designed to provide the user with a time variant speed, time variant heading and satellite elevation. In simulations, the selection of the user motion has a significant influence on the performance of the device under test (DUT).

For example, in a simulation using a slow motion user profile, echoes exist over long time intervals. A navigation receiver that estimates the channel impulse response and is designed to use the coherence length of the channel for improved accuracy can benefit from the long coherence length. A standard delay-locked loop (DLL) receiver will result in large errors. If a high speed motion profile is used, the echoes become extremely short and the estimation receiver can no longer estimate the channel properly which will result in larger errors where a standard DLL will average over a certain time period and eliminate most of the error. This example shows that this influence can be very large and can even change the performance order of satellite receivers. Therefore, the user motion profile has to be selected with care. Two distinct cases are described in the subsections below.

The user motion indicated in this section does not incorporate antenna patterns and variations due to antenna gain due to user dynamics (for example, a pedestrian user with a mobile terminal tends to change randomly the direction of the antenna boresight).

6.1   Case 1: Specific case simulation

In this case, the intention is to simulate the performance of a specific receiver on a specific route through a specific city (real or hypothetical) with a given set of values (e.g. measured speed, azimuth and satellite elevation). The result of this simulation will be accurate but only valid for this case. This is useful if the simulation is, for example, iterated in different runs over a range of azimuths (e.g. 0, 10, 20, 30 …. 350°). Then the result of the simulations can be compared for the different azimuths and will show which azimuth is the best and which is the worst case.

Another example is the iteration of the user speed for a given track: in this case the speed of the different simulation runs is varied (e.g. 10 km/h, 20 km/h …. 80 km/h). The result of the simulation runs will show the influence of the speed to the navigation error.

In addition, the model can be fed with measured speed, heading and elevation data. In this case, the simulation will give the exact result for a user driving on this road. An extrapolation to other tracks is not possible.

For all applications where a user motion profile can be generated *a priori* it is suggested to use such a generated profile.

6.2 Case 2: Statistical simulations (Monte Carlo simulation)

Often the goal is not to vary the user movements but parameters that are not motion dependent such as receivers, satellite signals, satellite power, etc. In these cases, it is advisable to reduce the dependence on geometric parameters as much as possible.

To simulate the dependence of the system on a single parameter, it is necessary to reduce the dependence of the simulation on all other parameters as much as possible. Therefore, it is advisable to use the following a set of parameters which will allow for comparing results from different research organizations:

FIGURE 79

Full circle track illustrated
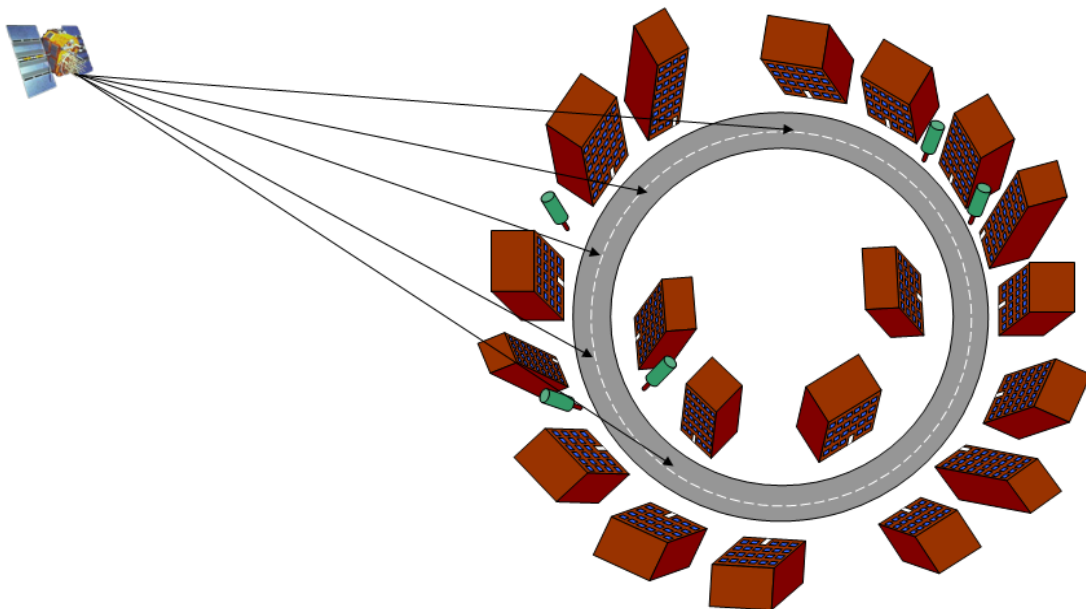
6.2.1 Car Profile – Car A

For convenience this profile is called "ITU P.2145 – Car A"

a)   User direction and satellite azimuth

The simulation result strongly depends on the relative angle between the direction of the vehicle and the satellite azimuth. For example, if the satellite is located at a relative azimuth along the direction of movement, the channel will be in line-of-sight conditions most of the time. However, if the satellite is located in a relative azimuth perpendicular to the direction of movement, the signal is often shadowed (especially for low elevations). Therefore a selection of a route where the satellite is more often in the front would result in a higher accuracy than if the satellite is at the side. If the heading is chosen randomly during a simulation (e.g. by a random walk) this can happen accidentally between two simulation runs and may give misleading results.

Therefore, it is suggested to use a large circular road so that it covers all user directions evenly. A period of 1800 s to cover a 360° change in direction is an adequate choice. For longer simulation times, a multiple of full circles ($N = 1,2,3$ ...) shall be considered. This results in a simulation time of $N \times 1800$ s.

b)   *Satellite elevation*

It is suggested to keep the elevation of the satellite constant over the full circle to avoid a mixed dependence on elevation and azimuth.

c)   *User speed*

A time cycle of 60 s over which the user speed changes is suggested, including high-speed movements, stop phases and low speed movements. This profile simulates a stop and go situation in urban traffic. This profile is shown in Fig. 80.

FIGURE 80

Speed profile for car applications – Profile "ITU P.2145 – Car A"
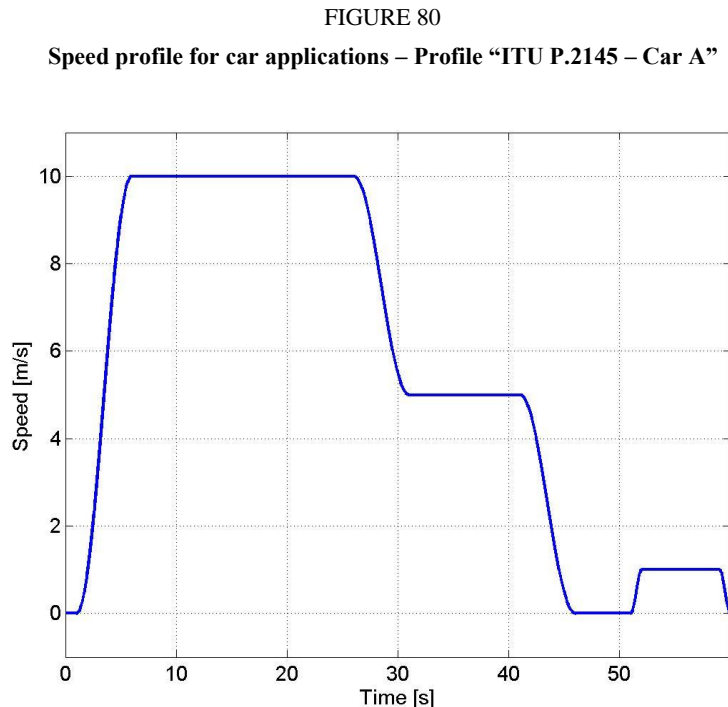
d)   *Receiver height*

For the car application, it is suggested to use a constant antenna height of 1.5 m.

6.2.2   Pedestrian profile – "Pedestrian A"

For this application, a profile that represents a stop and walk cycle is suggested. In contrast to a car application, it is assumed that the user walks only at one speed.

For convenience this profile is called "ITU P.2145 – Pedestrian A"

e)   *User direction and satellite azimuth*

As in the case of the car profile "Car A", the simulation result strongly depends on the relative angle between the direction of the pedestrian and the satellite relative azimuth. Once again, a large circular road is advised.

f)   *Satellite elevation*

To avoid a mixed dependence on elevation and azimuth, it is suggested to keep the elevation of the satellite constant over the full circle.

g)   *User speed*

A time cycle of 60 s over which the user speed changes is suggested. This profile is presented in Fig. 81.

FIGURE 81

Speed profile for pedestrian applications – Profile "ITU P.2145 – Pedestrian A"
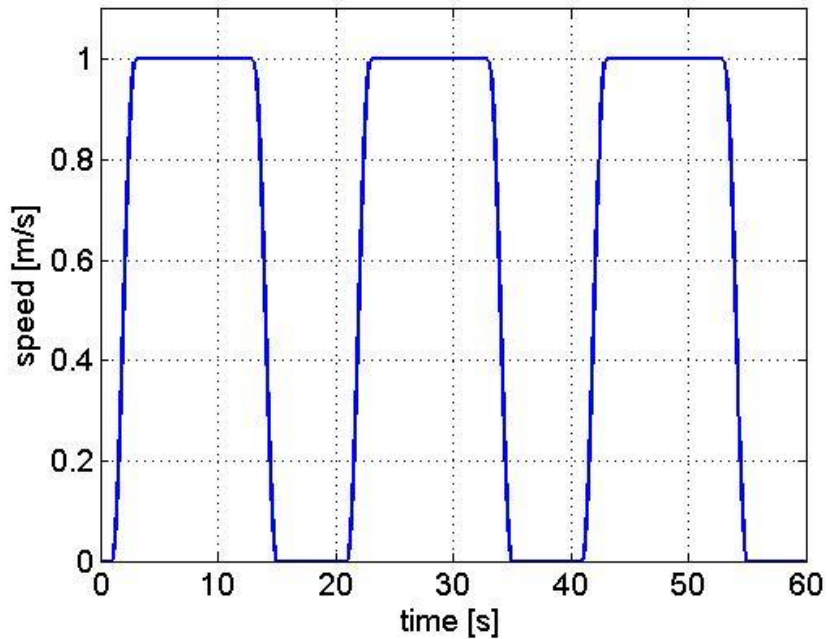
h) *Receiver height*

In a pedestrian application, the device is often a handheld. While walking, this height can vary due to the movement of the user's hand. To simulate a time variant antenna height a profile like the one presented in Fig. 82 is advised.

FIGURE 82

Antenna height for pedestrian applications – Profile "ITU P.2145 – Pedestrian A"
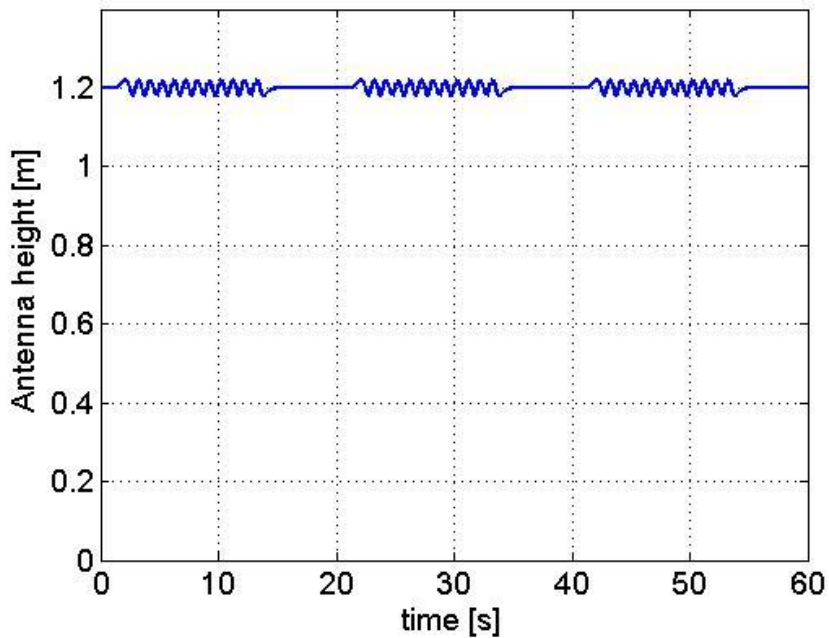
7   Acronyms

CDF   Cumulative distribution function

CIR   Channel impulse response

FIR   Finite impulse response

IDFT   Inverse discrete Fourier transform

LMSCM   Land mobile satellite channel model

LoS   Line of sight

8   IPR protection

Some methods of this channel model are protected by filed or granted patents. The German Aerospace Center has signed the patent statement and licensing form of the ITU to allow unlimited and non-discriminatory access to licenses concerning these patents.

9   References

[1]   KAMMEYER, K.D. and KROSCHEL, K. (2002) *Digitale Signalverarbeitung*. B. G. Teubner Verlag.

[2]   LEHNER, A. (2007), Multipath Channel Modelling for Satellite Navigation Systems PhD Thesis, University of Erlangen-Nuremberg, ISBN 978-3-8322-6651-6, Shaker Verlag GmbH, D-52018 Aachen, Germany.

[3]   SKLAR, B. (1998) *Digital Communications*. Prentice Hall.

Part B: Model parameters for the physical-statistical wideband satellite-to-indoor channel model in Recommendation ITU-R P.681

1   Satellite-to-indoor channel propagation model

Within this section, the satellite-to-indoor channel model described in Recommendation ITU-R P.681 that allows simulating a moving receiver located inside a building will be depicted in more detail. The channel model includes components calculated by physical-deterministic and stochastic methods. To apply physical-deterministic or site-specific methods, the layout of the environment is required. As a complete building layout including its interior is cumbersome to be used within simulations, the proposed satellite-to-indoor channel model uses physical-deterministic methods only for the room in which the receiver is located. Furthermore, the model is restricted to rooms that have window fronts or walls directed toward the transmitter. The layout of the room will be denoted as scenery in the following and defines the space R. Other channel contributions from outside the room or interior objects, like furniture, are treated in a stochastic manner.

The stochastic part of the channel model is based on statistics that have been extracted from a satellite-to-indoor channel sounder wideband measurement campaign performed at a premise of the German Aerospace Center (DLR) at Oberpfaffenhofen close to Munich. For the measurement campaign, a right hand circular polarized signal at L-band, in more detailed at 1.51 GHz with a bandwidth of 100 MHz, has been used in a typical office environment. More details on the measurement campaign itself and on the extraction of the statistics can be found in [5], [7]. Due to the frequency allocation of

current satellites' signals and the limits of the measurement campaign, the satellite-to-indoor channel model supports L-band frequencies, i.e. between 1-2 GHz. The model describes the multipath propagation situation for transmissions between a single satellite and a receiver. A satellite constellation, i.e. multiple satellites at different positions, could be simulated sequentially. By using the same environmental layout, the components based on site specific physical-deterministic calculations are correlated between different simulations. Still, due to stochastic components two simulations with the same transmitter and receiver positions will not provide exactly the same CIR. Please note that corresponding publications, i.e. background information can be found in [5], [6] and [9]. The scope and applicability of the model is detailed in Recommendation ITU-R P.681.

In the following section, the usage of the satellite-to-indoor channel model simulator supplied with Recommendation ITU-R P.681 is described. Thereafter, a detailed description of the satellite-to-indoor channel model is provided including comparison to measurement data and software validation.

1.1 Usage of the channel model simulator

Within this section, a more details on the usage of the satellite-to-indoor channel model simulator software are provided including code fragments illustrating the usage.

1.1.1 Input parameters

The channel model is split into an initialization phase and a runtime phase. In order to run the channel model, several parameters need to be provided as input as described in Recommendation ITU-R P.681. These include the carrier frequency, signal bandwidth, spatially averaged delay spread, transmitter position, scenery and optionally the number of scattered components.

An exemplary setup for the parameters could be:

```
par.bandwidth = 100e6;   % bandwidth used in [Hz]
par.del_spread = 30e-9;  % delay spread in [s]
par.freq = 1.5e9;  % carrier frequency in [Hz]
elev = 10;   % elevation angle in [deg] for the transmitter
azi = 0;     % azimuth angle in [deg] for the transmitter
par.trans_pos = 20e6*[cosd(azi)*cosd(elev); cosd(elev)*sind(azi);...
                sind(elev)]; % transmitter positions in a distance of 20e6 [m]
```

To create the room structure based on the function `createRoom()`:

```
par.room.dx = 10;   % x-dimension [m]
par.room.dy = 10;   % y-dimension [m]
par.room.dz = 3;    % z-dimension [m] (height)
par.room.winWidth = 1;  % window width [m]
par.room.winUpper = 0.3; % distance to upper edge for the windows [m]
par.room.winLower = 1.2; % distance to lower edge for the windows [m]
par.room.winNums = 5;   % number of windows
par.room.winWall = 1;   % wall number where the windows are placed
par.room.roofWall = 5;  % wall with the transmission coefficient par.room.Troof
par.room.Twin = 10^(-2/20);   % transmission factor for windows [linear]
par.room.Twall = 10^(-15/20); % transmission factor for walls [linear]
par.room.Troof = 10^(-25/20); % transmission factor for roof [linear]
walls = createRoom(par.room);
```

where Fig. 1 visualizes the created scenery. Using the function, the walls are automatically defined in the coordinate system.

FIGURE 1

Visualization of the scenery generated using `createRoom()`
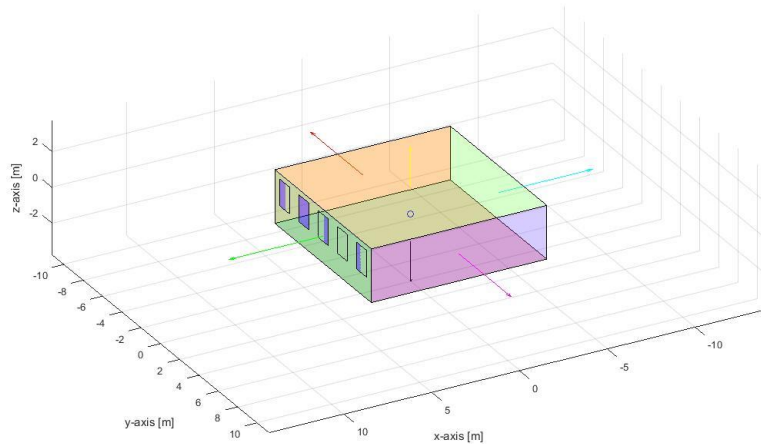
In order to use the wideband satellite-to-indoor channel model, propagation related parameters are required by the user. These are the perpendicular transmission coefficients for the materials within the description of the scenery and the delay spread value. Values for the perpendicular transmission coefficients of building materials can be found in [14] for a large variety of building materials and frequencies. Additionally, Recommendation ITU-R P.2040 provides values for the relative permittivity and conductivity of several building materials such that the perpendicular transmission coefficient can be calculated by formulas in Recommendation ITU-R P.2040. For the delay spread value, a formula and values can be found in Recommendation ITU-R P.1238. Furthermore, measured delay spread values at S-band carrier frequency for several building types may be found in [11].

1.1.2   Running the model and output parameters

In order to run the model, the structures `par` and `walls` need to be passed to the function `sim_chan()`:

```
obj = sim_chan(par,walls);  % initialise the model
```

which initializes the channel model.
In order to simulate the channel with arbitrary receiver trajectory, a loop over different receiver positions need to be used:

```
for i = 1:size(rec,2)    % go through for each receiver position
 [cir,p]= sim_chan(obj,rec(:,i));  % get channel output for RX position rec(:,i)
end;
```

where the vector `rec(:,i)` defines a three dimensional point x_r in space in meters. Please note that it is expected that the receiver trajectory is provided by the user of the model in terms of single receiver positions that are changing within the loop.

The model provides the channel impulse response (CIR) $h(\tau, x_r)$ calculated in dependency of the receiver position x_r provided to the user as:

$$h(\tau, x_r) = \sum_{l=0}^{L(x_r)-1} \tilde{\alpha}_l(x_r)\delta(\tau - \tilde{\tau}_l(x_r)), \tag{1}$$

where:

$L(x_r)$ is the number of visible paths at receiver position x_r, i.e. `size(cir,1)`

$\tilde{\alpha}_l(x_r)$ is the complex amplitude of the path, i.e. `cir(:,obj.info.amp)`

$\tilde{\tau}_l(x_r)$ is the delay of the path, i.e. `cir(:,obj.info.delay)` provided in seconds normalized to the receiver-transmitter distance divided by speed of light.

As an additional output of `sim_chan()`, the last interaction point of the ray is provided as matrix `p` where line l of the matrix represents the last interaction point of the l-th ray. Using the interaction point and the receiver position, the angle of arrival can be calculated in a straightforward manner in the coordinate system.

1.2 Detailed description of the satellite-to-indoor model

In the following section, the satellite-to-indoor channel model is described in a detailed way starting by an entry loss model that builds up the basis for the wideband satellite-to-indoor channel model that follows later on. In a later section, possible frequency extension, comparison to measurement data and software validation is addressed.

1.2.1 Entry loss model

The model is explained starting with a single room on the top floor of a building as depicted in Fig. 2.

FIGURE 2

Simple scenario: the receiver is located in a room on the top floor of a building
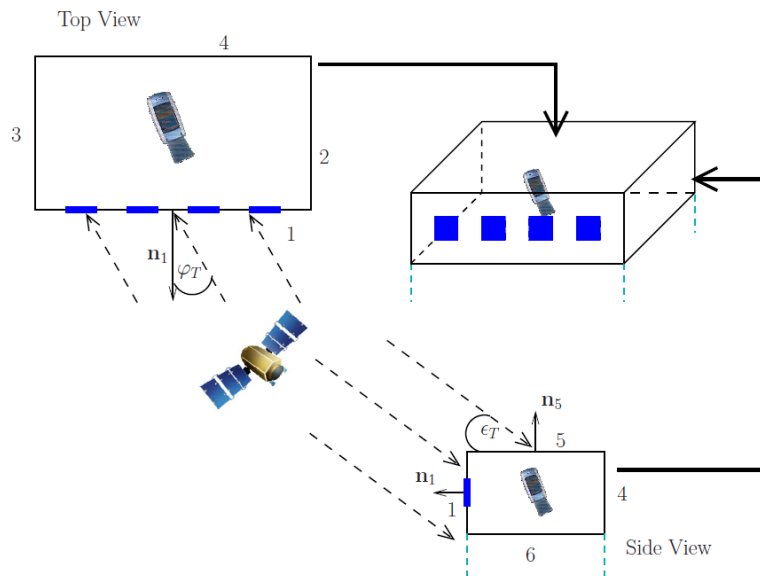
Figure 2 visualizes a simple scenario, where the receiver is located in a room on the top floor of a building. The numbers given are specifying walls labelled from 1 to 6.

In such scenario, the walls labelled $1,...,4$, and the roof, labelled 5 are external walls while the floor of the room is labelled as 6. Therefore, a satellite seen under azimuth φ_T and elevation angle $\varepsilon_T > 0$ with respect to the horizon will illuminate at least one external wall and the roof directly, and at most two external walls and the roof. For simplification, the incident angle ψ_i is defined as the angle

between   the   wall   normal n_i and   the   direction   vector
$\tilde{x}_t = [cos(\varepsilon_T)\,cos(\varphi_T),cos(\varepsilon_T)\,sin(\varphi_T),sin(\varepsilon_T)]^T$ to the satellite position x_t by:

$$\psi_i = cos^{-1}\left(\tilde{x}_t^T\,n_i\right) \tag{2}$$

Every wall i with an incident angle $\psi_i < 90^{\text{o}}$ is directly illuminated by the satellite and will contribute, to the received electric field strength[1] $E(\tau, x_r, x_t)$. Here τ stands for the reference delay while x_r and x_t denote the receiver and transmitter antenna position, respectively. Assuming a signal with a finite bandwidth B, the received field strength can be calculated by:

$$E(\tau, x_r, x_t) = \sum_{i=1}^{5}\mathsf{I}_\psi(\psi_i)\cdot E_i(\tau, x_r, x_t) \tag{3}$$

where $\mathsf{I}_\psi(\psi_i)$ is an indicator function of the illumination of an external wall defined by:

$$\mathsf{I}_\psi(\psi_i) = \begin{cases} 1 & \text{for } \psi_i < 90° \\ 0 & \text{for } \psi_i \geq 90° \end{cases} \tag{4}$$

Within the model, $E_i(\tau, x_r, x_t)$, $i = 1,...,6$, considers transmission loss, diffraction by the aperture of the wall and propagation delay. As the aperture for the diffraction of the i-th wall, the wall itself, and windows are considered in the model. The overall field strength $E_i(\tau, x_r, x_t)$ of the i-th wall is calculated accordingly by:

$$E_i(\tau, x_r, x_t) = T_{i,\text{wall}}(\tilde{x}_t)\left(D_{i,1,\text{wall}}(x_r,x_t) - \sum_{l=0}^{L_{i,\text{window}}-1}D_{i,l,\text{window}}(x_r,x_t)\right)$$
$$\cdot sinc(\tau - \tau_{i,1,\text{wall}})$$
$$+ T_{i,\text{window}}(\tilde{x}_t)\cdot \sum_{l=0}^{L_{i,\text{window}}-1}D_{i,l,\text{window}}(x_r,x_t)\cdot sinc(\tau - \tau_{i,l,\text{window}}) \tag{5}$$

$$\text{with } sinc(x) = \frac{sin(\pi Bx)}{\pi Bx}$$

where $T_{i,g}(\tilde{x}_t)$ stands for an angular dependent transmission coefficient of type $g \in G$, where $G = \{\text{wall, window}\}$, while $D_{i,k,g}(x_r,x_t)$ denotes the diffraction by the element k of the aperture. In equation (5), $L_{i,\text{window}}$ are considered elements of type $g = \text{window}$. For simplicity, the time delay of the contribution from element $\{i,k,g\}$ denoted by $\tau_{i,k,g}$ is approximated as $d_{i,k,g}/c_0$, where c_0 denotes the speed of light. Thus, the term $d_{i,k,g}$ is calculated as the distance sum $\|x_t - x\| + \|x - x_r\|$, where x is calculated as the closest point on the surface of the element $\{i,k,g\}$ to the direct line between x_t and x_r.

---

[1] It has to be noted that a time variation of the electric field strength due to the carrier frequency f_c, $e^{j2\pi f_c t}$, is not considered for simplicity.

The transmission coefficient $T_{i,g}(\tilde{x}_t)$ is calculated by:

$$T_{i,g}(\tilde{x}_t) = T_g \cdot \cos(\psi_i)^2 = T_g \cdot (\tilde{x}_t^T n_i)^2 \tag{6}$$

which has been found empirically using measured data. Within equation (6), T_g denotes the absolute value of the transmission coefficient of the element g for a wave propagating perpendicular through the material[2]. The model for the transmission coefficient provided in equation (6) is very simplistic and only based on the parameter T_g. In general more complex models like in [3] could be used for the angular dependent transmission coefficient.

The diffraction component $D_{i,k,g}(x_r, x_t)$ is calculated by solving the scalar Kirchhoff diffraction integral.

$$D_{i,k,g}(x_r, x_t) = \frac{1}{4\pi} \iint_{F_{i,k,g}} \mathsf{U}(\mathbf{p}, x_t) \frac{\partial \mathsf{E}(x_r, \mathbf{p})}{\partial n_i} - \mathsf{E}(x_r, \mathbf{p}) \frac{\partial \mathsf{U}(\mathbf{p}, x_t)}{\partial n_i} \partial f \tag{7}$$

where $F_{i,k,g}$ denotes the surface of the k-th element of type g for the i-th wall, $\mathbf{p}$ the point on the infinitesimal small surface ∂f while $\mathsf{U}(\mathbf{p}, x_t)$ and $\mathsf{E}(x_r, \mathbf{p})$ are the electric field components from the transmitter to $\mathbf{p}$ and from $\mathbf{p}$ to the receiver, respectively. For computational reasons, equation (7) can be reformulated as a line integral [1].

The entry loss $L_E(x_r, x_t)$ is calculated as:

$$L_E(x_r, x_t) = \frac{|E_{LoS}(x_r, x_t)|^2}{|E(\tau_{LoS}, x_r, x_t)|^2} \tag{8}$$

with the theoretical field strength $E_{LoS}(x_r, x_t)$ of a virtual propagating path via the geometrical LoS path in free space. The calculation of this theoretical field strength reads:

$$E_{LoS}(x_r, x_t) = \frac{a_{e.i.r.p.}}{\|x_t - x_r\|} \exp\left(-j \frac{2\pi}{\lambda} \|x_t - x_r\|\right) \tag{9}$$

where $\alpha_{e.i.r.p.}$ is a constant depending on the transmitter e.i.r.p., $\tau_{LoS} = \|x_t - x_r\| / c_0$ and λ the wavelength of the carrier frequency. In accordance, the normalized received power $P_E(x_r, x_t)$ at delay τ_{LoS} is:

$$P_E(x_r, x_t) = \frac{1}{L_E(x_r, x_t)} = \frac{|E(\tau_{LoS}, x_r, x_t)|^2}{|E_{LoS}(x_r, x_t)|^2} \tag{10}$$

1.2.2 Wideband satellite-to-indoor channel model

Figure 3 shows an overview of the modelled propagation paths which are considered in the proposed channel model. Because of the importance of the LoS path for range estimation algorithms, physical-deterministic methods based on the scenery are used to calculate its parameters. In the same way, physical-deterministic calculations are used to parametrize paths occurring due to diffraction at windows, for example, which have small additional propagation lengths compared to the geometrical LoS path. In

---

[2] To simplify, T_g is defined as being dependent on the type g, only.

the following, a group of paths will be denoted as direct components which are occurring due to diffraction and transmission by the wall's aperture. Therefore, the group of direct components consists of the LoS path and paths which are diffracted by the aperture of the walls. The direct components are calculated using physical-deterministic methods, and will be described in more detail in § 1.2.2.2.

FIGURE 2

Overview of propagation effects considered within the proposed satellite-to-indoor channel model
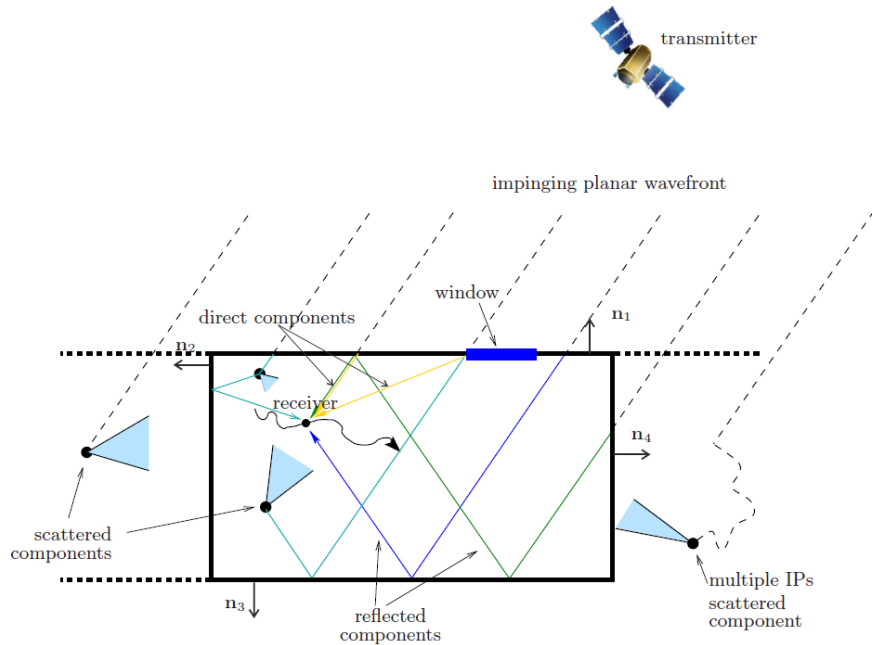

Propagation paths, which are reflected at the walls of the room are simulated. In this sense, side walls, roof and floor are considered as "walls". The maximum number of possible interactions with the walls are limited to two for each multipath component (MPC). In the following these paths will be called reflected components. The delays and the angle of arrival (AoA) of such MPC are determined by physical-deterministic methods using the geometrical relation of the transmitter-receiver geometry and the scenery. Other parameters like amplitude and phase of the MPC vary stochastically with the receiver position as described in § 1.2.2.2.

Another class of MPCs described in more detail in § 1.2.2.2 is denoted as scattered components in the following. This class of paths represents radio wave propagation which is spread out in all directions due to scattering [13]. Therefore, a scattered component includes a fixed point in the geometrical pathway, i.e. the position of the physical object, where scattering occurs. Objects which scatter an incoming wave may be a plant or the metallic leg of a table. Due to the complexity of the physical propagation mechanism of scattering, scattered components are fully stochastically modelled. As a fixed point is associated to each scattered component, the visibility of the path by the receiver as well as amplitude variations are modelled by an angular dependent pattern similar to [15], [16].

Figure 4 provides an overview on the satellite-to-indoor channel model by using a flow graph. As visualized, the model is split into two different parts: initialization and runtime part.

FIGURE 4

Simplified flow graph of the satellite-to-indoor channel simulator
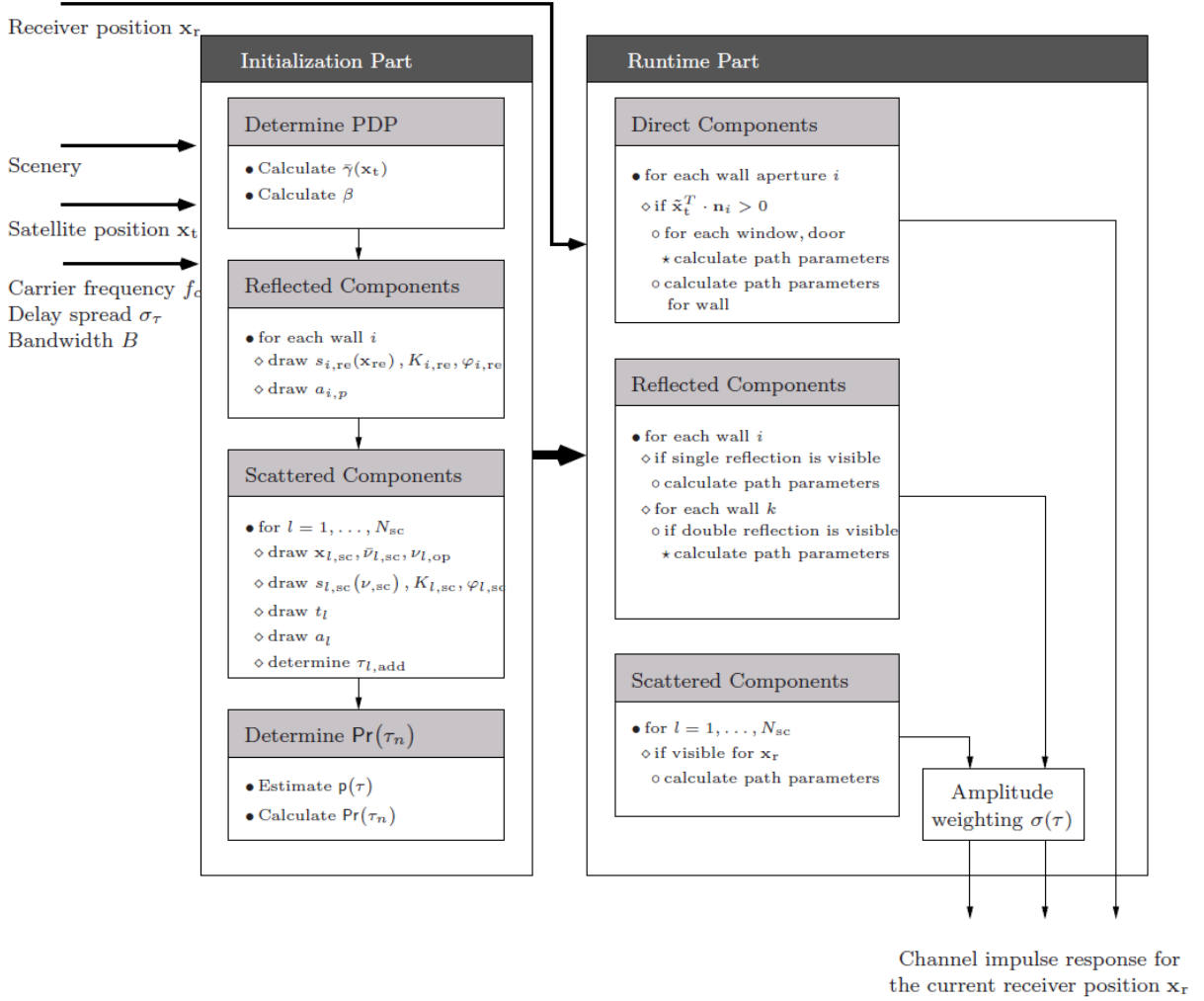
1.2.2.1 Initialization

For the initialization part, the user needs to supply a set of parameters which include the carrier frequency f_c, the delay spread σ_τ, the signal bandwidth B, the satellite position x_t and the scenery which defines the simulated room and the perpendicular transmission coefficients for the considered building materials.

Based on the scenery and the entry loss model which provides $P_E(x_r, x_t)$, the spatial averaged power delay profile (PDP) $\bar{P}(\tau, x_t)$ is calculated as:

$$\bar{P}(\tau, x_t) = E_{x_r}\left[P_E(x_r, x_t)\right] \cdot e^{-\tau B \beta} \tag{11}$$

with

$$\beta = 2\ln\left(\frac{1 + \sqrt{1 + 4B^2 \sigma_\tau^2}}{2B\sigma_\tau}\right) \tag{12}$$

and $E_{x_r}[\cdot]$ as the sample average over a grid of receiver positions x_r in a distance of $\Delta_{\bar{\gamma}(x_t)}$ located inside the space of the scenery R.

To initialize MPCs belonging to the reflected components, the stochastic process of the complex amplitude:

$$\left(s_{i,\text{re}}\left(x_{i,p,\text{re}} + y_{i,p,\text{re}}\right) + \sqrt{K_{i,\text{re}}}\, e^{j\varphi_{i,\text{re}}}\right) \cdot \frac{1}{\sqrt{1 + K_{i,\text{re}}}} \tag{13}$$

is drawn for each wall i of the room defined by the scenery where:

$x_{i,p,\text{re}}$ and $y_{i,p,\text{re}}$ define the two dimensional reflection point on the wall surface

$K_{i,\text{re}}$ is the Rice factor

$\varphi_{i,\text{re}} \in [0, 2\pi)$ is a uniform random random variable

$s_{i,\text{re}}\left(x_{i,p,\text{re}} + y_{i,p,\text{re}}\right)$ is an autoregressive process (AR)(1) with a pole p_{AR} on the real valued axis.

Additionally, $a_{i,p}$ is drawn for each wall i and $p \in \{1,2\}$. To characterize the randomness, statistics described in TABLE 1 are used.

TABLE 1

List of parameters for the satellite-to-indoor channel model

Parameter	Symbol	Unit	Value
Grid for receiver positions	$\Delta_{\bar{\gamma}(x_t)}$	[m]	$\Delta_{\bar{\gamma}(x_t)} = 0.5$
Grid for delay distribution	$\Delta_{p(\tau)}$	[m]	$\Delta_{p(\tau)} = 0.5$
Reflected Components			
Pole's amplitude of the AR(1)	p_{AR}		$(1 - p_{\text{AR}}) \sim \mathcal{W}_{]0,1[}(1 - p_{\text{AR}} \mid 0.06, 0.66)$
Rice factor	$K_{i,\text{re}}$		$K_{i,\text{re}} \sim \mathcal{W}(K_{i,\text{re}} \mid 10.86, 0.67)$
Delay independent amplitude	$a_{i,p}$		$a_{i,p} \sim \begin{cases} \mathcal{L}(a_{i,1} \mid -4.63, 1.29) & \text{for } p = 1 \\ \mathcal{L}(a_{i,2} \mid -4.81, 0.87) & \text{for } p = 2 \end{cases}$
Scattered Components			
Number of scattered components	N_{sc}		$N_{\text{sc}} = 10000$
Edge length of the box for $x_{l,\text{sc}}$	r_{sc}	[m]	$r_{\text{sc}} = 5\, c_0\, \sigma_\tau$
Type of component	t_l		$t_l \sim \begin{cases} \Pr(1 \mid x_{l,\text{sc}} \in \mathcal{R}) = 0.336 \\ \Pr(2 \mid x_{l,\text{sc}} \in \mathcal{R}) = 0.266 \\ \Pr(3 \mid x_{l,\text{sc}} \in \mathcal{R}) = 0.267 \\ \underline{\Pr(4 \mid x_{l,\text{sc}} \in \mathcal{R}) = 0.131} \\ \Pr(1 \mid x_{l,\text{sc}} \notin \mathcal{R}) = 1 \end{cases}$
Angular pattern beam width	$\nu_{l,\text{op}}$	[°]	$\nu_{l,\text{op}} \sim \begin{cases} \mathcal{W}(\nu_{l,\text{op}} \mid 24.01, 0.72) & \text{for } x_{l,\text{sc}} \in \mathcal{R} \\ \mathcal{W}(\nu_{l,\text{op}} \mid 3.15, 0.91) & \text{for } x_{l,\text{sc}} \notin \mathcal{R} \end{cases}$
Additional delay for $t_l = 2$	$\tau_{l,\text{add}}$	[s]	$\tau_{l,\text{add}} \cdot c_0 \sim \mathcal{N}_{[0,\infty]}(\tau_{l,\text{add}}\, c_0 \mid 16.07, 7.76)$
Pole's amplitude of the AR(1)	p_{AR}		$(1 - p_{\text{AR}}) \sim \mathcal{W}_{]0,1[}(1 - p_{\text{AR}} \mid 0.12, 0.49)$
Rice factor	$K_{l,\text{sc}}$		$K_{l,\text{sc}} \sim \mathcal{W}(K_{l,\text{sc}} \mid 10.44, 0.81)$
Delay independent amplitude	a_l		$a_l \sim \begin{cases} \mathcal{L}(a_{i,1} \mid -5.17, 0.85) & \text{for } t_l = 1,\ x_{l,\text{sc}} \in \mathcal{R} \\ \mathcal{L}(a_{i,2} \mid -5.05, 0.84) & \text{for } t_l = 2,\ x_{l,\text{sc}} \in \mathcal{R} \\ \underline{\mathcal{L}(a_{i,2} \mid -5.05, 0.84)} & \underline{\text{for } t_l \in \{3,4\},\ x_{l,\text{sc}} \in \mathcal{R}} \\ \mathcal{L}(a_{i,2} \mid -5.79, 0.85) & \text{for } t_l = 1,\ x_{l,\text{sc}} \notin \mathcal{R} \end{cases}$

NOTE – The Weibull distribution of x is denoted as $\mathcal{W}(x \mid \lambda, k)$ with scale parameter λ and shape parameter k while the truncated Weibull for $0 < x < 1$ is denoted as $\mathcal{W}_{]0,1[}(x \mid \lambda, k)$. In the same way $\mathcal{N}_{[0,\infty]}(x \mid \mu, \sigma)$ stands for the truncated normal distribution with $x \geq 0$ with mean μ and standard deviation σ. The log-normal distribution for x is denoted by $\mathcal{L}(x \mid \mu, \sigma)$ with parameters μ and σ.

In order to initialize MPCs belonging to the class of scattered components, the position $x_{l,\text{sc}}$ is drawn for every component $l = 1,\ldots, N_{\text{sc}}$. The position $x_{l,\text{sc}}$ may be located inside, i.e. $x_{l,\text{sc}} \in \mathcal{R}$, or outside,

i.e. $x_{l,\text{sc}} \notin \mathsf{R}$, the considered scenery. According to the location, the type $t_l \in \mathsf{T}$ of the scattered component l is drawn according to $\Pr(t_l | x_{l,\text{sc}})$ which is conditioned on the location of $x_{l,\text{sc}}$. If the type of the scattered component l is equal to 4, i.e. $t_l = 4$, the position of the MPC is changed by mirroring the drawn position at the wall. In agreement to the type of scatterer t_l, the additional delay $\tau_{l,\text{add}}$ for each scatterer l is determined. For the types $t_l \in \{3, 4\}$, $\tau_{l,\text{add}}$ is calculated using the geometrical relations while for $t_l = 2$, $\tau_{l,\text{add}}$ is drawn as a random variable from its distribution in TABLE 1. For the initialization of the complex amplitude, the random process:

$$\left(s_{l,\text{sc}}(v_{l,\text{sc}}) + \sqrt{K_{l,\text{sc}}}\, e^{j\varphi_{l,\text{sc}}} \right) \frac{1}{\sqrt{1 + K_{l,\text{sc}}}} \tag{14}$$

is drawn, where:

$\qquad v_{l,\text{sc}}$ is an angle on the horizontal plane

$\qquad K_{l,\text{sc}}$ is the Rice factor

$\qquad \varphi_{l,\text{sc}} \in [0, 2\pi)$ is a uniform random variable

$\qquad s_{l,\text{sc}}(v_{l,\text{sc}})$ is an AR(1) with a pole p_{AR} on the real valued axis.

Additionally, $\overline{v}_{l,\text{sc}}$ and $v_{l,\text{op}}$ are drawn from distributions displayed in Table 1.

After the MPCs belonging to the reflected and the scattered components have been initialized, the probability density function (PDF) $p(\tau)$ of the delay is estimated. For the estimation process, the delays of MPCs are determined for a grid of different receiver positions x_r with edge length $\Delta_{p(\tau)}$ within the scenery.

1.2.2.2 Runtime

During the runtime part of the satellite-to-indoor channel model, the channel impulse response (CIR) $h(\tau, x_r)$ is calculated dependent on the receiver position x_r provided by the user as:

$$h(\tau, x_r) = \sum_{l=0}^{L(x_r)-1} \tilde{\alpha}_l(x_r) \delta(\tau - \tilde{\tau}_l(x_r)) \tag{15}$$

where:

$\qquad L(x_r)$ is the number of visible paths at receiver position x_r

$\qquad \tilde{\alpha}_l(x_r)$ is the complex amplitude of the path

$\qquad \tilde{\tau}_l(x_r)$ is the delay of the path.

Direct components: In the satellite-to-indoor channel model, each wall i will contribute to the CIR if the vector product between the wall normal n_i and the vector from the centre of the scenery to the satellite $\tilde{x}_t = {x_t}/{\|x_t\|}$ is positive, i.e. $\tilde{x}_t^T \cdot n_i > 0$.

Each element $\{i,k,g\}$ is considered to be the source of an individual propagation path, where k the element number of type $g \in \{\text{wall, window}\}$. The amplitude of the simulated propagation path is calculated as:

$$\alpha_{i,k,g}(x_r, x_t) = T_{i,g}(\tilde{x}_t) \cdot D_{i,k,g}(x_r, x_t) \text{ for } g \in \{\text{window}\} \tag{16}$$

and

$$\alpha_{i,1,\text{wall}}(x_r, x_t) = T_{i,\text{wall}}(\tilde{x}_t)\left(D_{i,1,\text{wall}}(x_r, x_t) - \sum_{l=0}^{L_{i,\text{window}}-1} D_{i,l,\text{window}}(x_r, x_t) \right) \tag{17}$$

where:

$$T_{i,g}(\tilde{x}_t) = T_g \cdot \left(\tilde{x}_t^{\text{T}} n_i\right)^2$$

$$D_{i,k,g}(x_r, x_t) = \frac{1}{4\pi} \iint_{F_{i,k,g}} U(\mathbf{p}, x_t)\frac{\partial E(x_r, \mathbf{p})}{\partial n_i} - E(x_r, \mathbf{p})\frac{\partial U(\mathbf{p}, x_t)}{\partial n_i} \partial f \tag{18}$$

with T_g is the perpendicular transmission factor for elements of type g, $F_{i,k,g}$ denotes the surface of the k-th element of type g for the i-th wall, $\mathbf{p}$ the point on the infinitesimal small surface ∂f while $U(\mathbf{p}, x_t)$ and $E(x_r, \mathbf{p})$ are the electric field components from the transmitter to $\mathbf{p}$ and from $\mathbf{p}$ to the receiver, respectively.

The propagation path delay is calculated as $\tau_{i,k,g} = \frac{\|x_t - x\| + \|x - x_r\|}{c_0}$, where x is the closest point on the surface of the element $\{i,k,g\}$ to the direct line between the transmitter position x_t and receiver position x_r.

The angle of arrival (AoA) of the path can be calculated from the point x straightforward in the given coordinate system.

Reflected components: The simulation of the complex amplitude of paths $\alpha_{i,p,\text{re}}(\tau_{i,p,\text{re}}, \mathbf{x}_{i,p,\text{re}})$ occurring due to $p \in \{1,2\}$ wall reflections, where the last reflection is occurring on wall i is calculated by:

$$\alpha_{i,p,\text{re}}(\tau_{i,p,\text{re}}, \mathbf{x}_{i,p,\text{re}}) = \sigma(\tau_{i,p,\text{re}}) \cdot a_{i,p} \cdot w_{i,\text{refl}}(\mathbf{x}_{i,p,\text{re}})\left(s_{i,\text{re}}(\mathbf{x}_{i,p,\text{re}}) + \sqrt{K_{i,\text{re}}}\, e^{j\varphi_{i,\text{re}}}\right) \cdot \frac{e^{-j2\pi f_c \tau_{i,p,\text{re}}}}{\sqrt{1+K_{i,\text{re}}}} \tag{19}$$

where $\mathbf{x}_{i,p,\text{re}} = [x_{\text{re}}, y_{\text{re}}]^T$ is the two dimensional position of the reflection point on the wall surface;

$$\sigma(\tau_n) = \sqrt{\frac{\overline{P}(\tau_{i,p,\text{re}}, x_t)}{\int_{\tau_{i,p,\text{re}}-\frac{1}{2B}}^{\tau_{i,p,\text{re}}+\frac{1}{2B}} p(\tau)\partial\tau \sum_{l=0}^{L(x_r)-1} |\tilde{\alpha}_l(x_r)|^2}} \tag{20}$$

is a power adaptation to the spatially averaged PDP, f_c denotes the carrier frequency and $w_{i,\text{refl}}(\mathbf{x}_{i,p,\text{re}})$ is an amplitude windowing function as:

$$w_{i,\text{refl}}(\mathbf{x}_{i,p,\text{re}}) = w\left(\frac{x_{i,p,\text{re}} - \frac{l_{i,x}}{2}}{l_{i,x}}\right) \cdot w\left(\frac{y_{i,p,\text{re}} - \frac{l_{i,y}}{2}}{l_{i,y}}\right), \tag{21}$$

with

$$w(x) = \frac{1}{0.9415} \cdot \begin{cases} \frac{1}{2} sin\left(\frac{(x+0.5)\pi}{2 \cdot 0.05}\right) + \frac{1}{2} & \text{for} -0.55 \le x \le -0.45, \\ 1 & \text{for} -0.45 < x < 0.45, \\ -\frac{1}{2} sin\left(\frac{(x-0.5)\pi}{2 \cdot 0.05}\right) + \frac{1}{2} & \text{for} 0.45 \le x \le 0.55, \\ 0 & \text{for } x < -0.55 \text{ and } x > 0.55 \end{cases} \tag{22}$$

where $l_{i,x} \times l_{i,y}$ defines the dimension of wall i. The stochastic process:

$$\left(s_{i,\text{re}}(x_{i,p,\text{re}} + y_{i,p,\text{re}}) + \sqrt{K_{i,\text{re}}}\, e^{j\varphi_{i,\text{re}}}\right) \cdot \frac{1}{\sqrt{1 + K_{i,\text{re}}}} \tag{23}$$

has been initialized in § 1.2.2.1.

The delay $\tau_{i,p,\text{re}}$ and the AoA is calculated straightforward as reflection by the wall i knowing the transmitter and receiver position x_t and x_r, respectively.

Scattered components: The model for the complex amplitude $\alpha_{l,\text{sc}}(\tau_{l,\text{sc}}, \nu_{l,\text{sc}})$ for a path of the scattered components follows the model used for the reflected components as:

$$\alpha_{l,\text{sc}}(\tau_{l,\text{sc}}, \nu_{l,\text{sc}}) = \sigma(\tau_{l,\text{sc}}) \cdot a_l \cdot w\left(\frac{\nu_{l,\text{sc}} - \bar{\nu}_{l,\text{sc}}}{\nu_{l,\text{op}}}\right) \cdot \left(s_{l,\text{sc}}(\nu_{l,\text{sc}}) + \sqrt{K_{l,\text{sc}}}\, e^{j\varphi_{l,\text{sc}}}\right) \frac{e^{-j2\pi f_c \tau_{l,\text{sc}}}}{\sqrt{1 + K_{l,\text{sc}}}}$$

$$\tag{24}$$

The main difference between equations (24) and (19) is the dependence of $\alpha_{l,\text{sc}}(\tau_{l,\text{sc}}, \nu_{l,\text{sc}})$ on $\nu_{l,\text{sc}}$, which is the azimuthal angle between $x_{l,\text{sc}}$ and x_r on the horizontal plane. Therefore, equation (24) can be interpreted as an angular pattern for the l-th scattered component directed towards $\bar{\nu}_{l,\text{sc}}$ with a 6 dB beamwidth $\nu_{l,\text{op}}$.

The stochastic process:

$$\left(s_{l,\text{sc}}(\nu_{l,\text{sc}}) + \sqrt{K_{l,\text{sc}}}\, e^{j\varphi_{l,\text{sc}}}\right) \frac{1}{\sqrt{1 + K_{l,\text{sc}}}} \tag{25}$$

has been initialized in § 1.2.2.1.

Using the geometrical relation, the delay $\tau_{l,\text{sc}}$ of the l-th path, $l = 1, \text{K}, N_\text{sc}$ is calculated by:

$$\tau_{l,\text{sc}} = \left(\|x_\text{t} - x_{l,\text{sc}}\| + \|x_\text{r} - x_{l,\text{sc}}\|\right)\frac{1}{c_0} + \tau_{l,\text{add}} \tag{26}$$

where $\tau_{l,\text{add}}$ models an additional delay in order to simulate paths resulting from multiple object interactions initialized in § 1.2.2.1.

1.2.3 Frequency extension to C-band

Publication [7] provides a comparison between L-band and C-band wave propagation for the satellite-to-indoor scenario. As a result it was found that the main difference between both carrier frequencies is the entry loss, i.e. the averaged received power. Other statistical parameters like mean delay and delay spreads depend more on the actual propagation environment. Figure 5 taken from [7], [9]

visualizes the findings. While the received power varies between L- and C-band wave propagation the shape of the power delay profile shows clear similarities as for example a similar decay stands for a similar delay spread value. Also, Recommendation ITU-R P.1238 provides a formula for the delay spread value that is independent of the carrier frequency. Instead it depends only on the area of the floor space. Therefore, it may be concluded that the wideband satellite-to- indoor channel model can be extended to C-band frequencies by using carrier frequency related perpendicular building material transmission coefficients. Recommendation ITU-R P.2040 and [14] provide these values for a large variety of frequencies. Nevertheless, no validation of the model for other frequency bands has been performed.

FIGURE 5

Comparison of measured power delay profiles for a satellite-to-indoor scenario
at L-band and C-band, taken from [5], [7]
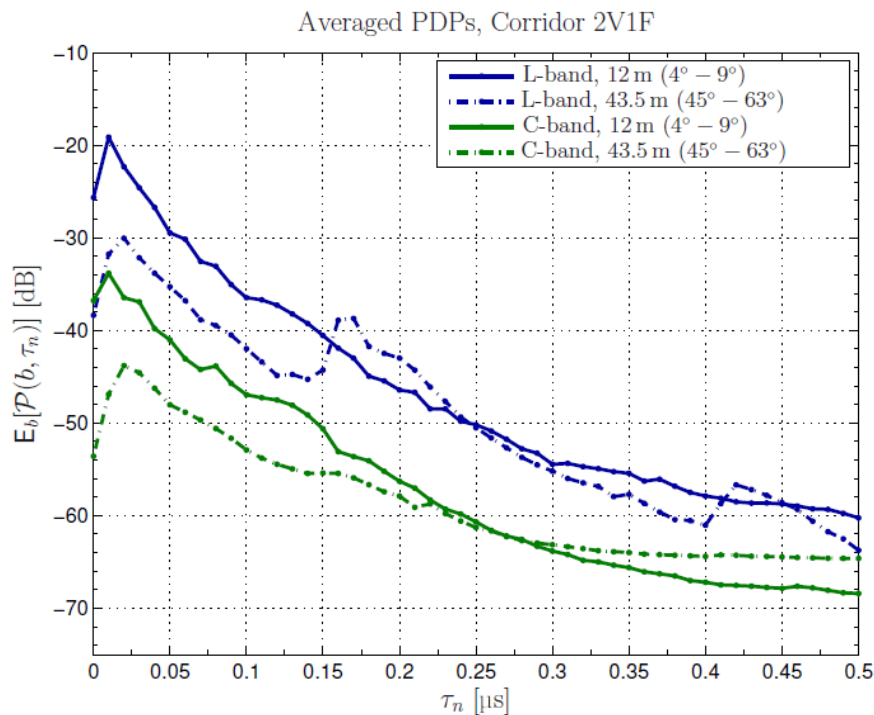
1.2.4 Simulation example

To visually inspect the output of the satellite-to-indoor channel model, a simulation example. Is presented. Figure 6 visualizes the underlying scenery. As shown, the receiver moves along a circular path which has a radius of 3 m around the centre of the scenery. A CIR is calculated for every degree of the circle for two loops of receiver movement, so for the angles 0° to 720°.

FIGURE 6

Visualization of the scenery used for the simulation.
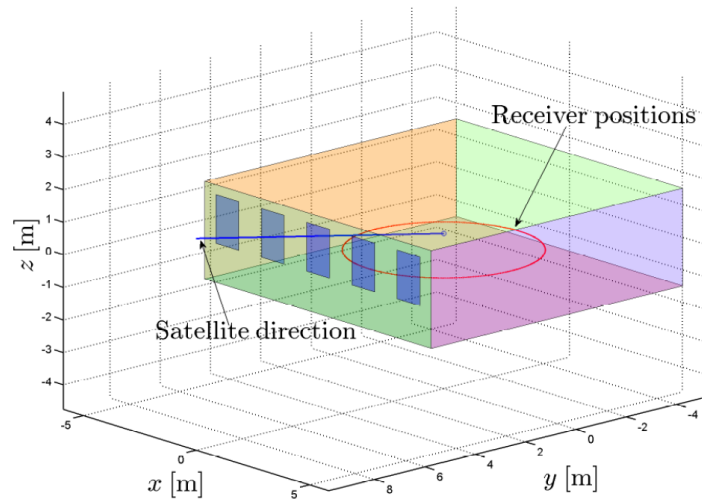
In Figure 6, the circle represents the receiver trajectory while the line marks the direction to the satellite located in the far field.

FIGURE 7

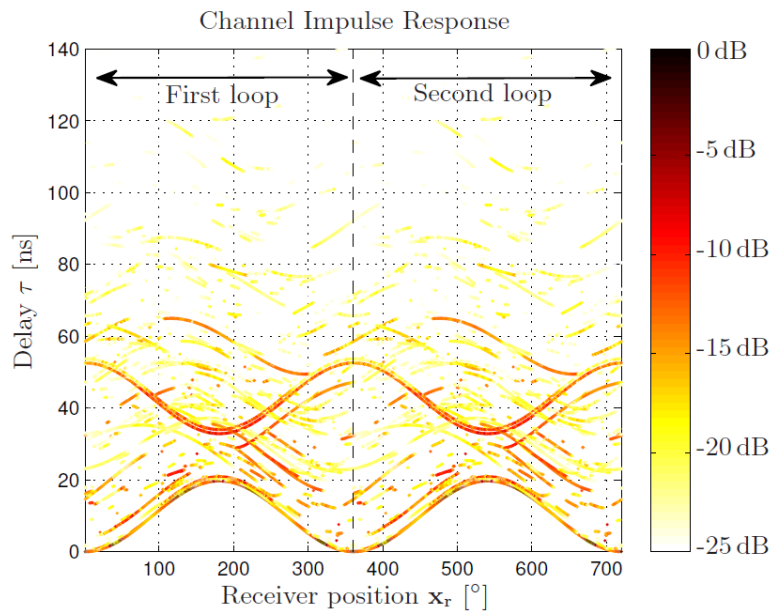**CIRs calculated by the channel simulator for the circular trajectory of the receiver**

Figure 7 visualizes the CIRs calculated for each receiver position using a colour-scale for the amplitude of the paths. As the simulated receiver performs two loops, a repetition of the CIRs is visible. The amplitude of the paths is shown in colour-scale. The delays of the paths are subtracted by the propagation delay of the geometrical LoS path at the first receiver position in the simulation, i.e. the closest point on the circular trajectory to the window front. Figure 7 shows an exact repetition of CIRs for the first and the second loop of receiver movement. Once the transmitter-receiver geometry is fixed, the CIR is fixed. Naturally, MPCs of the class of direct components have the smallest delays among all paths. Because the receiver is moving on a circular trajectory, the direct components' delays follow a sinusoidal curve. Figure 7 reveals also two paths between $\tau = 32$ ns and $\tau = 54$ ns which are visible for all receiver positions and show a converse delay behaviour compared

to the direct components. The first one of the two paths is a reflection at the rear-wall of the room seen from the transmitter, while the second path is a reflection at the same wall after the signal is reflected from the floor of the room. Other paths visualized in Fig. 7 show random-like delay behaviour. The amplitude variation of individual paths follows a correlated process with a rising and a falling slope in cases of appearance and disappearance, respectively.

The number of MPCs which have a minimum amplitude of −25 dB with respect to the geometrical LoS path amplitude per calculated CIR is visualized in Fig. 8. Like in Fig. 7, the curve repeats itself for the first and the second loop of the circular receiver movement. For this specific simulation, the number of paths changes between a minimum of 17 and a maximum of 37.

FIGURE 8

**Number of paths in the simulation**
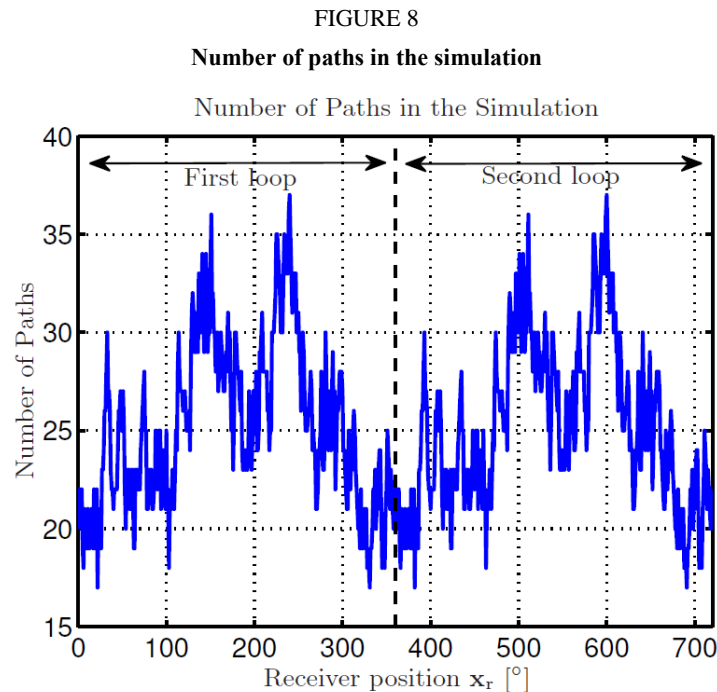
1.2.5 Comparison to measurement data

To compare the output of the satellite-to-indoor channel model to measurement data, the scenery used in the model has to be adjusted to the measurement environment. Therefore, it must consist of a room with the same size and the same number of windows as in the measurements. It is expected that the channel model provides a slightly different outcome as the scenery applied to the channel model uses infinitely thin windows and walls. Moreover, furniture and other objects located inside the room during the measurements cannot be incorporated into the simulation. The measured CIRs have been obtained for a 12.5 m track of the model railway [7]. The measurement data is split into segments where each segment corresponds to 10 cm on the railway track. Accordingly, a PDP $P(\tau_n)$ can be calculated for every segment. Using the different PDP a PDF $p(P(\tau_n))$ of the received power for every τ_n can be estimated.

Figures 9 and 10 compare the estimated PDF of the received power for every τ_n between the measurement data and the channel model output for two different heights of the transmit antenna.

FIGURE 9

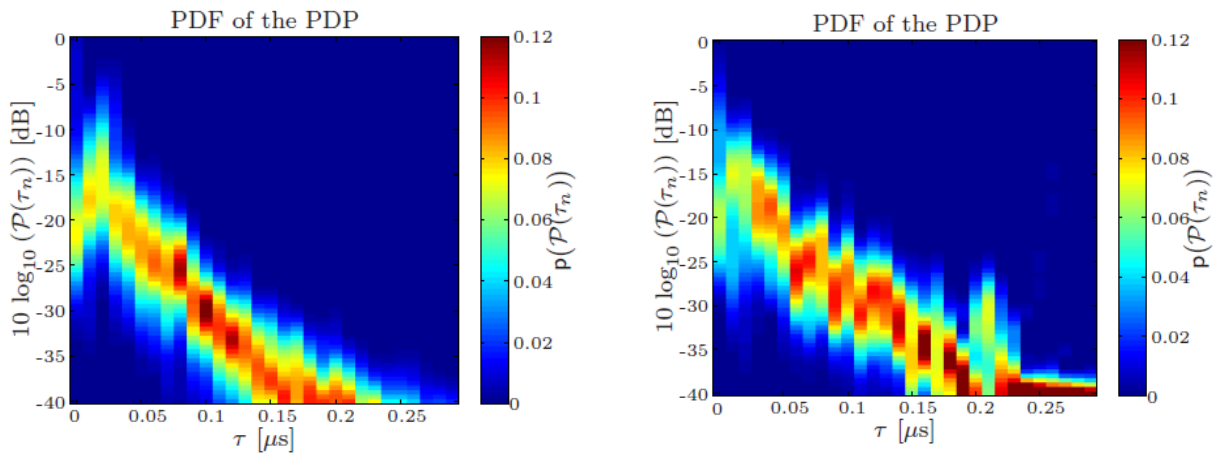**Visualization of the estimated PDF $P(\tau_n)$ for each τ_n of the PDP $P(\tau_n)$**
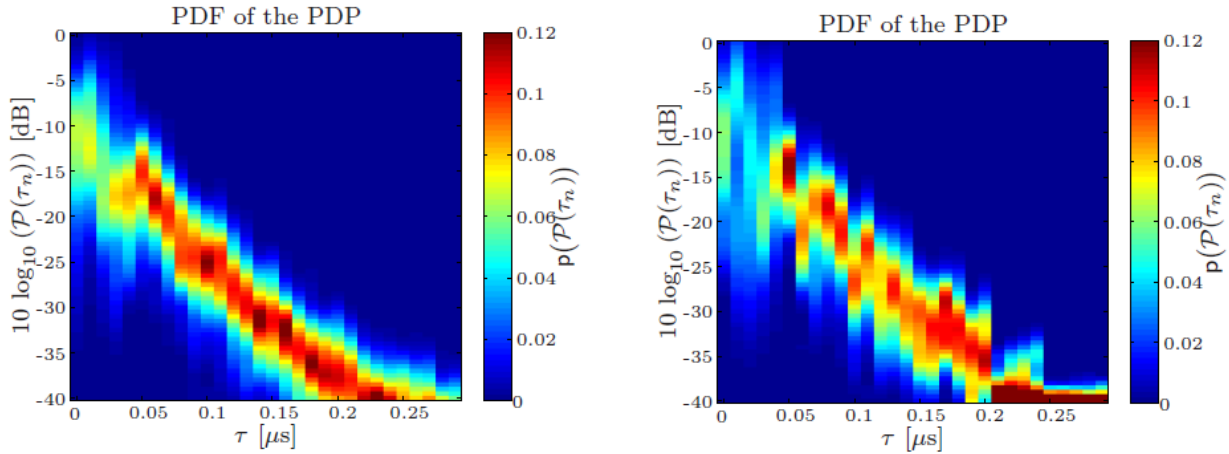
(a) Estimated PDF for each τ_n of the PDP $P(\tau_n)$ obtained from the measured data.

(b) Estimated PDF for each τ_n of the PDP $P(\tau_n)$ obtained from the simulated data.

Figures 9(a) and 9(b) show the PDF obtained from measurement data and simulation data respectively. For both data sets, the transmit antenna was located in a distance of about 25 m and about 3 m above the receiving antenna.

FIGURE 10

Visualization of the estimated PDF $P(\tau_n)$ for each τ_n of the PDP $P(\tau_n)$

(a) Estimated PDF for each τ_n of the PDP $P(\tau_n)$ obtained from the measured data.

(b) Estimated PDF for each τ_n of the PDP $P(\tau_n)$ obtained from the simulated data.

Figures 10(a) and 10(b) show the PDF obtained from measurement data and simulation data respectively. For both data sets, the transmit antenna was located in a distance of about 30 m and about 16 m above the receiving antenna.

Comparing Fig. 9(a) to Fig. 9(b) and Fig 10(a) to Fig. 10(b), similarities are visible. The shape of the curves follows a similar decay. Additionally, curves obtained from the simulated data show similar magnitudes of power and a similar maximum value of $p(P(\tau_n))$ per delay sample n.

Nevertheless, the deviation from the exponential decaying curve seems to be larger in Figs 9(b) and 10(b) compared to Figs 9(a) and 10(a). This might result from a different spatial distribution of scattered components in the artificial scenery of the channel model compared to the measurement scenario.

To evaluate the applicability of the channel model to ranging applications, a simplified simulation using the Global Positioning System (GPS) coarse/acquisition (CA) code signal is performed. The comparison is based on the same measurement data evaluated every 1 cm on the railway track. In navigation receivers, the standard ToA estimator is a delay-locked loop (DLL) which estimates the delay τ_{DLL} of the maximum correlation peak. For a pure LoS channel, the DLL estimate is maximum likelihood (ML) [12]. To simplify the evaluation, τ_{DLL} is used as the delay of the maximum peak of the magnitude for the CIR convoluted with the idealized correlation function of the GPS CA code signal. Consequently, the ranging error ε_{DLL} is calculated as:

$$\varepsilon_{DLL} = \tau_{DLL} \cdot c_0 - d_{tr}, \tag{27}$$

where d_{tr} denotes the distance between the transmit and receive antenna. Using this simplified evaluation strategy, inherently a static scenario with a narrow spacing DLL is assumed. Because of the relatively high power in the measurements compared to a real satellite-to-indoor propagation scenario, τ_{DLL} can interpreted as a bias occurring due to multipath propagation. Figures 11 and 12 provide the CDF curves of ε_{DLL} using simulated and measured CIRs for two different transmitter positions. The behaviour of the CDF curve based on the simulated or measured CIR is quite similar for both transmitter positions.

In order to provide a comparison based on more advanced methods, the Kalman enhanced super resolution tracking (KEST) algorithm [8] is applied instead of a DLL. The algorithm serves here as a multipath mitigation algorithm based on sequential Bayesian filtering. Advanced multipath mitigation algorithms like [2], [4] and [10] estimate the CIR in order to reduce the multipath interference on the delay estimation of the LoS path. Therefore, estimated CIRs from the measured and simulated data are compared.

CIR measured over a spatial distance of 4 m on a railway track are used. Note that due to the usage of stochastic components in the satellite-to-indoor channel model, the CIR cannot be expected to be identical. Figure 13 compares the estimated CIR based on measured and simulated data.
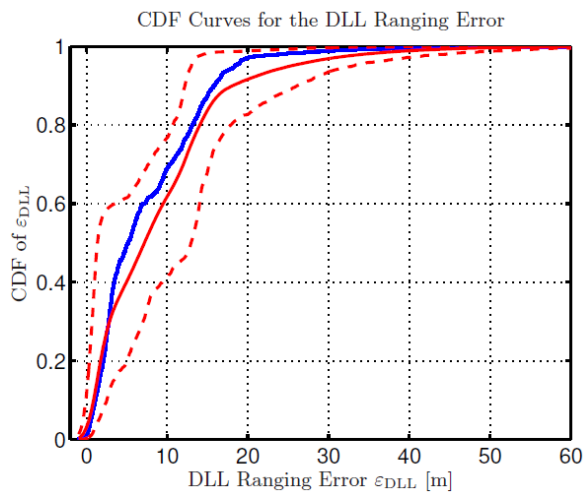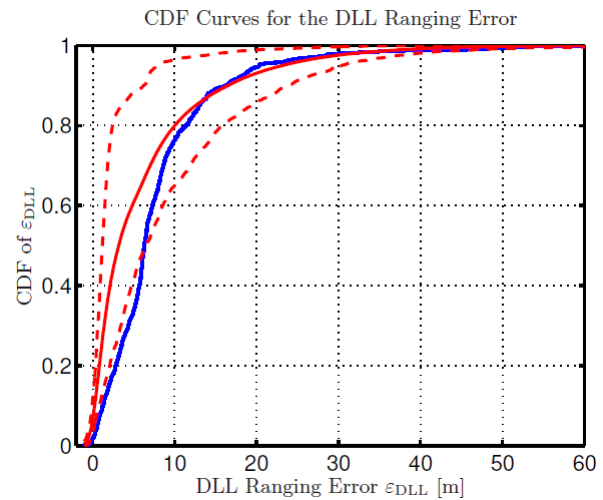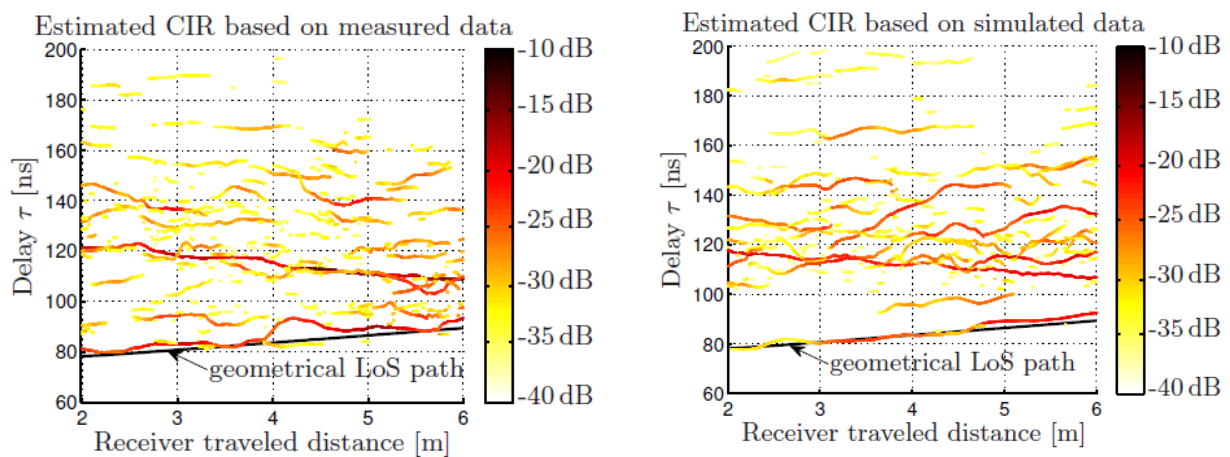
FIGURE 12

CDFs of the DLL ranging error ε_{DLL} based on simulated and measured CIRs.

In Figure 11, the CDF based on the simulated data has been calculated as the average of 200 simulations while the dashed curves provide the 95% confidence interval. For both data sets, the transmit antenna was located in a distance of about 25 m and about 3 m above the receiving antenna. In Figure 12, the CDF based on the simulated data has been calculated as the average of 200 simulations while the dashed curves provide the 95% confidence interval. For both data sets, the transmit antenna was located in a distance of about 30 m and about 16 m above the receiving antenna.

FIGURE 13

Visualization of estimated CIRs using the KEST algorithm

(a) Estimated CIRs using measured data.

(b) Estimated CIRs using simulated data.

Figure 13 shows estimated path in their delay and power over receiver travelled distance which covers 4 m overall. The distance between transmit and receive antennas is indicated by the geometrical LoS path. The KEST algorithm is applied to both, measured and simulated data, as shown by the left and right figure, respectively. For both data sets, the transmit antenna was located in a distance of about 25 m and about 3 m above the receiving antenna.

The comparison between Fig. 13(a) and Fig. 13(b) reveals a large amount of similarities. In both Figures, curves representing individual paths are visible behaving in a similar way while the receiver moves. Paths in both Figures show a high correlation for small receiver position changes in amplitude and delay. Also a path with a decreasing delay from ≈120 ns to ≈110 ns is visible in both Figures which originate from a reflection at the rear wall of the room. The power values of paths are also in a similar range between −39.5 dB to −12.8 dB in Fig. 13(a) and between −39 dB to −18.1 dB in Fig. 13(b) for this specific simulation.

Figure 14 compares the number of detected paths using the KEST algorithm based on measured and simulated data. Both curves show several similarities. The number of detected paths by KEST is ranging between 6 and 20 for measured data and between 7 and 19 for the channel model simulation.

FIGURE 14

Visualization of the detected number of paths using the KEST algorithm based on measured and simulated data
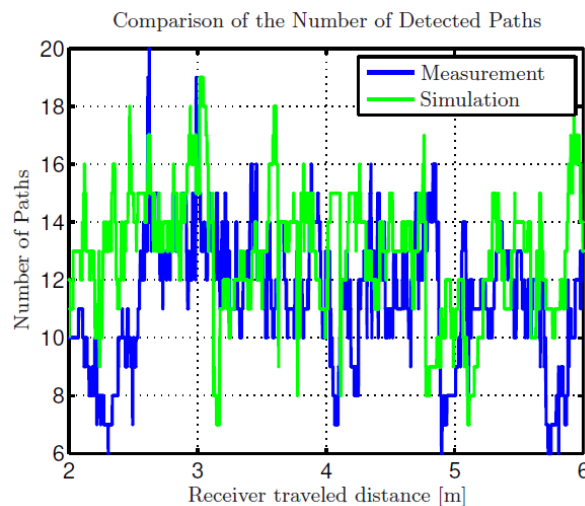
1.2.6   Software validation

In this section the software of the satellite-to-indoor is qualitatively checked. In a first simulation, a relatively simple room is simulated where a specific behaviour can be expected. In a second simulation a more complex scenery is used and qualitative values are audited.

### 1.2.6.1   Checks using a simple room structure

In order to verify the diffraction calculations, a room with a single large window is simulated. The perpendicular transmission coefficient is set to −100 dB for all walls and the roof in order to restrict the signal power received via walls and roof. The window on the other side is simulated using a perpendicular transmission coefficient of 0 dB. The room size is set to 20x80x100 m, and the window has been placed with the following parameters:

–   winWidth = 40 m

–   winUpper = 0.3 m

–   winLower = 1.2 m

A visualization of the room is provided in Fig. 15.

FIGURE 15

Visualization of the room used to verify the diffraction calculation.
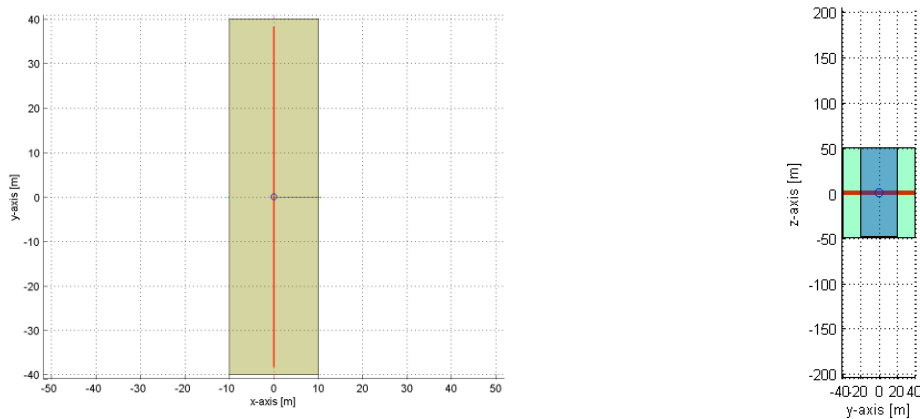
As visible, the receiver trajectory is linear along the y-axis (i.e. parallel to the window) with a 0.05 m grid step (Fig. 15, red line). The transmitter direction is perpendicular to the window, i.e. simulated at azimuth and elevation angle of 0°.

First the diffraction profile resulting from the window opening is verified. The numerical integration used in the satellite-to-indoor channel simulator to Fresnel integration based knife edge is first compared. It is important to validate this point due to the following reasons:

–   In the model, diffraction calculations are a major part of the entry loss model. Therefore, the diffraction calculation directly impacts the spatial averaged power delay profile and, as a consequence the power of individual MPCs.

–   Due to the use of the physical deterministic model for the direct components, these components are subject to errors in the diffraction calculations. Especially for ranging, the line-of-sight path is very important within simulations. Therefore, errors in the calculation of the diffracted power will have a direct impact on assessed signal processing algorithms.

To validate the implementation, the diffraction calculations based on the numerical integration as it is implemented in the satellite-to-indoor channel model to the Fresnel integration based knife edge is then compared. Comparing both calculations in Fig. 16 reveals that similar results are obtained.

FIGURE 16

Comparison of Fresnel integration and numerical integration used in the satellite-to-indoor channel simulator
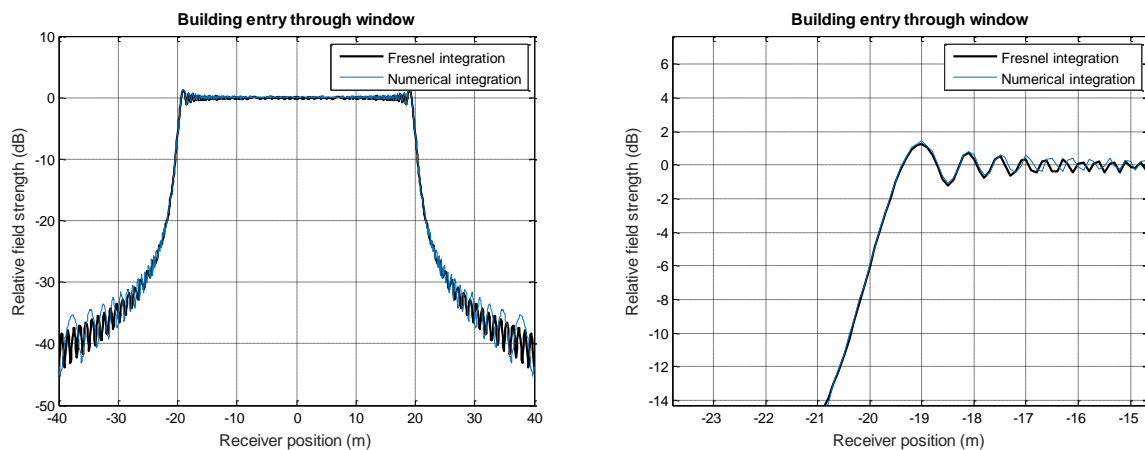
To further validate the diffraction implementation, the power of the direct component through the window obtained from the CIR data output using the linear receiver trajectory is compared to uniform theory of diffraction (UTD) calculations. The result of the comparison in Fig. 17 reveals again clear similarities.

FIGURE 17

Power of the direct component for the window (blue line) in comparison to UTD (black line). The red line marks the border between line-of-sight through the window and non line-of-sight. In accordance to theory both methods show a 6dB attenuation at this point
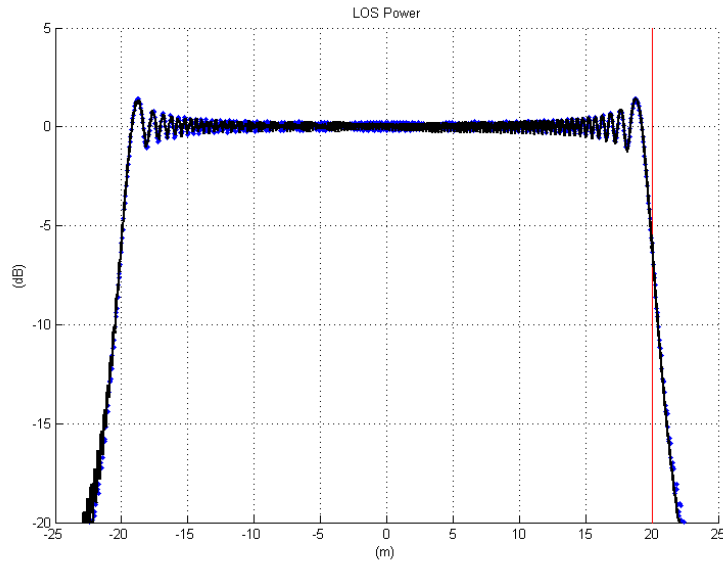

Figure 18 provides a visualization of the number of visible paths during a simulation. It can be observed that calculating the amount of paths that are above −50 dB in amplitude compared to free space loss is rising while the receiver is moving on the linear trajectory. This rise is an unexpected behaviour. Nevertheless, taking the amount of paths that are above −25 dB in amplitude compared to free space loss, the behaviour is as expected showing a uniform distribution.

Number of visible paths within the simulation
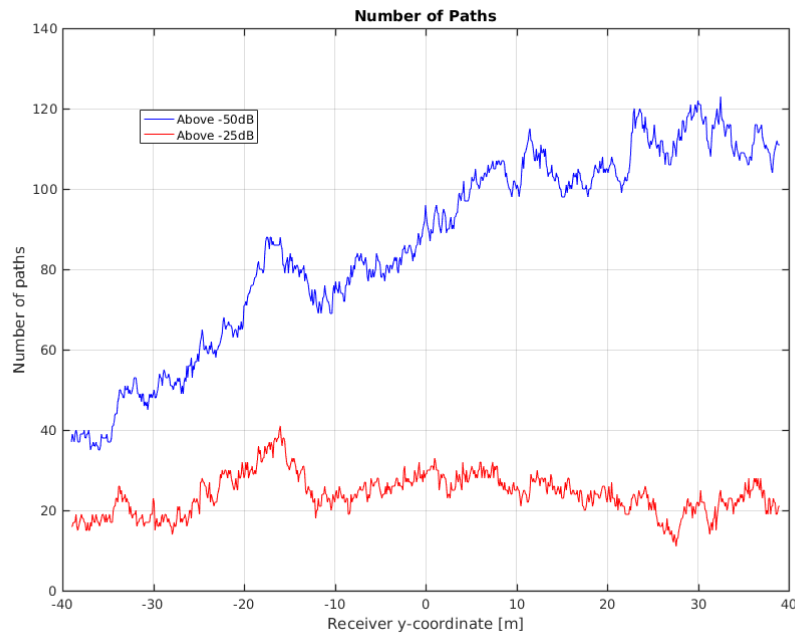
Still the question may arrive if the total narrowband multipath power may show a similar effect as the blue curve in Fig. 18. In Figure 19, the multipath narrowband power is plotted versus the receiver position and it is easily verifiable that the power is uniformly distributed as expected.

FIGURE 19

Narrowband multipath power
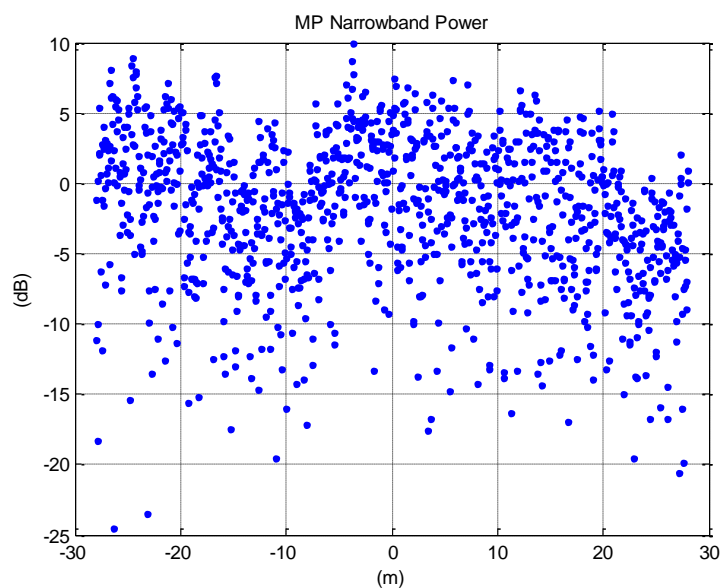
To further investigate towards the validity for the application system (here GNSS), the ranging error is estimated by assuming an early minus late (EML) discriminator with one chip spacing. To do so, for each receiver position the post-correlated signal is built based on the model output:

$$y(\pmb{x}_r) = \sum_{l=0}^{L(\pmb{x}_r)-1} \tilde{\gamma}_l(\pmb{x}_r) r(\tilde{\tau}_l(\pmb{x}_r))$$

where $\pmb{x}_r$ the receiver position and $y(\pmb{x}_r)$ the post-correlated signal. $\{\tilde{\gamma}_l(\pmb{x}_r)\}_{l=0:L(\pmb{x}_r)-1}$ are the complex amplitudes provided by the simulator at receiver position $\pmb{x}_r$, $\{\tilde{\tau}_l(\pmb{x}_r)\}_{l=0:L(\pmb{x}_r)-1}$ the relative delay with respect to the line-of-sight signal, $r(.)$ the auto-correlation function of the GPS C/A signal (triangular function), $L(\pmb{x}_r)$ the number of paths at the corresponding receiver position. The discriminator error can be calculated as:

$$D(\pmb{x}_r) = \left| y\left(\pmb{x}_r, -\frac{C_S}{2}\right)\right|^2 - \left| y\left(\pmb{x}_r, \frac{C_S}{2}\right)\right|^2$$

with C_S the chip spacing equal to one. In Figure 20 the results are visualized. It may noticed that certain symmetry is present with smaller average error for receiver positions [−20 m, 20 m] at which the line-of-sight signal is unobstructed receivable through the window. Nevertheless due to multipath the discriminator error includes a high amount of randomness.

FIGURE 20

**EML Discriminator Error simulating a GPS C/A signal**
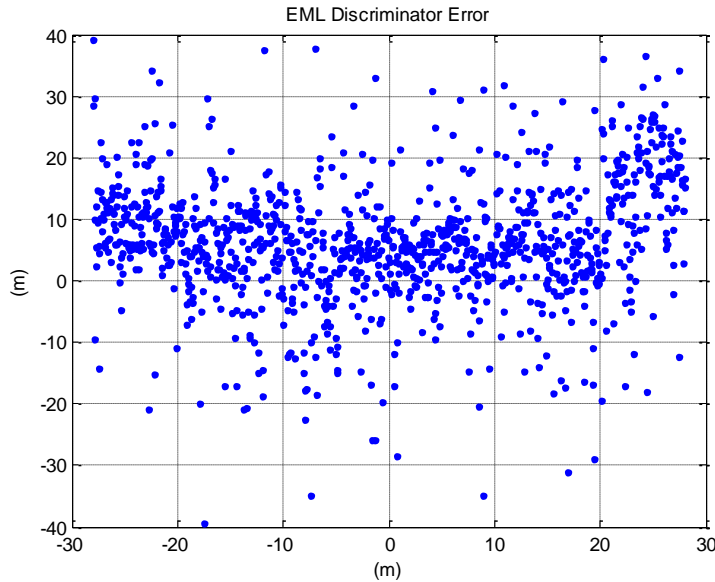
1.2.6.2   Checks using a more complicated room structure

To qualitatively check more complicated room structures a room with 10x10x10 m and three windows is created shown in Fig. 21. The width of each window is 2 m, and the distances to the upper and lower edge are 0.3 m and 1.2 m, respectively. The transmitter elevation and azimuth are 0° with respect to the room, and the following perpendicular transmission coefficients were used:

$$T_{win} = -2\ dB, T_{wall} = -15\ dB, T_{roof} = -25\ dB\ .$$

FIGURE 21

Room structure used during the second type of simulations
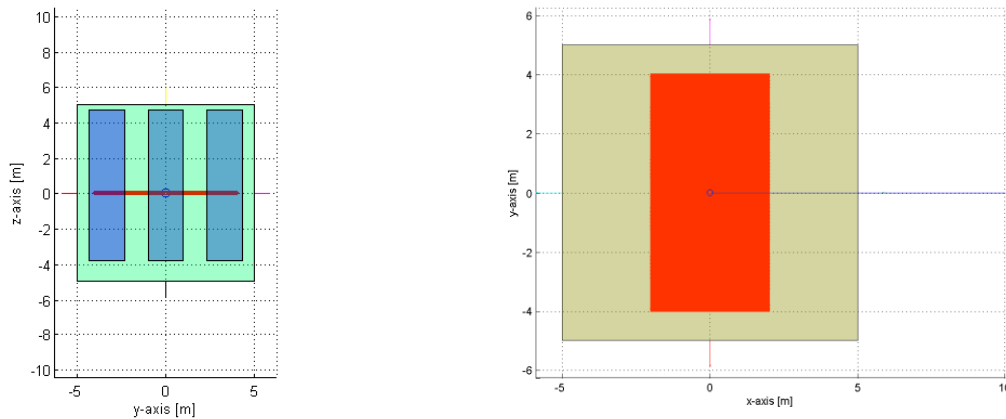
Note – The red square visualizes the receiver positions located on a grid inside a rectangular of 4 m x 8 m

The simulated receiver positions are located on a grid of 0.04 m inside a 4 m x 8 m square located on the x/y-plane as shown in Fig. 21.

For verification the narrowband power (coherent sum) of the direct components and of the residual components (i.e. reflected and scattered components) is computed. The resultant powers as functions of the receiver positions are shown in Fig. 22.

For the narrowband power of the direct components (Fig. 22, right side) the impact of the windows and of the wall is easily noticed: in front of a window, the LOS power is close to −2 dB and in front of a wall, the LOS power is close to −15 dB, which is consistent with the used perpendicular transmission coefficients.

The narrowband power of the residual components (Fig. 22, left side) on the other side shows a very random uniformly distributed behaviour in dependence on the receiver position. It may be noticed that the power of the residual components is on a similar scale as the power of the direct components in this simulation. Using a lower value for the delay spread, would let the power of the residual components decrease.

FIGURE 22

Resulting narrowband power calculations for the direct components and the residual components
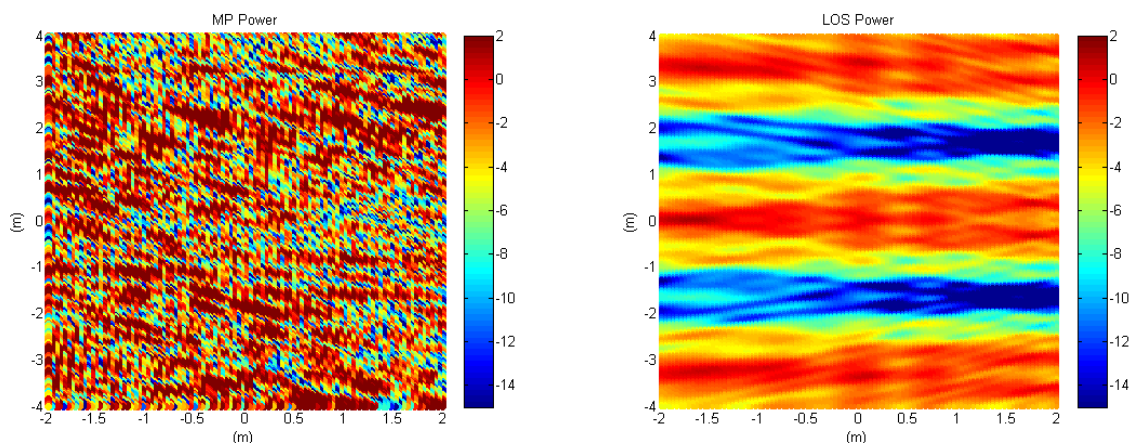
Note – The power of MPCs belonging to the reflected or scattered components is visualized on the left while on the right is shown the narrowband power of the direct components in dependence of the receiver position

Simulating the discriminator error for a GPS C/A signal a random behaviour can be noticed in Fig. 23. Indeed, from the simulation, the residual components narrowband power has a slightly higher power than the direct components narrowband power, and thus the error follows the random pattern.

FIGURE 23

Discriminator Error (m)
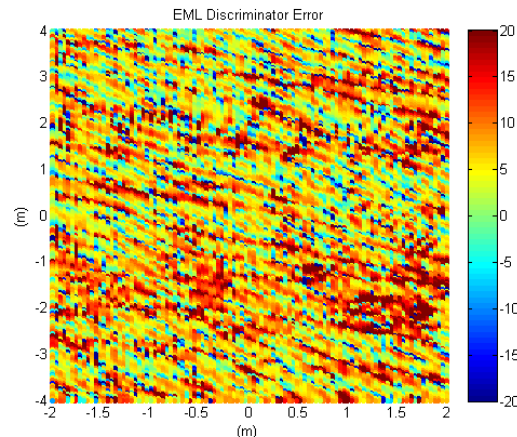
2   References

[1]   M. Albani, "Boundary diffracted wave and incremental geometrical optics: A numerically efficient and physically appealing line-integral representation of radiation integrals. Aperture scalar case," IEEE Trans. Antennas Propag., vol. 59, no. 2, pp. 586-594, Feb. 2011.

[2]   F. Antreich, J. Nossek, and W. Utschick, "Maximum Likelihood Delay Estimation in a Navigation Receiver for Aeronautical Applications," Aerospace Science and Technology, vol. 12, no. 3, pp. 256-267, 2008.

[3]   W. Burnside and K. Burgener, "High frequency scattering by a thin lossless dielectric slab," IEEE Trans. Antennas Propag., vol. 31, no. 1, pp. 104-110, Jan. 1983.

[4]   P. Closas, C. Fernández-Prades, and J. A. Fernández-Rubio, "A Bayesian Approach to Multipath Mitigation in GNSS Receivers," IEEE J. Sel. Areas Signal Process., vol. 3, no. 4, pp. 695-706, Aug. 2009.

[5]   T. Jost, Satellite-to-Indoor Wave Propagation for Positioning Applications, ser. Kommunikationstechnik. Verlag Dr. Hut, 2014, PhD dissertation.

[6]   T. Jost, G. Carrié, F. Pérez-Fontán, W. Wang, and U.-C. Fiebig, "A Deterministic Satellite-to-Indoor Entry Loss Model," IEEE Trans. Antennas Propag., vol. 61, no. 4, pp. 2223-2230, Apr. 2013.

[7]   T. Jost, W. Wang, U.-C. Fiebig, and F. Pérez-Fontán, "Comparison of L- and C-Band Satellite-to-Indoor Broadband Wave Propagation for Navigation Applications," IEEE Trans. Antennas Propag., vol. 59, no. 10, pp. 3899-3909, Oct. 2011.

[8]   T. Jost, W. Wang, U.-C. Fiebig, and F. Pérez-Fontán, "Detection and Tracking of Mobile Propagation Channel Paths," IEEE Trans. Antennas Propag., vol. 60, no. 10, pp. 4875-4883, Oct. 2012.

[9]   T. Jost, W. Wang, U.-C. Fiebig, and F. Pérez-Fontán, "A Wideband Satellite-to-Indoor Channel Model for Navigation Applications," IEEE Trans. Antennas Propag., vol. 62, no. 10, pp. 5307-5320, Oct. 2014.

[10]   B. Krach, P. Robertson, and R. Weigel, "An Efficient Two-Fold Marginalized Bayesian Filter for Multipath Estimation in Satellite Navigation Receivers," EURASIP J. Adv. Sig. Proc., vol. 2010, 2010.

[11]   F. Pérez-Fontán, V. Hovinen, M. Schönhuber, R. Prieto-Cerdeira, F. Teschl, J. Kyrolainen, and P. Valtr, "A wideband, directional model for the satellite-to-indoor propagation channel at S-band," Int. Journal of Satellite Communications and Networking, vol. 29, no. 1, pp. 23-45, 2011.

[12]   B. W. Parkinson and J. J. Spilker Jr., Global Positioning System: Theory and Applications, Vol. 1. American Institute of Aeronautics and Astronautics Inc., 1996.

[13]   T. S. Rappaport, Wireless Communications – Principles and Practice. Prentice Hall, 1996.

[14]   W. C. Stone, "Electromagnetic Signal Attenuation in Construction Materials," NIST, Tech. Rep. NISTIR 6055, Oct. 1997.

[15]   F. Schubert, B. Fleury, P. Robertson, R. Prieto-Cerdeirai, A. Steingass, and A. Lehner, "Modeling of multipath propagation components caused by trees and forests," in EuCAP, 2010.

[16]   T. Santos, F. Tufvesson, and A. Molisch, "Modeling the Ultra-Wideband Outdoor Channel: Model Specification and Validation," IEEE Trans. Wireless Commun., vol. 9, no. 6, pp. 1987-1997, 2010

_____